INTELLIGENT MANUFACTURING APPLIED TO ADDITIVE MANUFACTURED POLYMER GEARS

By

Ye Zhang

A thesis submitted in partial fulfilment of the requirements for the degree of

Doctor of Philosophy in Engineering

University of Warwick, School of Engineering

February 2020

Abstract: Nylon spur gears were 3D printed using Nylon 618, Nylon 645, alloy 910 filaments, together with Onyx and Markforged nylon proprietary materials, with wear rate tests performed on a custom-built gear wear test rig. The results showed that Nylon 618 provided the best wear performance among the 5 different 3D printing materials tested. It is hypothesised that the different mechanical performance between nylon filaments was caused by differences in crystallinity and uniqueness of the Fused Deposition Modelling (FDM) process. The performance results showed that gears 3D printed using Nylon 618 actually performed better than injection moulded nylon 66 gears when low to medium torque was applied. The selection of printing parameters for 3D printing can dramatically affect the dynamic performance of components such as polymer spur gears. Performance of 3D printed gears has been optimised using a machine learning process. A genetic algorithm (GA)–based artificial neural network (ANN) multi-parameter regression model was created. There were four print parameters considered in 3D printing process, i.e. printing temperature, printing speed, printing bed temperature and infill percentage. The parameter setting was generated by the Sobol sequence. Moreover, sensitivity analysis was carried out, and leave-one cross validation was applied to the genetic algorithm-based ANN which showed a relatively accurate performance in predictions and performance optimisation of 3D printed gears.

Small-angle X-ray scattering (SAXS), wide-angle X-ray scattering (WAXS), differential scanning calorimetry (DSC), X-ray fluorescence (XRF) and Fourier-transform infrared (FTIR) test were carried out to analyse the influence from different Nylon materials to the dynamic performance and mechanical properties of 3D printed gears, and demonstrate the intrinsic links between processing parameter, mechanical performance, and materials. Various of computer simulation has been carried out to test the different loading scenario affecting gear and materials performance. The Objective of this project is to improve the performance of the 3D printed polymer gears.

Contents

Table of figures.

Acknowledgement

仅以此论文献给我的父母以及爱妻徐诺.

To my beloved parents and wife Nuo Xu.

I would like to thank my supervisor Dr. Ken Mao and Dr. Simon Leigh for their supports.

Declaration

This thesis is submitted to the University of Warwick in support of my application for the degree of Doctor of philosophy.

I hereby declare that it has been composed by myself and has not been submitted in any previous application for any degree.

Publications

Zhang, Y, Mao, K., Simon, L., Shah, A., Chao Z., & Mao G. (2020). A parametric study of 3D printed polymer gears. The International Journal of Advanced Manufacturing Technology, 2020;107:(11-12), 4481-4492.

Zhang Y, Purssell C, Mao K, Leigh S. A physical investigation of wear and thermal characteristics of 3D printed nylon spur gears. Tribology International. 2020; 141:105953.

Ma G, Chao Z, Zhang Y, Zhu Y, Hu H, editors. The application of support vector machine in geotechnical engineering. Earth and Environmental Science; 2018: IOP Publishing.

Chao Z, Ma G, Zhang Y, Zhu Y, Hu H, editors. The application of artificial neural network in geotechnical engineering. Earth and Environmental Science; 2018: IOP Publishing

Chapter 1. Introduction to polymer gear and additive manufacturing process.

1.1. General

The objects of this project were to predict and improve the performance of the polymer gear. There are two main parallel research lines undertaken within the Warwick research team, one group was focused on the injection mould gears, another group was focused on 3D Printed gears. This thesis was concentrated mainly on the 3D printed gears. There were three main stages of this project. The first stage was to understand the basic behaviour of the 3D printed gears, including wear rate, loading capacity and material behaviour. The second stage was focused on one material, to improve the performance by control the parameters of the 3D printer. The third stage was to investigate how each parameter could change the material behaviour. It was one of the first research carried out the analysis the 3D printed polymer gear and it has proved that 3D printed gear has potential to overcome the performance of injection mould gears.

In recent years, there have been increasing demands for polymer composites in different engineering applications, due to their quite running, excellent moulding ability and low weight. However, polymer composite gear is not widely used in the gear systems of automotives due to lack of mechanical strength and heat resistance. Hence, it is practical to used additional components such as carbon fibres, glass fibres and nanotubes to reinforce the mechanical strength of the polymer composite. (2)

1.2. Polymer material properties.

There are 5 materials was mainly used in this project, High density polyethylene (PE), Polyxymethylene (POM), Polyamide (Nylon), Polycarbonate (PC), and PEEK 650G (Polyetheretherketone). According to Frank (3), it is important to consider material properties such as how material temperature depends on thermal characteristics (mechanical and chemical structure of thermoplastics resins) for example Glass Transition (Tg), Flow Temperature (Tf),

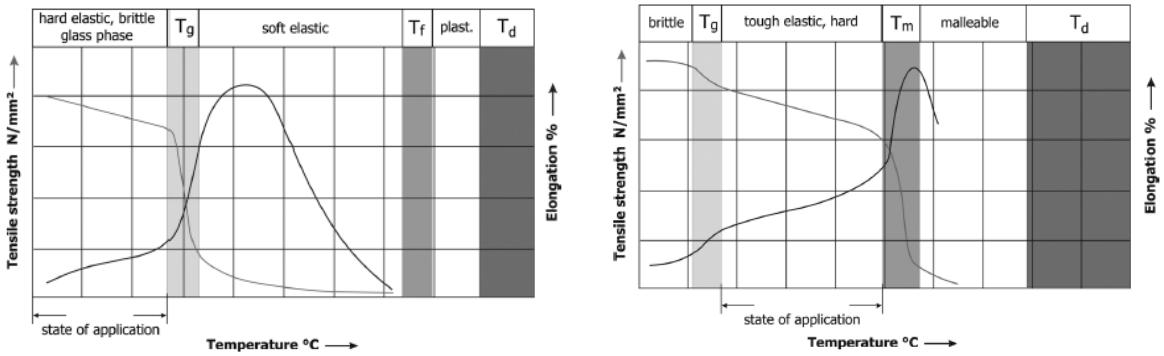

Figure 1.Temperature behaviour of semi-crystalline amorphous thermoplastic resins.

Crystallite Melting Temperature (Tm), Thermal Decomposition (Td), Dimensional Stability, Thermal Conductivity, Thermal Diffusivity and Heat Capacity (4). It is clearly indicated that, there was a gap between glass transition temperature and melting temperature. During this phase, the crystalline structure was transferred into amorphous phase.

As shown in figure 1, plastics will change into different phases when the temperature is increased, hence, temperature could produce an impact on the mechanical properties. Moreover, according to the B.Darlix (4), the yield stress and Young's modulus of polycarbonate decreased as temperature rises.

1.3. Reinforced Polymer composite.

For applications such as gears and bearings which requiring high load capacities, high temperature resistance and low friction required, hence, increasing mechanical properties of polymer gear became necessary (5). Moreover, in the process of reinforcing polymer gears, two main parameters of filler could affect the outcomes filler material and filler proportion.

Firstly, there are several of matrices including polyoxymethylene, polyetheretherketone, Polyethylene and Polycarbonate could provide as host material. The filler could be inorganic or organic, and it could improve wear resistance by bonding between transfer films and metallic counterparts in the chemical phase, or improve modulus and hardness which is mechanical phase (6). In terms of inorganic filler, such us copper, Cus and SiC could enhance the bonding between the transfer film and the metallic counterpart with PEEK (7-9). Nevertheless, in terms of organic filler, such as carbon fibre and glass fibre, these will affect both chemical properties and mechanical properties. The reinforcement of PEEK leads to a significant reduction in the specific wear rate during long dry sliding against steel (10).

Secondly, the proportion changing of the filler could also affect the wear resistance. According to S. Mishra et al. (11), there were two different types of organic filler, glass fibre and biofibre (sisal fibre pineapple leaf fibre) used to reinforce polyester, and it is believed that increasing the

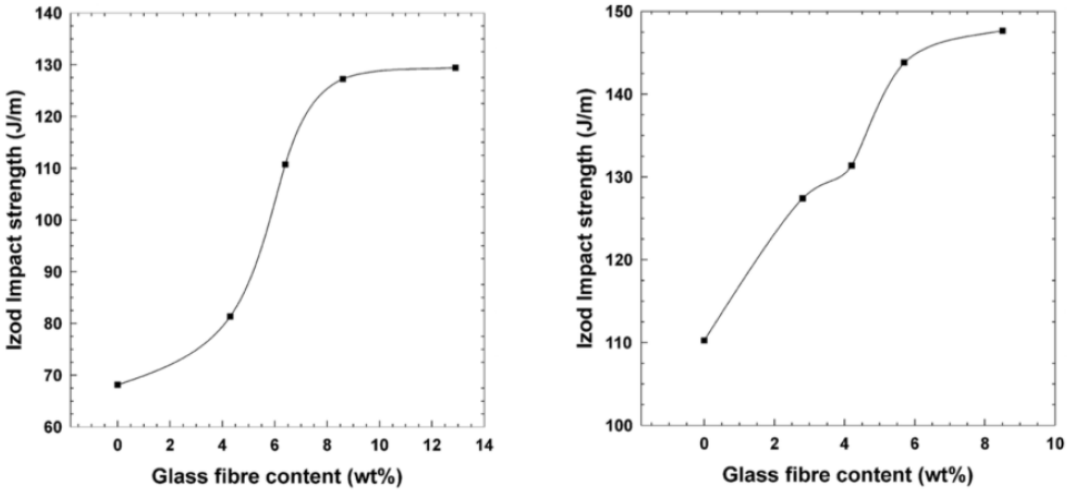

(a) (b)

Figure 2. (a) Effect of glass fiber loading on the impact strength of PALF/ glass hybrid polyester composite (total fibre content=25 wt. %). (b) Effect of glass fiber loading on the impact strength of sisal/ glass hybrid polyester composite (total fiber content 30 wt.%

percentage of the fibre filler could improve the impact strength . However, after certain percentage of filler, the wear resistance stay constant. Shown in figure 2 above.

Moreover, it is argued that size of the fillers could affect the wear behaviour, Durand et al claimed that a larger size of the filler (around 100 μm) could provide better wear resistance than smaller filler (around 20 μm), however, Xin et al. (12) proved that, the smaller filler size around 120 to 510 nm sized particles seemed to be more effective in improving the wear resistance.

1.4. Polymer gear and reinforcement.

According to the K. Mao (13, 14) , the acetal and nylon gear wear behaviour and performance prediction were introduced based on the gear thermal mechanical contact with the real world experimental and numerical calculation. It was claimed that the performance of acetal gear depends on the surface temperature, increasing of the temperature and causing an increasing rate of wear, and it also affects the gear transition torque. However, the nylon gear friction and wear performance were different compared with acetal gear, and the failures of nylon gear are often root and pitch fractures rather than surface failure. Moreover, according to the Kurokawa (15, 16),it is shown that Poly-ether-ether-ketone (PEEK) can provide excellent gear performance, while, by using carbon fibre reinforced PEEK could increase gear performance compared with unfilled PEEK. However, PEEK is relatively expensive compared to other various of Polymers such as polyamide 12 (PA12), Polyamide 6 (PA6), polyamide 66 (PA66). The performance of PA12 carbon fiber reinforcement shows better result compared other PAs and lower cost compared with PEEK.

Furthermore, Senthilvelan (17) stated that the alignment of glass fibre along the gear tooth involute could reduce the shrinkage, also provide better results in profile deviation. However, due to the orientation of the glass fibre, not all the glass fibre could fill along the gear tooth, hence, glass fibre which does not coinciding with tooth lead will not improve the shrinkage, hence, the rate of shrinkage with the glass fibre reinforcement gear was not uniform. Figure 3 below shown the orientation of the fibre within the injection mould gear.

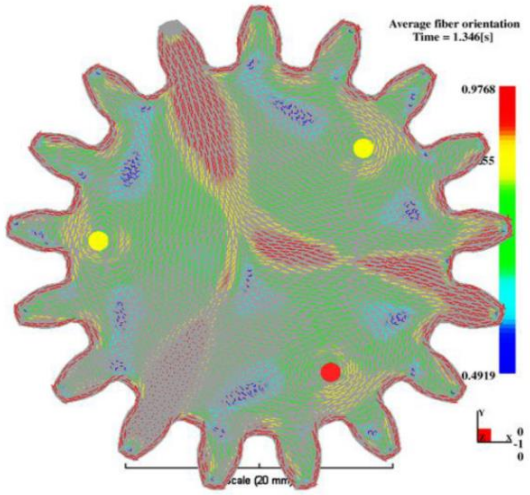

Figure 3. Predicted average fiber orientation in glass fiber reinforced.

Chapter 2. Literature review.

2.1. Finite element method.

According to Reddy (18), finite element method is a method that could estimate the solution to boundary value problems for the partial deferential equations. FEM divides relatively complex problems into smaller and simpler elements, then calculates each small problem and converge every the small problems to estimate the final value of the whole problem.

2.2 History and application of FEM.

FEM was first used to solve complex elastic and structural problems. It is not clear that when finite element method was invented, however, according to work done by Hrennikoff (19) and Courant (20), around1950s to 1960s, the systematic numerical methods was created for solving a partial differential equation to solve dam construction problem, based on this method the concept of the element was introduced. Until the late 1960s, the actual FEM method was introduced by the J.H Argyris.

The demand for FEM has increased in various industries, including aeronautical biomechanics and automotive industrie. With the different packages for specific components such as thermal electromagnetic, fluid and structural working environments.

2.3. Recent spur gear simulation using FEM

Due to dramatic increase in the power of computers, FEM simulations are become increasingly accurate. According to Asker (21), the contact stress and deformation of gear tooths is simulated in a linear single tooth contact, shown as figure 4(a), this simulation could provide relatively accurate linear contact behaviour, however, this simulation could not represent the dynamic

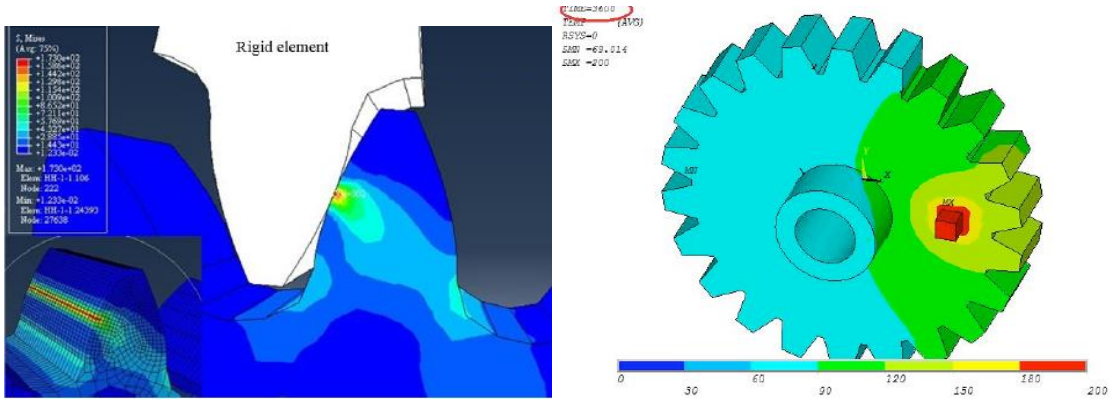

(a) (b)

Figure 4. (a) linear static simulation of stress on gear tooth. (21) (b) heat flow analysis in steel gear. (22)

contact behaviour of gear tooth. Moreover, Vivek (22) was created a linear contact of a steel spur gear has been simulated with FEM, and as the result, comparison between hertz equation calculation and FEM simulation is compared. It has shown a linear contact between two gears.

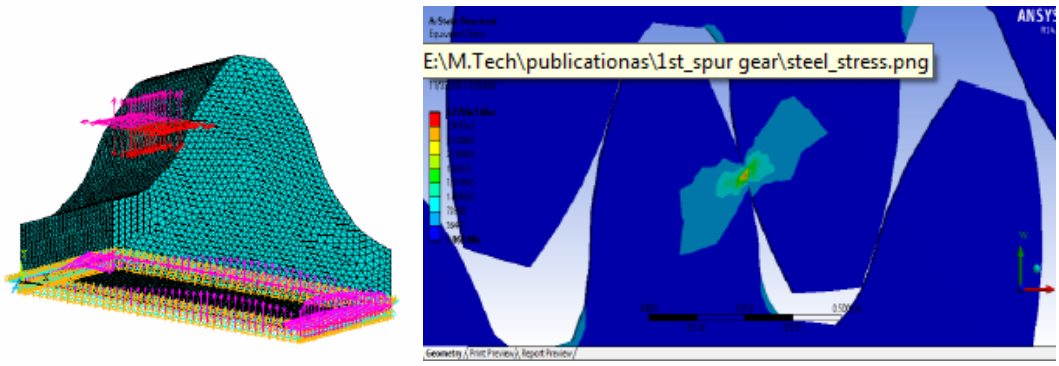

Figure 5. linear simulation of stress on gear tooth.

Furthermore, Qrimli (23), provides a relatively accurate static contact simulation of steel spur gears, shown as figure 5, in his simulation, the static gear was against with a tooth shaped rigid element. In this simulation the FEM result was compared with both Hertz equation, and AGMA equation with an error of 12.71% and 1.66%, however, in this static simulation, Hertz effect was not fully represented due to the different mechanical properties between the rigid body and gear body, moreover, the full cycle of the gear tooth contact was not carried out. Johns simulated a more accurate gear pair with rotation which could observe full meshing cycle of the gear tooth, moreover, in the report, different effect of misalignment was also carried out. Nevertheless, Xin.W (24) simulated the heat flow within the gear by created a heating point located on the side of gear. Moreover, in this simulation, some cracks were generated to analyse the heat transfer at a crack. However, this report was only focused on how the cracks affect the heat transfer and does not represent the heat generate by the friction of the gear tooth shown in figure 5(b).

In order to simulate the fiber reinforcement, it is practical by adding fiber filler into composite will increase the mechanical performance. Tibor and Friedrich (25), (26) modelled the tribological performance of composite polymer with steel counterpart using analysis by real world experiment and FEM simulation. As the figure 6 shows below, a steel sphere was slid across the carbon fiber reinforcement polymer, in three different orientation, and different behavior with different orientations of fiber filler was discussed. K.K.Chawla (27), claim that fiber reinforcement material

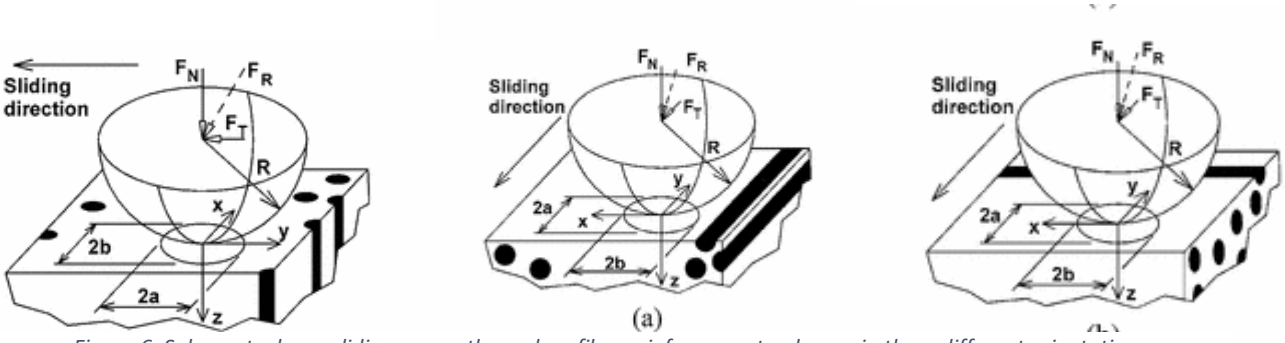

Figure 6. Sphere steel was sliding across the carbon fibre reinforcement polymer, in three different orientation

is inhomogeneous material that should follow the rule of mixtures formula.

The tribological performance was analysed, and stress allocation of polymer and carbon fibre was also discussed. It is believed that normal fibre orientation could provide better mechanical performance. Furthermore, even though the thermoplastic are unsuitable for high torque load transmission, but by adding carbon fibre could significantly increase enforcement, moreover, with 30% volume of glass fibre in polymer composite loading behaviour is studied.

Moreover, due to the simulation being increasingly complex, many researches are working on reducing the computational time while retaining accuracy. According to Paul (28), computational time could be reduced by adding hand calculation associated with FEM. In other words, this method that combined Hertz equations and FEM, reduce computer cost and provide a relatively accurate result. However, this method has significant drawback due to the limitations of the contact position, and the result of this method could only show of single contact position. Hence, such

methods can only provide limited information of helical gear contact analysis. Furthermore, Alencar B created a model which could predict the failure by three different dynamic effect thermal simulation, wear simulation and fatigue simulation (29), and this simulation could provide both thermal affect, wear affect and fatigue affect. whereas, realistically three dynamic effect were working on gear operation at the same time, however, in this simulation three dynamic simulation was modelled separately.

2.4. Additive Manufacturing Process

Due to the process of the injection mould processes the fiber filler orientation within the host martial was hard to control, however, it is possible to control the filler orientation by additive manufacturing process. There has been a rapid growth in the number of units sold from 2010. In the process of additive manufacturing process, geometric information is provided by computer-aided design (CAD), then, CAD file will be converted to a stereolithography (STL) file. This SLT file is converted the CAD drawing into sliced part which containing the information for each layer going to be printed (30).

There are three main supply sources for additive manufacture (liquid, powder and solid) divided by seven industrial additive manufacturing processes which are stereo lithography(SL), fused deposition modelling (FDM), ink jet printing(IJP), three dimensional printing(3D-P), selective laser sintering (SLS), laser cladding, and laminated object manufacture. (LOM) (31).

Stereolithographic (SL) is a liquid based process, and in this process the liquid phase polymer converted into a solidified polymer by ultraviolet (UV) light scan. The thickness of each layer limited by the power of the UV light. In the process of fused deposition modelling (FDM), a thin polymer filament feld and melted into the metal print head to extrude certain objects, and this is a relatively cost effective process but restricted by resolution of the Z axis (31), (32). There are many different filaments available on the market including polylactic acid (PLA), acrylonitrile butadiene styrene (ABS), polycarbonate (PC) and many others. Ink jet printing (IJP) requires a droplet of molten material to achieve layer deposition. As well as the three-dimensional printing (3D-P), droplets of molten material is also required to solidify the solid powder material. Selective laser sintering (SLS) using laser to fuse power material to provide layers, moreover, the majority of current commercial printers apply CO2 lasers, power supply from 50W to 200W. Laser cladding (LC) are process in which power material is forced through a nozzle to the laser beam by using

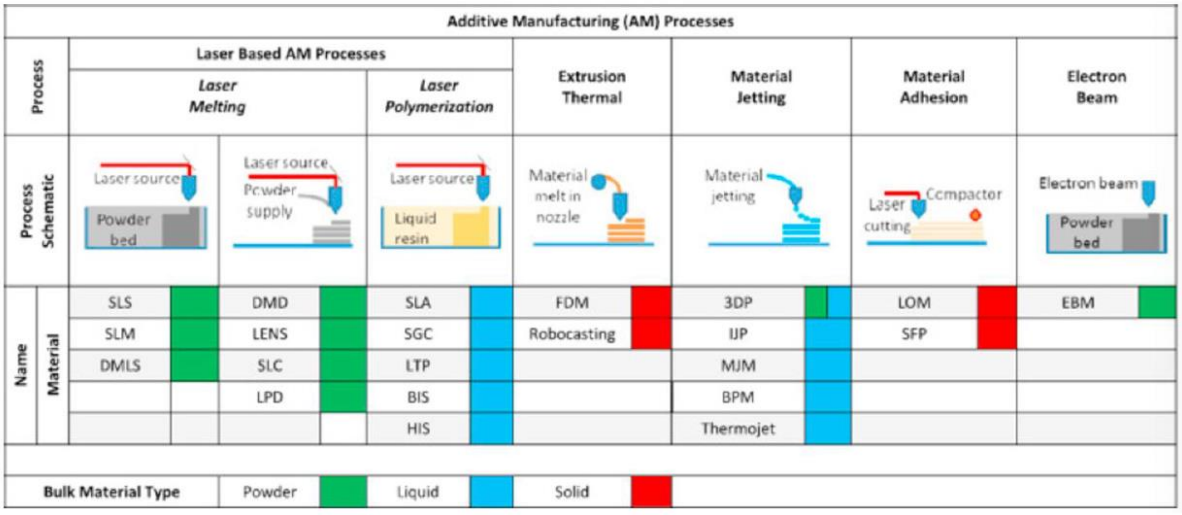

Figure 7. Current additive manufacturing technologies (1).

material fusing to create layers. Laminated Object Manufacturing (LOM) is a process that build object by cutting single layer of membrane into cross-section, then bonded it together by heat and

pressure (30). In the recent years, there has been a rapid growth of additive manufacturing in industry, according to the Wohlers Report 2013 (1) there has been around 25% annual growth of additive manufacturing product and services during last 25 years. From 2010 to 2012 there was a 27.4% market growth rate which reached $2.2 billion. The sold industrial AM system which cost less than $5000 was increased by 19.3% in 2012, and AM systems which cost more than $5000 was increased by 46.3% in 2012. Moreover, there are more additive manufacturing processes have been invented shown as figure 8 below:

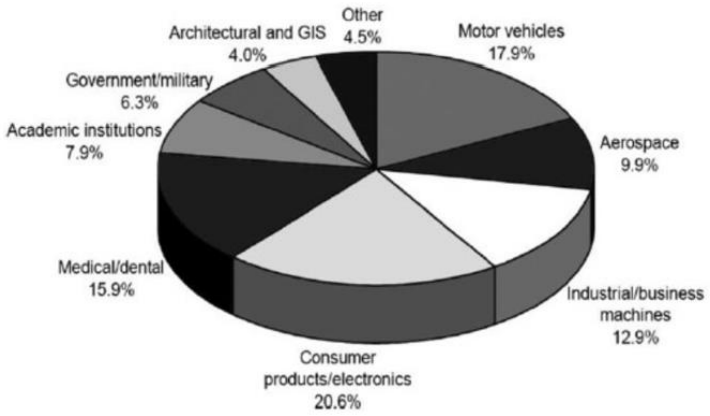

Figure 8. Additive manufacturing in industrial distribution (Wohlers Report 2013 (1)).

Application of 3D printing usually suitable for relatively low production volume, small size and complex design. For example, when the production volume below 1000 unit, 3D printing is cost effective with plastic injection moulding (33). Moreover, additive manufacturing technology is applied in a wide range of industries including the motor, aerospace, medical and architectural.

To simulate the power transmission of the gear there are two main stages: static simulation and dynamic simulation. Haidar F. AL-Qrimli (23) simulated a single spur gear meshed with a single tooth shaped rigid body, which is able to provide a relatively accurate result of an instant moment

of stress acting on a certain position. However, in this static simulation, the Hertz effect was not fully represented due to the different in mechanical properties between a rigid body and gear body. Moreover, a full cycle of the gear tooth contact was not carried out. Johns simulated more accurate gear pair with rotation which could observe full meshing cycle of the gear tooth, In the report, different effects of misalignment were also carried out (34). There are limited reports regarding to the dynamic and thermal effect of the polymer spur gear. According to Xin (24) there is a heating point located on the side of gear, aimed at to analysing the heat flow within the gear body. In this simulation, some cracks were generated to analyse the heat transfer in the cracks. However, this report was only focused on how the cracks affected the heat transfer and could not represent the heat generated by the friction of the gear tooth. Hence, the aim of this research is mainly to simulate the mesh of polymer spur gear with dynamic affect and thermos effect. Furthermore, A model has been created which could predict the failure by three different dynamic effect including thermal simulation, wear simulation and fatigue simulation (29).

2.5 Additive manufacturing of polymer spur gear.

For particular applications such as in automotive and aerospace engineering, polymer gears have unique advantages over metal gears, such as: low cost and weight; high efficiency; quietness of operation; functioning without external lubrication; etc. The characteristics of wear and thermal behaviour of injection moulded gears have previously been studied (35), however, additive manufacturing (AM) and 3D printing processes have become increasingly popular for production of polymer components. It is generally understood that 3D printing is cost effective if production volumes are below 1000 units in comparison with plastic injection moulding (33). The technology has been applied in wide range of industries, including the automotive, aerospace, medical and

architectural industries (36). The nature of 3D printing means that the process is inherently linked to the materials used and each 3D printing technology has a subset of materials that it is compatible with. For Fused Deposition Modelling (FDM) for instance there are many different materials available on the market including polylactic acid (PLA), acrylonitrile butadiene styrene (ABS), polycarbonate (PC), nylon and many others (37). Due to the increased interest in 3D printing there is an increasing amount of research regarding the direct mechanical properties and thermal properties of 3D printed materials and their modification. Leigh et al (38)introduced a low-cost conductive composite material for 3D printing of electronic sensor. Christ et al (39) increased the elastic strain of polyurethane through addition of multi wall carbon nanotubes. Blok, et al (40)claimed that adding continuous fibers could further increase the tensile strength compared with carbon fibre nylon composites. Kalin et al. (41) claimed that gear performance and durability could be affected by thermal properties with the result showing an increase in operating temperature could decreasing the life cycle of the gear. Hu and Mao (42)investigated misalignment effects on acetal gears together with wear behavior, with the results demonstrating that acetal gears were most sensitive to pitch misalignment.

ABS FDM filaments have for instance been reinforced by Montmorillonite (OMMT) with the mechanical properties and thermal properties such as tensile stress, elastic modulus and thermal expansion increasing as the percentage of composite loading is increased (43). Torrado et al. (44) evaluated the mechanical properties of eight different ABS-based polymer matrix composite with different build orientations. The results showed the anisotropy in mechanical properties and variation in the mechanical properties across the range of different ABS materials. Moreover, ABS: Ultra-high-molecular-weight polyethylene (UHMWPE) Styrene-ethylene-butylene-styrene (SEBS) composites showed a reduction in anisotropy. Gupta et al (45) introduced a numerical

method to evaluate the mechanical properties of a carbon nanotube (CNT) reinforced PEEK matrix. Moreover, the reaction stress between the host polymer and carbon nanotubes was simulated, with the results stating that CNTs could directly affect the mechanical properties of PEEK. Singha et al (46) state the current issues in additive manufacturing with more focus on the rigidity of 3D printed parts. There was also some further investigation regarding the increase in mechanical performance by adding carbon fibres into filaments and showing dramatic increases in rigidity (47), (48). Tavcar et al. (49) investigated life time tests for several types of material and reinforced materials including Nylon, 6 Nylon 66, POM and PPS, with the results showing reinforced materials could survive more cycles if lubrication was applied. Santos et al. (50) established that higher crystallinity could increase elasticity when polymers are heated up beyond glass transition temperature. Moreover, higher crystallinity is coupled with stronger intermolecular forces which makes the polymer harder but more brittle, with amorphous regions within polymer providing plasticity and impact resistance (51).

In the above published studies, static forces applied to test samples can provide relatively accurate static mechanical properties, however other methods are required to evaluate more complex dynamic contact problems as might be encountered in components such as polymer gears. For 3D printed gears it is important to understand gear performance under set load conditions, their complex thermal mechanical behaviour their hyper elastic and visco elastic behaviour. Conventionally, polymer gears are produced using injection moulding but surprisingly to date there are have been very few studies published on the topic of 3D printing of polymer gears, perhaps due to mistrust or preconceptions about their potential mechanical performance.

2.6 Performance optimisation of 3D printed gear by machine leaning methods.

According to Ye et al (52) 5 different 3D printing nylon material has been compared, result shown nylon 618 has outstanding performance compare with other nylon materials, including 23% carbon fiber reinforced nylon filament (Which originally manufactured by filament supplier). There have been many investigations into the characteristics of wear and thermal behaviour of injection moulded gears. Mao et al. (35) carried out analysis of the friction and wear behaviour of acetal and nylon gears including characterising the failure mechanism and thermal analysis. The results showed the operational time of polymer spur gears under different circumstances. Hu and Mao (42) investigated the effects of different misalignments on the fatigue of polymer gears during use. Hooke et al (53) proved that increases in the surface temperature can dramatically increase the wear rate of the gear tooth. Moreover, Gauvin et al (54)carried out an investigation into the maximum surface temperature experienced by polymer gears without lubrication. Mao et al. (55) introduced a new method to predict the surface temperature of acetal gears and found the correlation between fatigue life and tooth size. Additive manufacturing (AM) and 3D printing processes have become increasingly popular, with the application of 3D printing usually suitable for relatively low production volumes, small size parts and complex designs. It is generally understood that 3D printing is cost effective if production volumes are below 1000 units in comparison with plastic injection moulding (33). The technology has been applied in wide range of industries, including the automotive industry, aerospace, medical and architectural (36). There is limited research on dynamic performance of 3D printed polymer parts, however, there are several investigations regarding the parameters which affect the mechanical and thermal properties. Chacon et al. (56) has investigated the effect of process parameters on mechanical performance of PLA in terms of on-edge orientation, layer thickness and feed rate. It has been shown that higher

printing speeds can increase the mechanical performance of printed parts. Giovanni (57) carried out Taguchi experimental design for fatigue analysis of PLA and claimed that infill percentage had the most influence on fatigue life. Kuznetsov et al. (58) claimed that printing temperature and printing speed could dramatically dominate the mechanical properties of the 3D printed part. Moreover, the thermal conductivity of 3D printing filaments can also affect the properties of the object (59), increasing or decreasing the bond quality between each layer during fused deposition modelling (60), (61). In order to understand the complicated interplay between these different process parameters and to select the most appropriate parameter set for production of 3D printed gears a multiple regression process is required.

Multiple regression process could be achieved by machine learning methods, however, there are extremely limited research regarding machine learning associated with predicting performance of gears and only some on its application to 3D printing processes. Fracture behaviour of 3D printed material has been shown to be dramatically different compare with other materials (62). Deng et al. (63)introduced optimisation methods to the multi-factor printing of a ceramic slurry by using artificial neural networks. Koeppe et al. (64) used neural networks to analyse load distribution in 3D printed lattice-cell structures. Delli and Chang (65) used supervised machine learning to do real time monitoring of 3D printing to eliminate printing time and waste. Those research reports have provided valuable results in terms of static force analysis and monitoring of the 3D printing, however, dynamic analysis of 3D printed parts requires further investigation. Li et al. (66) has introduced a method using support vector machine to predict dynamic contact characteristics for helical gears. Shouli Sun et al. (67) used neural networks to optimise and predict a gear hobbling process to improve the efficiency and reduce cost. Sun et al. (68) used artificial neural networks and support vector machines with genetic algorithms to monitor the faults in gears. To find the

correlation of 3D printing process parameters and dynamic performance of polymer gears would be of significant benefit to researchers both in the fields of 3D printing and gear manufacture in to increase the efficiency of the 3D printing process and quality of the resultant 3D printed spur gears.

Performing multi-parameter regression has many challenges, for example missing data, and data noise, as well as high dimensionality which impact the ability to identify the relations between parameters (69). Through ordinary mathematical solutions, it is extremely computationally complex to solve multi-target modelling and targets often may not correlated. However, by using some base-line methods such as gaussian processes, neural networks or support vector machines, the complexity of the problem can be much reduced (70).

2.7 Machine learning methods.

2.7.1 Machine learning

Implementing suitable machine learning methods could help to analyse different 3D printer parameters to achieve prediction and optimisation of the gear wear rate. Algorithms are the core of machine learning (71). In 1950s , Turing published "Computing Machinery and Intelligence" that initiated the conception for the future research of machine learning (72). In 1957, Rosenblatt presented the notion of perception, which is the foundation for the neural network algorithm and the SVM algorithm (73). In 1967, Cover proposed another important machine learning algorithm called k-nearest neighbour method (74). In 1970, Winston raised learning structure theory , which promoted the development of symbolism learning algorithm (75). In 1980s, ANN Algorithm was the mainstream technology (76) because Rumelhart proposed BP Algorithm, which significantly promoted the progress of ANN Algorithm (77). At the same time, based on information theory, Iterative Dichotomiser 3 (ID3) algorithm (78) was proposed by Quinlan an Classification And Regression Tree (CART) algorithm (79) was put forward by Breiman, which formed DT

algorithm. In 1990s , SVM algorithm became the mainstream technology in spite of it was firstly proposed in 1970s by Vapnik (80) combining with the theory of VC dimension , Experience Risk Minimization Principle (81). and Structural Risk Minimization Principle (81). Until 1990s, VaPnik came up with Statistical Learning Principles (82). Vapnik and Boser (REF) combined kernel method improved the non-linear support vector algorithm, which make the SVM can perform better with minor data to solve non-linear problems as well as high dimension pattern recognition (83). Hence from the middle of 1990s this algorithm was extensively used in machine learning field (84). In 2000s, ANN algorithm again became one of dominant technologies because, in 2006, Hinton presented the conception of Deeping Learning that is actually a kind of ANN that contains hidden layers and Lecun raised Convolutional Neural Network that was the first real Deeping Learning algorithm (85) which hugely enhance the development of ANN (86).

2.7.2 Support Vector Machine

Now the SVM is the most popular machine learning algorithm applied in geotechnical engineering. The SVM is a new data mining approach based on statistical learning principles. It can effective deal with regression and pattern recognition issues and it also can be applied in prediction and stability assessment aspects (87). The SVM mainly has three advantages: 1. It can use kernel function to realise the non-linear mapping from the raw space to high dimensional space; 2. It can utilize small number of sample data to achieve accuracy prediction; 3. Few support vectors determine the final outcome as a result the complexity of calculation depends on the number of support vectors rather than the dimension of sample space (88).

2.7.3 Support Vector Machine Classification

The SVM is a binary classification model, which is able to establish a hyperplane to divide sample data to achieve structural risk minimization based on maximum margin principles. Due to the introduction of the kernel function the SVM is capable of solving no-linear partition (89). The kernel function has the capacity to map the samples in low-dimension space to high-dimension

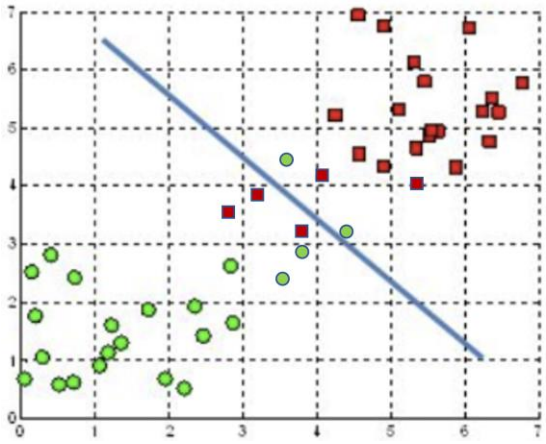

Figure 9. Sample data in two-dimension plane

space to address no-linear issues. In practical applications, many raw samples data space do not exist a hyperplane to divide the sample data in it correctly. For example, as the sample data in the two- dimension plane in Fig.9. It is impossible to find a line to separate the sample data correctly.

However, the kernel function is able to map the sample data in the two-dimension plane to three dimension or higher dimension space and finding a hyperplane in high dimension space divides the sample data. For instance, the sample data in the two-dimension plane are mapped to a three-dimension space in Fig 10.

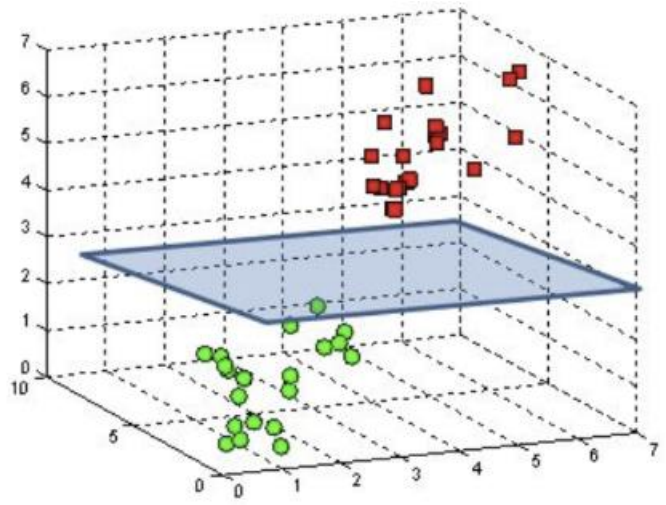

Figure 10. Sample data in three-dimensional space

It is obvious that a two-dimension surface in the three-dimension space can be found to divide the sample data by two groups, but there are numerous surfaces in the three-dimension space that can divide the sample data by two sets. How to determine the optimum hyperplane is another problem that the SVM needs to solve. The SVM principle seeks the optimum hyperplane based on the Margin Maximization. The Margin Maximization Principle refers to looking for a hyperplane that has the largest distance with that sample points which have the smallest distance with it as the optimal hyperplane. The sample points that are nearest to the optimal hyperplane are called Support Vectors, and the distance between the support vectors and the optimal hyperplane is known as Margin (90). As shown in the Fig 10.

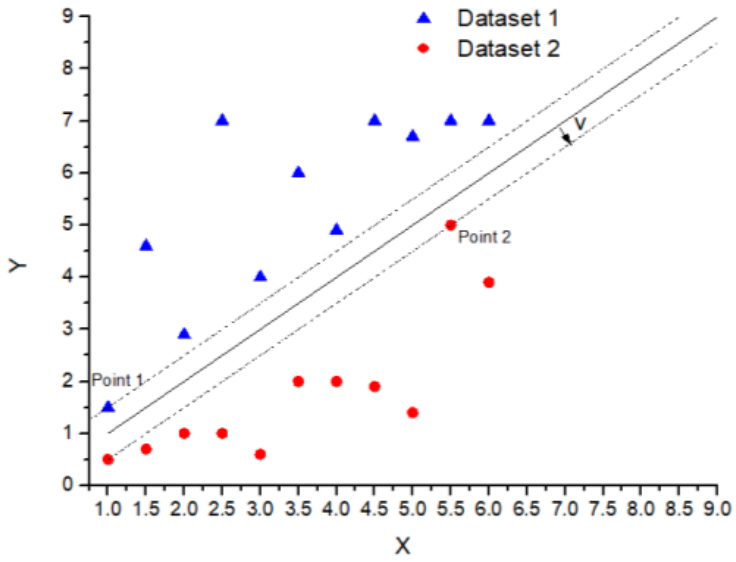

Figure 11. The schematic of the Support Vector Machine.

The support vectors for the optimal hyperplane are Point 1 and Point 2 , and the margin is v . Hence the issue of seeking the optimal hyperplane transfer to the matter of calculating the minimum value of the Margin v that is a function of the coordinates of sample points (Eq. 1).

$$y_i(\mathrm{v} * x_i - b)\text{-}1=0, \quad i=1,2,.....n \tag{1}$$

where, b is constant.

In order to be convenient to calculate, finding the minimum value of *v2* often is adopted to replace the computation of the least of *v*. Hence the classification issue for the SVM is converted to solve the matter for the convex quadratic programming (91). The process of solving the issue of the

convex quadratic programming is rather complex. In order to simplify the procedure of obtaining the optimal solution of the convex quadratic programming matter, the Lagrange multiplier method is adopted to transform the primal issue to its dual problem, as shown from Eq. 2 to 4.

$$L(v,b,a) = 1/2\|v\|^2 + \sum_{i=1}^{n} a_i(1 - y_i(v^T x_i + b), \tag{2}$$

$$\min_a 1/2 \sum_{i=1}^{m}\sum_{j=1}^{m} a_i a_j y_i y_j (x_i * x_j) - \sum_{i=1}^{m} a_i \tag{3}$$

$$s.t. \sum_{i=1}^{m} a_i y_i = 0, 0 \le a_i \le l, i = 1, 2, ...N \tag{4}$$

where, *a* is constant.

Hence through solving the simplified mutable problems, the optimal hyperplane is obtained.

2.7.4 SVM Regression

Another important function of the SVM is to solve the regression problem. Regression problem refers to determining a regression model to describe the relationship of given sample data, as shown in Formula 5.

$$L = \{(x_1, y_1), (x_2, y_2), ...\} \tag{5}$$

where, L is regression model, $x_i(i=1,2.....n)$ is the x value of the sample data, $y_i(i=1,2....n)$is the y value of the sample data.

To gain a regression model indicates the relationship between x and y (92). The principles and methods are adopted to solve the regression problem as that of the classification issue. The SVM can utilise few sample data to build a regression model based on the structural risk minimization principle (93). The optimal regression model means the difference value between f(x) and y is

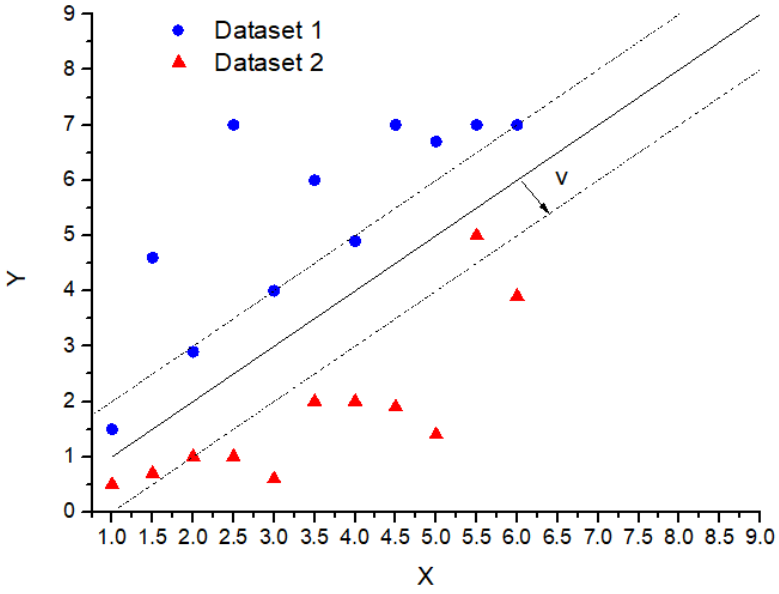

Figure 12. The schematic of Support Vector Machine regression

the least. The Support Vector Regression assumes that deviation value between f(x) and y that is less that s can be ignore when calculating the total difference value between f(x) and y, which manifests that only the deviation value that is larger than s is able to be reckoned in the total difference value (94). As shown in Fig 12.

The deviations that are caused by the points in the area are omitted, and only the deflections that are result from the points that outside the region are included. Hence the problem of Support

Vector Regression can be converted to the matter of searching minimum value, as shown in Formula 6.

$$\min_{v,b} 1/2\|v\|^2 + s\sum_{i=1}^{n} \ell(f(x_i) - y_i) \tag{6}$$

where, *s* is constant.

This function is called s-incentive loss function. (95). Hence the Support Vector Regression issue is transformed to the matter of solving the convex quadratic programming. Regarding the linear regression problem, as that of the classification problem, the Lagrange Multiplier Method is adopted to convert the primal problem to its dual problem to simplify the calculation of it, as shown in Formula7.

$$\max_{\alpha,\hat{\alpha}} \sum_{i=1}^{n} y_i(\hat{\alpha}_i - \alpha_i) - \varepsilon(\hat{\alpha}_i + \alpha_i) - 1/2\sum_{i=1}^{n}\sum_{j=1}^{n}(\hat{\alpha}_i - \alpha_i)(\hat{\alpha}_j - \alpha_j)x_i^T x_j \tag{7}$$

$$s.t.\sum_{i=1}^{n}(\hat{\alpha}_i - \alpha_i) = 0, 0 \le \alpha_i, \hat{\alpha}_i \le b$$

Then through solving the equation of the more complex problem. The optimal regression model is obtained, as shown in Formula8.

$$f(x) = \sum_{VM}(b_c - b_c^*)(x * x_i) - b \tag{8}$$

For the nonlinear regression problem, like that of the classification matter, mapping the nonlinear sample data from the low dimension space to the high dimension space by the kernel function converts the matter to the linear issue. Afterwards using the same procedures of solving the liner problem finds the optimal regression model of it.

2.7.5 Hopfield Networks

The Hopfield network is a symmetrically single layer full-feedback network, which can be divided by Discrete Hopfield Neural Network(DHNN) and Continuous Hopfield Neural Network （CHNN） based on various activation functions (96). Now a majority of applications of the Hopfield network adopt the DHNN. The activation function of the DHNN is the ramp function. The weight matrix of the DHNN is determined by weight design of Lyapunov function. The weight design of the Hopfield network is achieved by the cyclic operating the network to finally converge to a balancing point that is memorised by the network, namely the stable point of Lyapunov function. Since the minimal value of a function is the table point, the key of the Hopfield design is to choose weight matrix W and the deviator vector b to get the minimal value of Lyapunov function. Hence the issue of solving the balancing point of the Hopfield function is transformed to the matter of solving the minimal value of quadratic function (97). The DHNN has three major advantages: firstly, it has good astringency. Secondly, balancing points of it are finite. Thirdly, it has favourable stability (98).

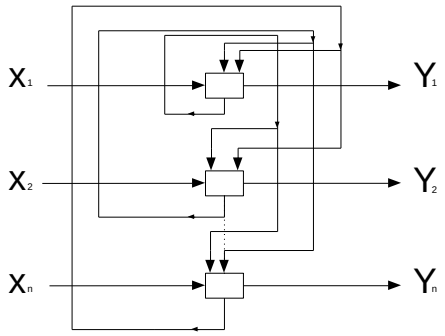

Figure 13. The schematic of the Hopfield network

2.7.6. DT network

The DT is a tree structure that can automatically classify and predict data. The DT consists of nodes and directed edges. There are two kinds of nodes : internal nodes and leaf nodes, and the internal node represents a characteristic as well as the leaf node denotes a category(101). It adopts the top-down recursive approach to compare the attribute value of the internal nodes in the decision tress, and the downward branch is determined by based on attribute value. The conclusion is gained from the leaf node(102). The DT algorithm has three major advantages: firstly, it is easy to understand and realise. Secondly, the volume of the sample data that the DT requires is not large. Thirdly, it is simple to evaluate the DT model by static tests and get the reliability of the model (103).

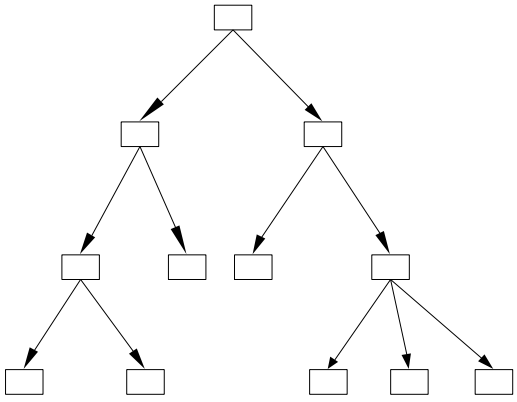

Figure 14. Schematic of the DT

The DT is able to employ a variety of algorithms to conduct classification operation, such as ID3, C4.5,C5.0 , PUBLIC, rough set, CART classification approach and the like (104). These algorithms adopt diverse sorting criterions to carry out classification operation. The ID3 algorithm uses the Information increment as the group standard, which can make the entropy of the system smallest when classification is completed(105). C4.5 and C5.0 algorithms introduce the gain ration to improve on the shortcomings of the largest increment tending to Multi-Valued Attribute in ID3.0 algorithm and they also is able to address continuous attribute(106). The CART classification mean utilises the shortest distance Gini index criterion to classify data, which can solve over-fitting problems(107). The PUBLIC algorithm employs calculating Gini index technique to classify samples, which is able to significantly improve the calculation efficiency(108). The rough set algorithm utilises core attribute as classification standard, which sorts the problems of repeated subtrees(109).

2.7.7 SOM network

The SOM network is a competitively learning ANN network without supervision, which can map input data in high dimension space to low dimension space without changing the topological structure of input data in high dimension space (99). SOM network is composed of input layer and competitive layer, and the neural in input layer and competitive layers fully interconnects. The training method of the SOM network is that firstly the sample data are input into the network, then the neural in competitive layer would calculate the gap between the sample data and its own weight

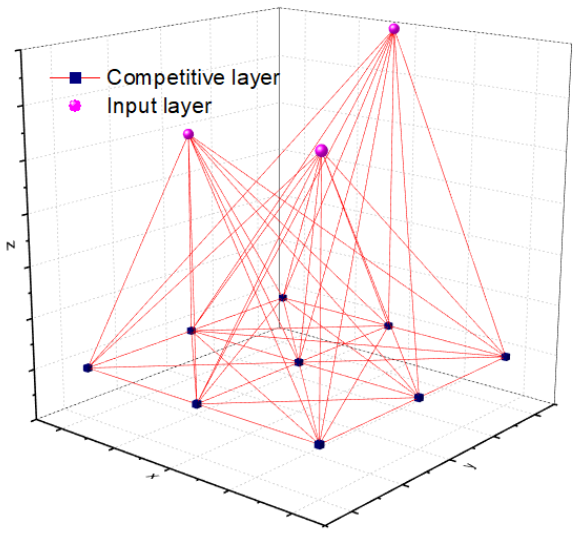

Figure 15. The schematic of the SOM network

vector, and the neural that has the smallest gap would become the best matching unit. After that the weight vectors of the best matching unit and the neural that is near it would be adjusted to make the gap between the sample data and the weight vectors become the smallest. The process constantly iterates until the model converges (100).

2.7.8. The DT regression, principles of the DT regression

The procedure of CART is composed of the feature selection, the generation of trees and pruning(110). The generation of regression tree is based on the Empirical Risk Minimization of

the square error. The process of generating the regression tree is similar to that of the classification tree each node of the regression tree would corresponds to a predicted value. Firstly, the input space of the regression tree is divided based on the minimization of the mean square error to find the best break points. secondly the classification with the least mean square error has been defined as the most reliable one. Thirdly, The classification would end until the value of each node is unique or reaches expected expired criterion(111). finally, pruning is conducting, which means the average value of each node of the regression tree with the least loss function is selected as the predicted regression value of testing samples. The process of pruning can guarantee the balance between the complexity of the model and fitting accuracy

2.8 Materials influence on 3D printed gear.

The performance of 3D printed gear has been investigated previously. According to Ye et al (52) 5 different 3D printing nylon material have been compared, with the result showing that 618 has an outstanding performance compared with other nylon materials, including 23% carbon fiber reinforced nylon filament. Moreover, there has been an increasing amount of research on improving 3D printing parameters cross different areas; Ratiporn and Sorawit carried out an optimisation method to enhance the mechanical properties of stereolithography using Taguchi methods(112). It has been found that the post cure temperature significantly influenced on flexural stress and hardness. The bonding force between polymers and nano composites and textiles has shown that the bonding force was affected by printing temperature, printing speed and different printing process (113). Yi Wei et al. carried out an investigation regarding the effect of printing parameters in 3D concrete printing. Several 3D printed structures was tested, and a fractural test was performed, with the result showing that the nozzle travel speed and material volume flow rate

significantly affected the solidity ratio of the filament (114). Nevertheless, there are increasing numbers of investigations on optimising parameters when printing polymers. Chacon (115)carried out an investigation regarding the effect on processing parameters from on-edge orientation, layer thickness and feed rate on mechanical performance of polylactic acid (PLA). It has been demonstrated that higher printing speeds can induce the better mechanical performance of printed parts. Giovanni (116) carried out Taguchi experimental design for fatigue analysis of PLA and claimed that infill percentage had a major influence on fatigue life. Kuznetsov (117) claimed that printing temperature and printing speed could dramatically affect the mechanical properties of the 3D printed part. Moreover, the thermal conductivity of 3D printing filaments can also affect the properties of the objects (118), increasing or decreasing the bond quality between each layer during fused deposition modelling(119) (120).

Microstructures such as crystallinity, size of the crystallinity domain and different phase of crystallinity could also have a significant effect on mechanical performance. Kennedy has claimed that crystallisation of polymer could be an influence on tensile deformation (121). Giovanni et al. meanwhile analysed the stereo-regularity of different types of polymer structures Showing the obtained result revealed that lower crystallinity or less stereospecific polymerization could lead to lower values of the Young modulus, and lower values of the stress at every strain, easy deformability and viscous flow at very high deformation (122). In addition, the thickness of amorphous located in between the lamellar crystals with various preferred orientation could also influence to the polymer mechanical properties (123). Different types of branching such as methyl or longer branches could define the crystallinity and mechanical properties of polymers as well as the distribution of the branch type (124, 125).

Chapter 3. Methodology

3.1 Computational simulations.

A finite element methods simulation was carried out by computer software named Abaqus. Abaqus FEA (formerly ABAQUS) is a software suite for finite element analysis and computer-aided engineering, originally released in 1978. According to the Reddy (126), FEM is a method that could estimate the solution to boundary value problems for partial deferential equations. FEM divided relatively complex problem into smaller and simpler elements, then calculated each small problem and converge all the small problems to estimate the final value of whole problem. The Abaqus product suite consists of five core software products and in our polymer spur gear simulation there are two in use:

Abaqus/Standard, a general-purpose finite-element analyser that employs an implicit

- integration scheme (traditional).

Abaqus/Explicit, a special-purpose finite-element analyser that

- employs an explicit integration scheme to solve highly nonlinear systems with many complex contacts under transient loads.

In order to reduce the weight of the gear and computational cost of the simulation, it is plausible to reduce the volume of the gear by shape optimisation. Shape optimisation refers to reduce the material which carried less stress. Gear shape optimisation uses software called Fusion360 （a software could clearly indicate which part of the gears carried less torque and can be removed）. which allow the load distribution within the gear will be analysed and the part with lower load will be removed.

3.2 3D printed polymer gear.

3.2.1 Gear Design

The first stage in 3D printing of a polymer spur gear was to design the gear itself. The gear design selected was similar to the injection moulded

gears used in a previous study (35). The gear tooth face width was reduced by 2mm due to test rig specifications. The specifications of the final gear are given in figure 16.

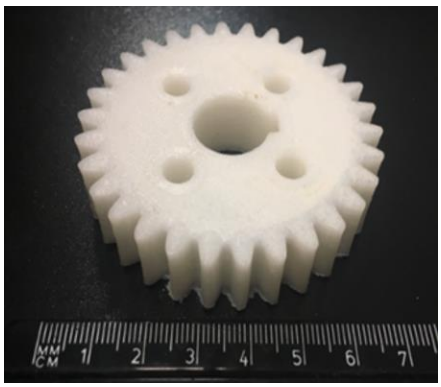

(a)

Module	2mm
Tooth number	30
Pressure angle	20°
Face width	15mm
Nominal backlash	0.18mm
Tooth thickness	3.14mm
Contact ratio	1.65

(b)

Figure 16. Additive manufacturing in industrial distribution.

Five different 3D printed nylon materials were tested and compared with injection moulded nylon gears including nylon 618, nylon 645, alloy 910, Onyx, and Markforged nylon. The different materials were printed using two different types of 3D printer. Nylon 618, Nylon 645 and Alloy 910 were printed using an Ultimaker 2 and the proprietary Onyx and Markforged nylons were printed using a Markforged X7 system. Gear inspection has carried been out by KLINGENBERG ZPK 260 gear inspection machine, and the result showed the quality of the gears was DIN 12 （BS D）. All 3D printing parameters were set as default and printed with manufacturer recommended temperature and speed apart from infill percentage, which was set to 60% for both printer systems to start with. Printer settings were matched between the Ultimaker 2 and Markforged systems

where possible. Gear wear tests were conducted with a pair of 3D printed gears with the same geometry and printed using the same settings, with both the driven and driver gear manufactured in same material. Between and during printing, all materials were stored in a dry box to keep moisture away from the materials.

3.2.2 Gear Testing Rig

The gear test rig is designed to test the gear wear whilst the gears are meshed and running. The specific details of the test rig shown as figure 17. 3D printed gears can be tested in much the same way as injection moulded gears, using a back to back test configuration where the gears are loaded by winding in the torque to a prescribed level (35). The schematic of the test rig is presented in figure 17. In this section a step load was applied to the gears at the different levels of 5 Nm, 6 Nm, 7 Nm, 8 Nm, 9 Nm, 10 Nm, 11Nm and 12 Nm. During the step load test, each load was operated for 30 minutes and increased from 5 Nm to 12Nm until the gear was failed (see chapter 4.3 Fig.2 (a)). Gear fatigue tests were performed with nylon 618, nylon 645, alloy 910, Onyx, and Markforged nylon gears. The test rig motor drives the gears with externally applied torque. Torque was simulated by the weight added to the driven shift. The contact force between gear teeth is provided by the weight added to the bearing block and loading arm. This loading method permitted large amounts of wear without significantly affecting the applied torque. To increase the sensitivity of the displacement sensor on the test rig, the displacement sensor was relocated from the pivot block to the weight to create a large reading of the displacement sensor. Gear failure was defined as when a large deformation was recorded by the test rig and the meshed gear tooth jumped out from its original running position.

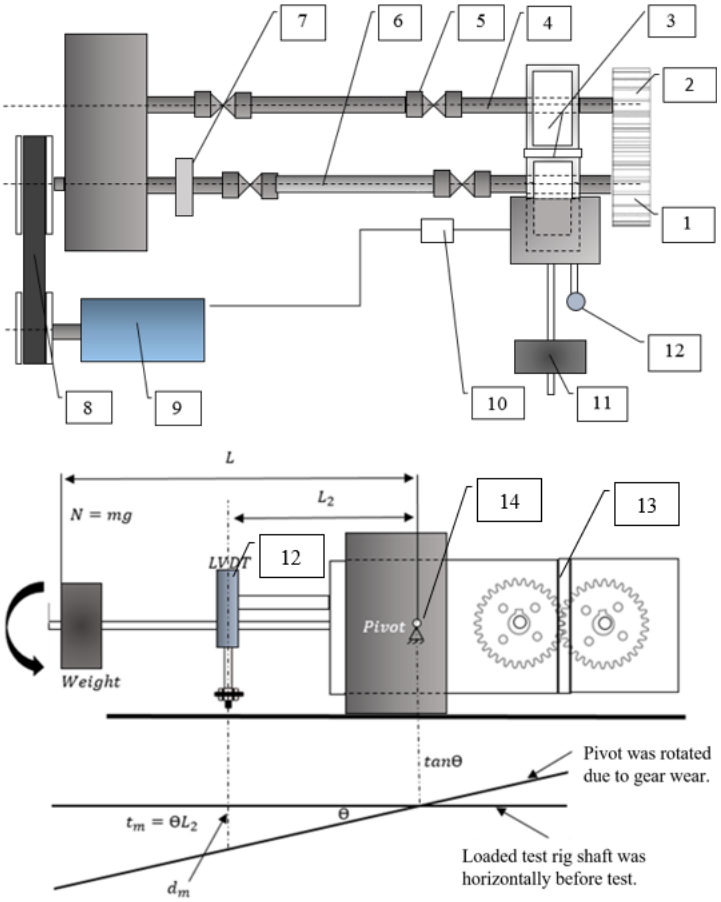

Θ: Rotation angle of the pivot.

t_m: Signal of wear to being magnified

d_m: Displacement measured by LVDT (Linear Variable Differential Transformer)

$L\ and\ L_2$: Distance of pivot between LVDT and weight.

1. Driver gear	2. Driven gear	3. Pivot block assembly.	4. Driven shaft	5. Universal couplings.	6. Driving shaft	7. Conical clutch
8. Pulley	9. Motor	10. Motor controller	11. Weight	12. LVDT	13. Centre spacer	14. Pivot

Figure 17. Schematic of test rig for polymer gears. Ye et al (52)

As figure above shown that total wear value of the gear tooth determined by the LVDT while gear is running, the wear of individual gear tooth hence equal to half of t_m. Wear not directly measured through the rotation of the pivot, it can be represented by the total wear:

$$t_w = d_p \times \cos(\alpha) \times \Theta \ldots\ldots\ldots\ldots\ldots\ldots\ldots\ldots\ldots\ldots\ldots\ldots\ldots\ldots\ldots\ldots\ldots\ldots (9)$$

d_p Represent the pitch circle diameter. α shows the pressure angle of the gear, and Θ is the rotation angle of the pivot. The relationship between rotational angles of the pivot Θ and dm is:

$$d_m = tan\Theta \times L_2 \ldots\ldots\ldots\ldots\ldots\ldots\ldots\ldots\ldots\ldots\ldots\ldots\ldots\ldots\ldots\ldots\ldots\ldots (10)$$

While Θ is derived:

$$\Theta = \arctan\left(\frac{d_m}{L_2}\right) \ldots\ldots\ldots\ldots\ldots\ldots\ldots\ldots\ldots\ldots\ldots\ldots\ldots\ldots\ldots\ldots\ldots\ldots (11)$$

Hence, final wear of the gear tooth will be represented by equation below:

$$t_w = d_p \times \cos(\alpha) \times \arctan\left(\frac{d_m}{L_2}\right) \ldots\ldots\ldots\ldots\ldots\ldots\ldots\ldots\ldots\ldots\ldots\ldots\ldots\ldots\ldots\ldots (12)$$

Moreover, operational time was mainly determined by the wear and wear rate, higher wear rate will cause less operational time.

3.2.3 Gear surface temperature

There are three temperature components contributing to the gear surface temperature: the ambient, bulk and flash temperatures (35). The ambient temperature was between 20 ℃ and 30 ℃ for the different tests. The bulk and flash temperatures were measured during running using a thermal

camera. In order to check that the wear transition, thermal behaviour and mechanical behaviour actually corresponded to the maximum surface temperature during operation reaching the melting point of Nylon (approximately 256 ℃), a number of incremental tests were carried out at elevated surface temperatures. Although the flash temperature is hard to measure, however, with calculation and numerical simulation, it could be estimated with relatively accurate result.

An investigation into the gear surface temperature during wear tests was carried out, with the aim of investigating the gear surface temperature under different loading criteria. A FLIR E4 thermal camera was used and set 10 cm above the testing gears. Surface temperature tests were carried out on Nylon 618 and Onyx gears. The duration of each test was 15 minutes and in the first 10 seconds of each test, an image was captured every 2 seconds due to rapid temperature rise and after the first 10 seconds the thermal image captured every 10 seconds until surface temperature settled with a stable range. The wear can be divided into three phases, a "running-in" period, a linear wear period and a final rapid wear period (35). The linear wear period is most representative of the operational conditions and should reveal the operational temperature of a gear (127).

3.2.4. Differential Scanning Calorimetry (DSC) Analysis.

In order to understand the thermal behaviour of the nylon materials being used and assess if the thermal behaviour of 3D printed filament changed after printing, differential scanning calorimetry (DSC) was performed using a Mettler Toledo DSC 3. The results showed that materials had relatively stable thermal behaviour and high repeatability of heating and cooling after being printed. Due to relatively poor performance in wear tests, alloy 910 and Markforged Nylon were not included in the DSC test. Nylon 66 (as used in the literature study of injection moulded gears) was included in the tests as a comparison material. The other aim of DSC tests was to measure the glass

transition temperature, crystallinity of the materials and enthalpy change during heating. Tests were performed with two cooling cycles and two heating cycles to analyse the repeatability of each heating and cooling cycle. The temperature range of the test was set at -150 ℃ to 320 ℃, with a heating rate of 10.00 K/min. An initial test was carried out with a maximum temperature of 420°C, however, the materials decomposed after first heating cycle, and hence the heating temperature was limited to 320°C.

3.3 Performance optimisation and prediction of 3D printed by Machine learning.

3.3.1 Performance optimisation of 3D printed polymer gear.

There are several stages to complete this dynamic performance optimisation of 3D printed gear. Firstly, use sobol sequence (algorithm) to generated sobol random parameters with 50 data per parameter. Secondly, 50 set of test data was generated, including printing temperature (230°C-275°C), printing speed (20mm/s-75mm/s), and bed temperature (30°C -70°C). Furthermore, bed temperatures refer to the temperature of printing surface which will affect the first few layers during printing. Infill percentage represent how hollow is the gear, the aim of reduce the infill percentage is to reduce the weigh and inertia during operation hence the percentage increasing from 20%-80%. Each parameter was increased by factor of one, for example, for printing temperature was from 230°C-275°C and sobol sequence will be cover entire range increased by unit steps of 1, hence there are in total 45 data of printing temperature alone. Furthermore, apply similar range for each parameter, 50 experiments could potentially cover every combination of each test data which roughly equal to $45 \times 55 \times 40 \times 60 = 5940000$ 3D printing setting possibilities. Then printing gears with Ultimaker 3 extended. Gear will be printed on tufnol bed due to chemical bonding between nylon and tufnol to eliminate the peel off effect during 3d printing process. Table shown the inputs and output. There were 100 gears was printed. Average

printing time around 6 Hours per gear depends on the setting of the parameters. Second stage was placing the printed gear on the gear wear test rig to generate performance life cycle with 10Nm torque. Test then will be recording the wear increasing at the gear tooth and shows different stage of gear operation until gear has been failed. The time from gear start to run on the test rig until the gear has been failed was considering of fatigue time as result. Third stage was using for 3D printing parameter as input and life cycle from test rig as output to create a neural network model of correlations between input and output. In the main time, using Gaussian process to perform multi-parameter regression to find out the approximate likehood of output accuracy. Finally, by using the model which generated by ANN and GP to do a sensitivity analysis to investigate the relations of each multi-parameter. The process is showed as table 1 below.

Table 1. Input parameters generated by sobol sequence and output from test rig.

Testing number	Printing Temp (°C)	Printing Speed (m/s)	Bed Temperature (°C)	*Infill Percentage (%)*	*Test result Gear fatigue time (Hours)*
1	230	25	30	*20*	*0.04*
2	253	50	50	*50*	*20*
3	264	38	60	*35*	*11.11*
4	241	63	40	*65*	*30*
5	247	44	55	*28*	*1.94*
6	269	69	35	*58*	*24.69*
7	258	31	45	*43*	*9.32*
8	236	56	65	*73*	*21.03*
9	238	41	43	*61*	*15.57*
10	261	66	63	*31*	*10.1*
11	272	28	53	*76*	*30.18*
12	250	53	33	*46*	*20.6*
13	244	34	68	*54*	*10.12*
14	267	59	48	*24*	*6.66*
15	255	47	38	*69*	*12.9*
16	233	72	58	*39*	*0.36*
17	234	48	64	*44*	*12.77*
18	257	73	44	*74*	*36.8*
19	268	36	34	*29*	*1.65*

20	245	61	54	*59*	*16.66*
21	251	30	49	*37*	*2.88*
22	274	55	69	*67*	*20.16*
23	262	42	59	*22*	*2.67*
24	240	67	39	*52*	*10.32*
25	237	33	51	*71*	*12.24*
26	260	58	31	*41*	*1.96*
27	271	45	41	*56*	*7.28*
28	248	70	61	*26*	*0.06*
29	243	39	36	*78*	*21.24*
30	265	64	56	*48*	*27.78*
31	254	27	66	*63*	*25.71*
32	231	52	46	*33*	*0.39*
33	232	38	54	*55*	*25.2*
34	255	63	34	*25*	*11.38*
35	266	26	44	*70*	*8.4*
36	243	51	64	*40*	*1.76*
37	249	32	39	62	5.16
38	271	57	59	32	4.17
39	260	45	69	77	34.49
40	238	70	49	47	15.67
41	241	29	62	28	0.07
42	263	54	42	58	14.79
43	274	41	32	43	3.06
44	252	66	52	73	30.45
45	246	48	47	21	0.04
46	269	73	67	51	12.77
47	257	35	57	36	16.38
48	235	60	37	66	32.77
49	234	37	41	79	25
50	256	62	61	49	25.41

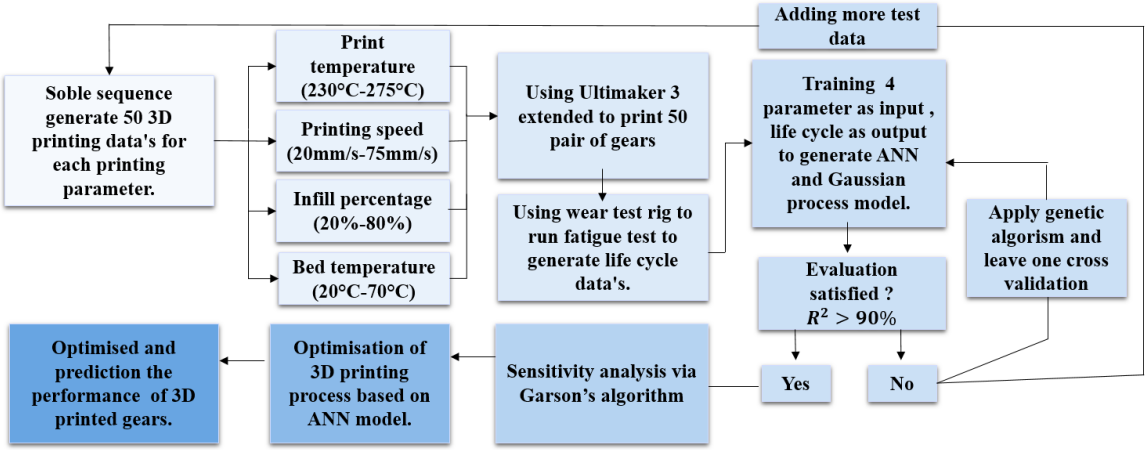

Figure 18. Schematic of 3D printing optimising process

3.3.2 Sobol sequence

Sobol sequence is a method to sampling data in a quasi-random sequence in which data was selected in a uniformly random form. Sobol sequence was first introduced by Russia, mathematician I.M Sobol (128). Sobol's sequence could provide better evenness and higher speed to fill the space within a hyper cube. Sobol's sequence's algorithm had over past 20 years of improvement of the algorithm to apply to high dimension. Hence, sobol's sequence became a best practice in different applications. Sobol's sequence was generated with sobole generator fitted in MATLAB, experiment data of each parameters was generated based on the algorithm of sobol sequence. This code below creates 50 vectors (4 components in each vector) according to a 4-variate uniform distribution implemented (approximately) using a sobol sequence. Each component in each vector is a number between 0 and 1. The command above produces a matrix *'X'* that lines up each of the vectors as a column in the matrix *X*. There are therefore 50 columns and 4 rows.

>>Temperature=225+X(1,:)*50

This takes the first component of each of the 50 vectors and rescales it to get a temperature input value (between 225K and 275K). Basically, use the first row X(1,:) of X

>>Speed=20+X(2,:)*50

Same as above but use the 2nd row X(2,:) of X to get the printing speed values (between 20 and 70rpm).

>>BedT=10+X(3,:)*50

3rd row X(3,:) of X to get the bed temperature values

>>Infill=20+X(4,:)*50

4rth row X(4,:) of X to get the infill values

>>Input(:,1)=Temperature'

Create a matrix called ‘Input’ and make the first column the 50 temperature values by typing the above (you need to transpose the vector of temperature values by using a prime, i.e. ‘)

>>Input(:,2)=Speed'

Second column of Input is the speed value.

>>Input(:,3)=BedT'

Third column of Input is the bed temperature values

>Input(:,4)=Infill'

Fourth column of Input is the infill values.

3.3.3 Artificial Neural Networks (ANN)

Artificial neural networks could simulate of physiological structure and mechanism of human brain. It is a machine learning process which is different from common methods such as signal reasoning and logical thinking approaches (76). ANN is an appropriate method to solve incomplete associative memory and defective characteristics pattern recognition and automatic learning. There are three main reason that ANN is suitable for this project, first of all, the calculation speed of the ANN is significantly computationally cheaper than other methods, and hence, it is computational cheaper than other simulation methods. Secondly, ANN has strong fault-tolerant ability to minimise the uncertainty during the experiments. Thirdly, ANN is adept in addressing the problems with multi-parameter regression which is hard to solve with numerical methods (129). The ANN has four common basic structures: feed-forward model, feed-back model, self-organising competition model, and Back-Propagation (BP) Networks. Hopfield Networks and Self-Organizing Map Networks (SOM) are the most representative networks for corresponding basic structures (130).

3.3.4 Back-Propagation Networks

The detailed stages of BP training method are following: 1. the sample data for training are input to the network. 2. Data moves forward from input stage to each hidden layer until the output stage, then the output data is generated. 3. The difference between input data and output data is compared and if the differences are larger than expected, they will be transferred back to the hidden layer. 4. The weight of each neuron is adjusted based on the deviation via the steepest descent method that means calculating the minimum value (maximum value) of the loss function along the gradient descent (ascent) direction, and the deviation transited to the input layer. 5. The value proceeds

forward again and after repeated iteration, the error constantly diminishes. (6) The training process is over when the gap between the input value and output value is smaller than the expected value.

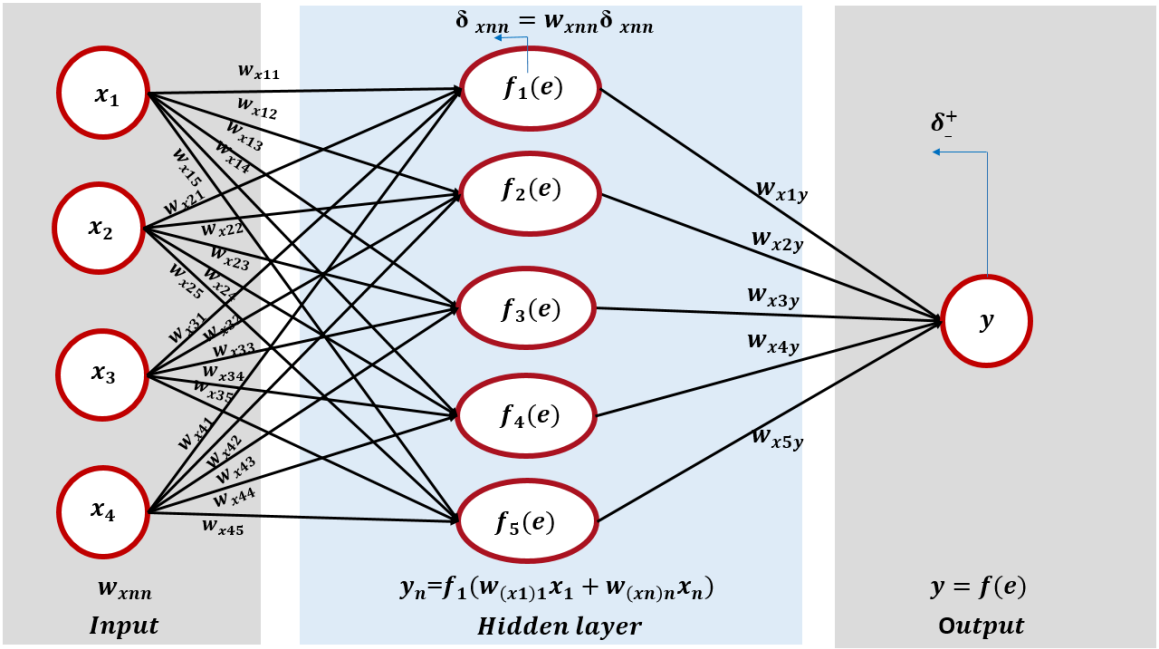

Figure 19. Schematic of ANN structure.

Figure 19 shown the structure of the ANN model. The ANN model in this paper was carried out based on MATLAB Neural network toolbox. Moreover, there is a loop fitted in the model aimed to select optimized hidden number of neural from 1 to 20. Result shows 5 hidden size providing less error. The ANN model in this paper is composed of 4 input layer nodes, 5 hidden layer nodes and 1 output layer nodes. The initial parameters of ANN, such as the connection weights between input layer, hidden layer and output layer, and threshold value of hidden layer and output layer

have large influence on the predictive performance. Due to the small number of training data, best validation performance could be 1.

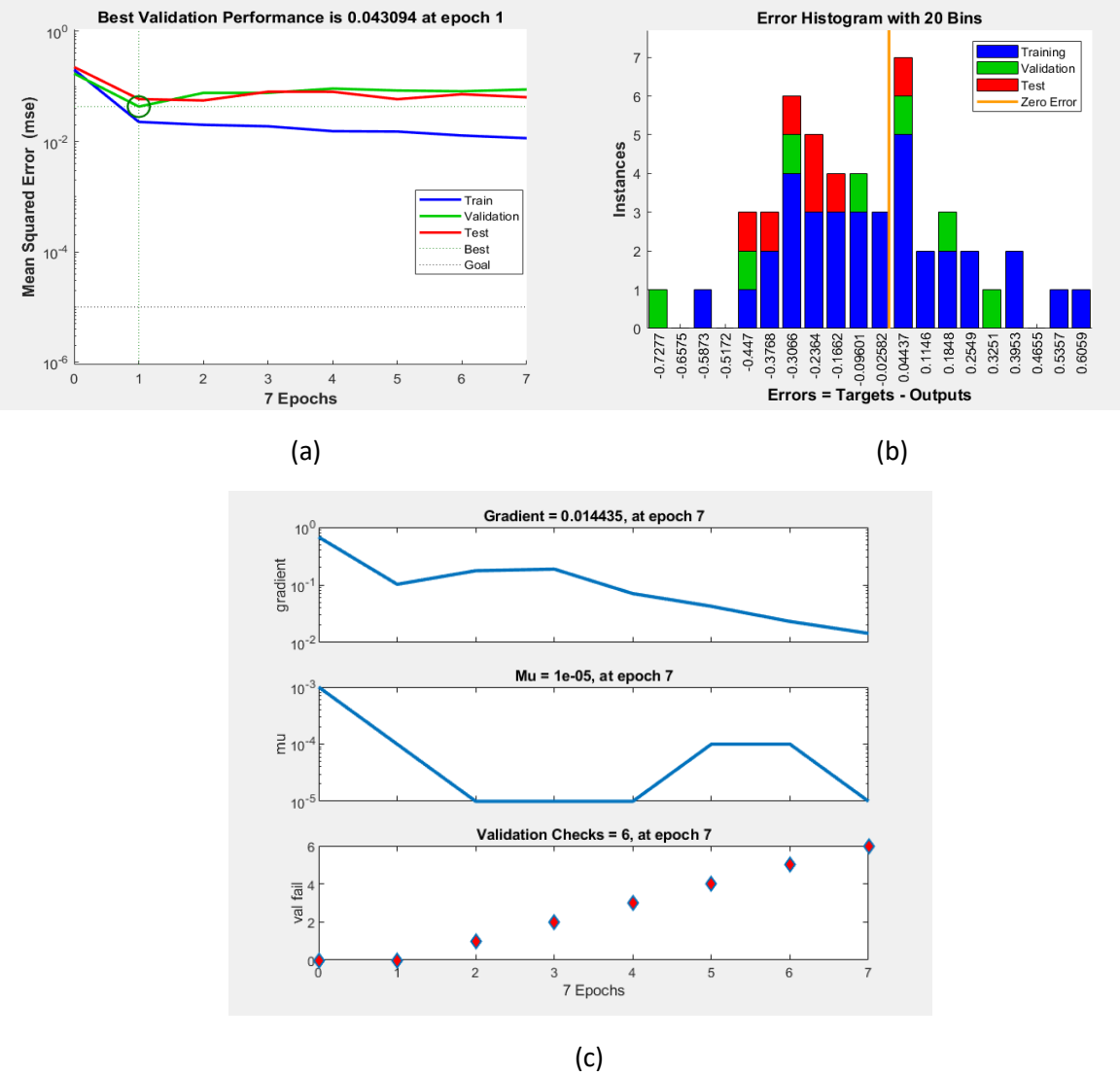

Figure 20. Performance validation of ANN.

3.4 Genetic algorithm (GA)

For the traditional ANN predictive models, without combining optimization algorithms, the initial parameters are determined randomly, which is inefficient, or prone to converging to local optima, slow convergence speed, overtraining, subjectivity in the determining of model parameters and often pose a convergence problem (131). The optimised algorithm GA is able to optimise the initial parameters of machine learning models to increase the estimating accuracy and accelerate the convergence speed of the ANN models (132, 133).

GA is a parallel random search optimisation algorithm to simulate the genetic mechanism of natural and biological evolution GA can conduct efficient heuristic search and parallel computing (134). It introduces the biological evolutionary principle of "survival of the fittest" in the coded tandem population formed by optimisation parameters, and chooses individuals according to the fitness function of the individuals and the operations of selection, cross and mutation to make the individuals with high fitness value be retained, the individuals with low fitness be eliminated (135). The new generation would inherit the information of the previous generation and be superior to the previous generation. This iteration is repeated until the predetermined expired criterion is met (136).

The basic operations of the GA are divided into:

3.4.1 Select operation

The selection operation refers to the selection of individuals from the old generation to the new generation (137). The probability that the individual is selected from the old generation to the new generation is related to the fitness value of the individual. The better the individual fitness value, the higher the probability of being selected (138).

3.4.2 Cross operation

The cross operation refers to the selection of two individuals from the old generation to produce new individuals by randomly exchanging and combination of the chromosomal locations of the two old individuals (139).

3.4.3 Mutation operation

The mutation operation refers to the selection of an individual from the old generation and choosing a point in the chromosome of the individual to mutate to produce a new individual. The basic process of GA as shown in Figure 21 below.

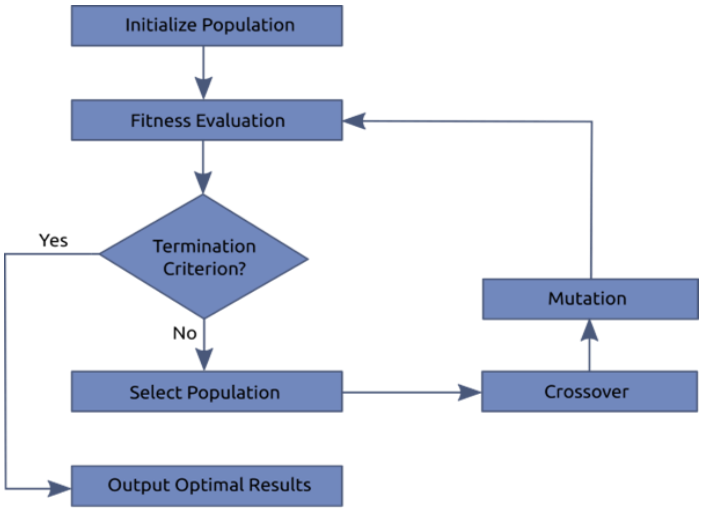

Figure 21. Schematic of GA process (132).

The detailed method of applying GA in improving the performance of ANN is following: the GA is used to optimise the initial parameters of ANN. Each particle in GA contains all information of the initial parameters of the ANN model. According to the fitness function of the individuals and the operations of selection, cross and mutation to make the individuals with high fitness value be retained, the individuals with low fitness are eliminated. This iteration is repeated until the

predetermined expired criterion is met. The initial parameters of the particle with the highest fitness are assigned to the ANN model. The objective function (fitness function) is the R-square. The crossover coefficient of the GA algorithm is 0.2, the mutation coefficient is 0.2, the size of population is 100, the maximum iteration number is 100.

3.3.5. Leave-one-out cross validation

Leave-one-out cross validation is the method which evaluate the performance of a machine learning algorithm, in this case is ANN. It is suitable for giving data set and output has relatively limited number. It could increase the prediction accuracy by increasing the training data point to 49 and decrease the test data point to 1. Hence, Leave-one-out cross validation could eliminate the randomness of dividing instances into for training and testing. By changing the ratio of training and testing of AAN could maximised the training algorism to provide a better understanding of model and clearer pattern of sobol sequence (140). Due to small amount of data, it is plausible to maximise the number of the training data.

3.3.6 Garson's algorithm

Based on the established machine learning models, the sensitivity analysis of the input parameters is conducted by adopting Garson's algorithm. In 1991, Garson proposed Garson's Algorithm(141, 142), later modified by Goh (1995), for determining the relative importance of the input parameters to the output parameter (139, 143-145), the equation of Garson's Algorithm as shown in Equation 5, the results of the sensitivity analysis by using Garson's Algorithm as shown in Eq 13.

$$R_{ij} = \frac{\sum_{j=1}^{L}\left(\left|W_{ij}W_{jk}\right| / \sum_{r=1}^{N}\left|W_{rj}\right|\right)}{\sum_{i=1}^{N}\sum_{j=1}^{L}\left(\left|W_{ij}W_{jk}\right| / \sum_{r=1}^{N}\left|W_{rj}\right|\right)} \quad (13)$$

Where R_{ij} is the relative importance of input parameters, W_{ij}, W_{jk} are the connection weights of the

input layer-hidden layer and the hidden-output layer, i= 1,2….N， k=1,2….M(N, M are the numbers of the input parameters and output parameters).

3.4 Material analysis of 3D printed gear.

There were two focus on optimisation of 3D printing parameters, firstly, is to investigate the 3D printer parameters setting influences on the dynamic performance of 3D printed polymer gear. 50 pairs of gears were printed and tested on the gear test rig (52). Parameters from 3D printer was optimised and predicted. Secondly, by carried out the different test including Small-angle X-ray scattering (SAXS), Wide-angle X-ray scattering (WAXS), Differential Scanning Calorimetry (DSC), X-ray fluorescence (XRF) and Fourier-transform infrared (FTIR) to investigate the crystallinity, size of the crystallinity domain and different phase of crystallinity to demonstrate the different failure mechanisms.

3.4.1 SAXS/WAXS test

Small Angle X-ray Scattering (SAXS) is a powerful X-ray technique which enables the non-destructive investigation of nanoscale particle size, distribution, and morphology. Typically is an important tool to study the corresponding microstructure parameters of polymers. The one-dimensional data of SAXS is consisted of intensity (Y-axis) and scattering vector (q, X-axis), where $|q| = 4\sin\theta/\lambda$, λ is the wavelength of the incident beam and 2θ is the scattering angle (123). This gave a q range for the detector of 0.009 $Å^{-1}$ to 0.338 $Å^{-1}$. A radial integration as function of q was performed on the 2D scattering profile and the resulting data corrected for the absorption and background from the sample holder. In this research, SAXS measurements were made using a Xenocs Xeuss 2.0 equipped with a micro-focus Cu Kα source collimated with Scatterless slits. The scattering was measured using a Pilatus 300k hybrid photon counting detector with a pixel size of 0.172 mm x 0.172 mm. The distance between the detector and the sample was calibrated using

silver behenate ($AgC_{22}H_{43}O_2$), giving a value of 1.181(3) m. WAXS was measured on a Pilatus 100k mounted at an angle of 36° to the beam direction at a distance of 0.163m. The data was collected as intensity (Y-axis) and 2θ (diffraction angle) basing on the Bragg equation ($2d\sin\theta=\lambda$)(146), while the 2θ range was from 18 to 47˚in our test system.

3.4.2 DSC test

Differential Scanning Calorimetry (DSC) means the measurement of the charge of the difference in the heat flow rate to the sample and to a reference sample while they are subjected to a controlled temperature program (Differential Scanning Calorimetry, Günther Höhne, Wolfgang F. Hemminger, H.-J. Flammersheim). It is a quantitative measurement of phase transitions used to determine transition temperatures, phase composition of materials such as glass transition in polymers, glass/crystal fractions. In the experiment, data was collected via Mettler Toledo DSC 3 with three heating and cooling cycles ranging from -150 to 320℃ in an the atmosphere of nitrogen. The heating/cooling rate was ±10℃·min^{-1} and a standard aluminium crucible with 40 μL volume was used as sample holder.

3.4.3. Element and molecular structure test (XRF and FTIR)

X-ray fluorescence (XRF) supplies simply, accurately and economically analytical ways for the detection of elemental composition of many types of materials including polymers. Herein, a Rigaku Primus IV XRF system was employed, which is advanced and unique wavelength dispersive X-ray fluorescence (WDXRF) equipment and used to analyse products. WDXRF system is based on Bragg's law, which utilizes the phenomenon that crystals will reflect x-rays of specific wavelengths and incident angles when the wavelengths of the scattered x-rays interfere constructively. While the sample position is fixed, the angles of the crystal and detector can be

changed in compliance with Bragg's law so that a particular wavelength can be measured. Only x-rays that meet Bragg's law are reflected. For non-destructive ultra-trace elemental analysis, the Rigaku system can supply total reflection X-ray fluorescence (TXRF) spectrometers as well. Fourier-transform infrared (FTIR) spectrometers can not only be widely used in composition but also molecular structure analysis, which is derived from the basic that bonds between various elements absorb light at different frequencies. Interferometer is utilized to identify samples by engendering optimal signals with all the IR frequencies involved into it. The signal can be tested quickly. After that, the signal is decoded by applying a mathematical technique known as Fourier transformation. This computer-generated process then forms a mapping of the spectral information. Bruker Vertex 70V IR spectrometer utilized a nylon samples test with a frequency range from 4000 to 500 cm^{-1}.

Chapter. 4. Analysis of additive manufacturing polymer spur gear.

4.1 Wear of 3D Printed Gears

During the test, a set of gears were produced in each of the material variants and tested to a maximum of 2.4 million cycles or until gear failure (whichever came first). Whenever a gear lasted at least 500000 cycles in one test, a similar new one was texted at a higher load. Material properties of each tested gear were presented in figure 22, (35) (147),(148),(149),(150). From a visual inspection it appeared that most gear failures were due to the thermal bending of the gear teeth. Interestingly, a high proportion of the Nylon 618 gear failures appeared to be due to failure at the root of the gear teeth.

Figure 22. Material properties of five different materials provided by manufactures.

Material/ Properties	Nylon 66(35)	Nylon 618(147)	Nylon 645(148)	Alloy 910 (149)	Onyx (150)	Markforged Nylon
Specific gravity (g/cm^3)	1.41	N/A	N/A	N/A	1.18	1.10
Tensile strength (MPa)	62	31.5	35.7	55.8	36	31
Flexural modulus (MPa)	2600	152.9	212.7	502.8	2900	840
Glass transition temperature (℃)	51	48	52	82	N/A	N/A
Melting temperature (℃)	256	218	217	210	N/A	N/A

N/A: Data was not provided by manufacture.

The results of the wear tests are presented in Figure 22. The Nylon 66 results of the injection moulded gear performance test is from a literature report and nylon 618, nylon 645, Alloy 910, Markforged Nylon and Onyx values are resultant from the tests on the 3D printed gears. For the 3D printed gears, both Nylon 618 and Onyx gears were relatively stable below 10 Nm, however Onyx gears failed instantly after any load beyond 10 Nm due to dramatic thermal bending and wear. There were two regimes of debris observed, strip-like debris occurred after operation of Nylon 645, Alloy 910, Onyx and MF Nylon. Strip-like debris was also associated with relatively

high operation noise and relatively high wear rate. Snowflake-like wear debris occurred in Nylon 618. The operation noise of Nylon 618 was significantly lower compared with the other 3D printed materials tested. As shown in figure 22, several tests were undertaken on the gears. When a gear failed after less than 1 hour at 5 Nm torque no further tests were carried out, which was the case for MF nylon, nylon 645 and alloy 910. MF nylon gears operated for around 0.018 Million cycles, Nylon 645 gears operated for 0.014 Million cycles and Alloy 910 failed just after 0.0078 Million cycles. Perhaps most importantly, as a comparison, 3D printed Nylon 618 gears performed better than the literature values for an injection moulded Nylon 66 gears in the region below 10 Nm. Nylon 66 gave relatively better performance when torque was applied beyond 12 Nm. It is often incorrectly assumed that 3D printed parts have inferior performance when compared to conventionally produced counterparts, however this result showed that the 3D printed gear performed better than a 'conventionally' produced gear in this low to medium torque regime. In order to further understand the performance of Nylon 618 printed gears, further tests were carried out. The results of the wear tests are presented in Figure 23. Opreational speed of test for figure 23 were 1000 rpm for each each tests.

Figure 23. Wear test rig results

Material/ Load	**Nylon 66** (Injection mould)(35]	**Nylon 618**	**Onyx**	**MF nylon**	**Nylon 645**	**Alloy 910**
5Nm	2.4 Million cycles	2.4 Million cycles	2.4 Million cycles	0.018 Million cycles	0.014 Million cycles	0.0078 Million cycles
7Nm	2.4 Million cycles	2.4 Million cycles	0.96 Million cycles	N/A*	N/A*	N/A*
10Nm	1 Million cycles	1.5 Million cycles	0.006 Million cycles	N/A*	N/A*	N/A*
12Nm	Tested 0.504 Million cycles	0.78 Million cycles	N/A*	N/A*	N/A*	N/A*
15Nm	0.08 Million cycles	0.012 Million cycles	N/A*	N/A*	N/A*	N/A*

*When gear tested for less than 1 million cycles no further test were done.

4.2 Comparison of 3D Printed Nylon 618 Gears to Injection Moulded Nylon 66 Gears

The wear in a gear is defined as the amount of material lost from gear tooth contact surface during gear operation. As detailed previously, the wear can be divided into three distinct phases, a "running-in" period, a linear wear period and a final rapid wear period. In the low torque stage, there was only a small amount of wear observed with minimal wear debris generated during both the running-in and linear wear stages. In the final rapid wear period, the wear rate increased dramatically and subsequently the appearance of debris was accompanied by a marked increase in operational noise. After gross wear (nearly 40% of tooth thickness), the gears failed in thermal bending and the teeth jumped out from meshing position. For loads greater than 12 Nm there was no run-in period observed with gears going straight into a linear wear period. Large amounts of

wear debris were recorded at the outset of gear operation at loads in excess of 12 Nm. The results obtained can be compared to literature results of injection moulded Nylon 66 gears, where under 5 and 7 Nm loads, the gears were operational for in excess of 1.2 million cycles, however, wear increased from 0.2 mm to 0.5 with the same wear rate. Under 10 Nm load, the test duration of injection moulded gears was decreased to 0.9 million cycles. When the load applied was increased to 15 Nm, the gear survived up to 0.08 million cycles (35). Hence, when compared to literature for injection moulded nylon gears, Nylon 618 3D printed gears provide better performance when load is applied below 12 Nm. Figure 24 shows the results of wear test carried out on a pair of printed nylon 618 gears.

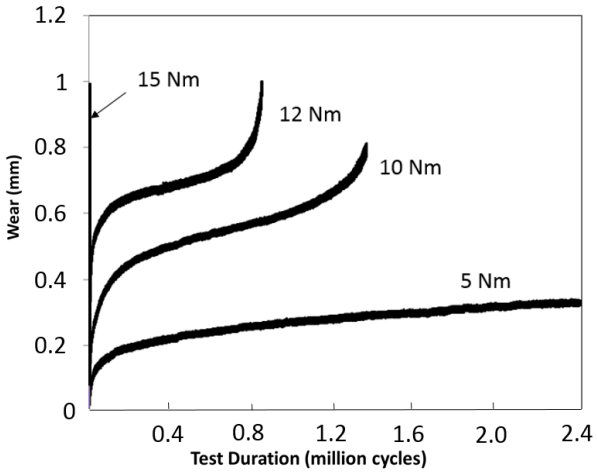

Figure 24. Result of Nylon 618 wear tests.

4.3 Wear rate analysis.

In order to ascertain the wear rate of 3D printed gears, a step load test was carried out. Nylon 618 gears were operated at 1000 rpm from 5 Nm and step load was increased by 1 Nm for each step until the gear failure. Figure 25 (a) shown the result of each step load that last 30 minutes. Each test was performed under same operational speed (1000rpm) increased by 1 Nm until gear was failed.

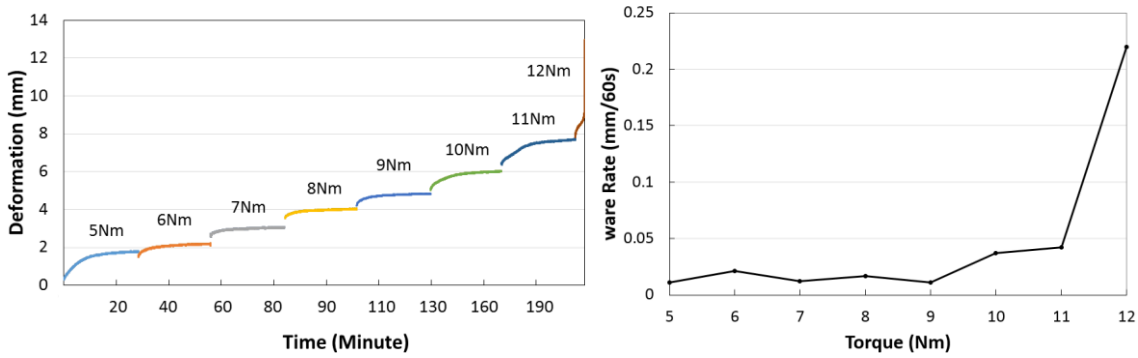

Figure 25.(a) Step load test of Nylon 618 (b) Wear rate against load for nylon 618 gears.

The nylon 618 test results in figure 25 (a) can be used to calculate wear rate under different loads shown as figure 25 (b), where the wear rate represents the material loss against torque per minute. According to the Friedrich et al. (151), the wear volume V_w is:

$$V_w = kFs \tag{14}$$

Where k is the specific wear rate, F the normal force, and s the sliding distance. If this equation is revised for tooth profiles, the specific wear rate for gear can be expressed as:

$$Qbd = k\frac{T}{r}d \times n \tag{15}$$

Rearrange equation:

$$k = \frac{Qbr}{Tn} \quad (16)$$

Where Q represents wear depth, b represents tooth face width, d is tooth depth, r is gear pitch circle radius and n are the number of cycles corresponding to the wear Q. Associated with the test of Nylon 618, at 5 Nm the wear rate was around 0.0113mm per 1 minute, and hence after calculating each step load test, the wear rate against torque was plotted as figure 25 (b).

As figure 25 (b) shows, the wear rate from 5 Nm to 9 Nm was very low. Each step load test was carried out for 30 minutes, hence, the operation time of each step load was not considered in this test. For loading above 9 Nm, the wear rate increased dramatically, believed to be mainly due to two factors: gear tooth bending force reaching the limitation of material yield stress, and gear failure due to thermal softening. When the gear surface temperature exceeds the material melting point, including ambient, bulk and flash temperatures, the wear rate will increase sharply. In order to fully characterise the wear behaviour of the 3D printed gears they were examined using microscopy.

4.4 Scanning Electron Microscopy (SEM) Analysis.

Injection moulded gears have previously been examined for signs of wear using SEM. In acetal and Nylon 6 gears, the material has been observed to be torn away at both sides of the pitch line. (152), (153)]Notably however, in the 3D printed gears tested here, there appears to be more material torn away at the addendum of the tooth flank. This contrast to literature behaviour may be due to higher tensile strength of Nylon 66 compared to Nylon 618 in the 3D printed gear. The lower tensile strength in the resultant gears potentially causes increased bending deformation of teeth causing a change in meshing position.

Figure 26 shows the failed tooth surface of nylon 618 3D printed gear. It is evident under x100 magnification that there is significant wear and bending at the addendum of the tooth, with that region of the tooth surface appearing to be melted. Moreover, SEM revealed that there was no

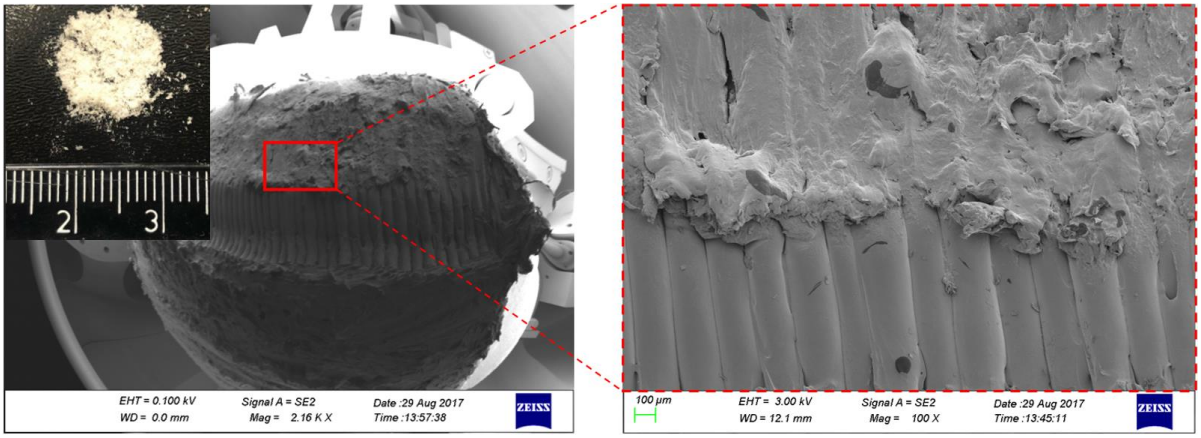

(a) (b)

Figure 26. (a) Fish eye SEM image over view of failed 618 tooth surface and debris. (b) Surface wear debris (×100))

material peeled off from the tooth (as might be expected with a 3D printed gear), showing there was strong bonding between each layer deposited during the 3D printing process. From visual inspection, the color of the printed material on the contact surface changed from white to yellow and the pitch line on the tooth face remained parallel to the addendum.

In order to draw a comparison between the Nylon 618 printed gears and one of the other printed gears, SEM was carried out on a Nylon 645 gear. As presented in figure 27, the SEM showed significant wear and bending at addendum of the tooth and the addendum part of the tooth surface appears to be melted. Moreover, the SEM also showed that material had peeled off from the tooth (Fig 28 (b)), which shows there was relatively weak bonding between each layer during the 3D printing process. As with the Nylon 618, the colour of the material changed on the contact surface

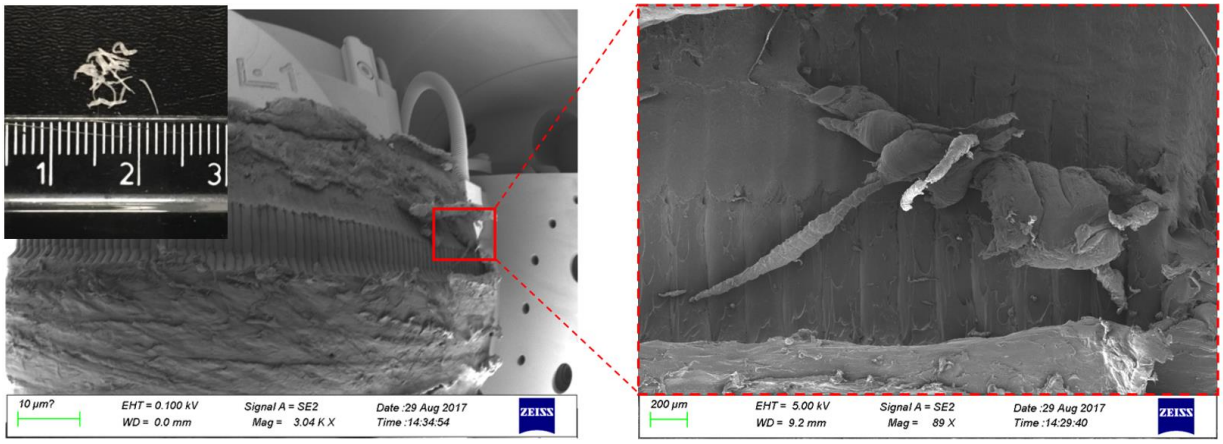

(a) (b)

Figure 27. (a) Fisheye SEM image over view of failed 618 tooth surface and debris. (b) Surface wear debris (×100))

from white to yellow and the pitch line on the tooth face did not remain parallel to the addendum cycle (Fig 27 (a)).

The results show dramatically different wear behaviour compared to injection molded gears. Examination of the tooth flank below the pitch line of the driver showed evidence of the material being torn away as the teeth roll against the direction of sliding and the tooth surface showed

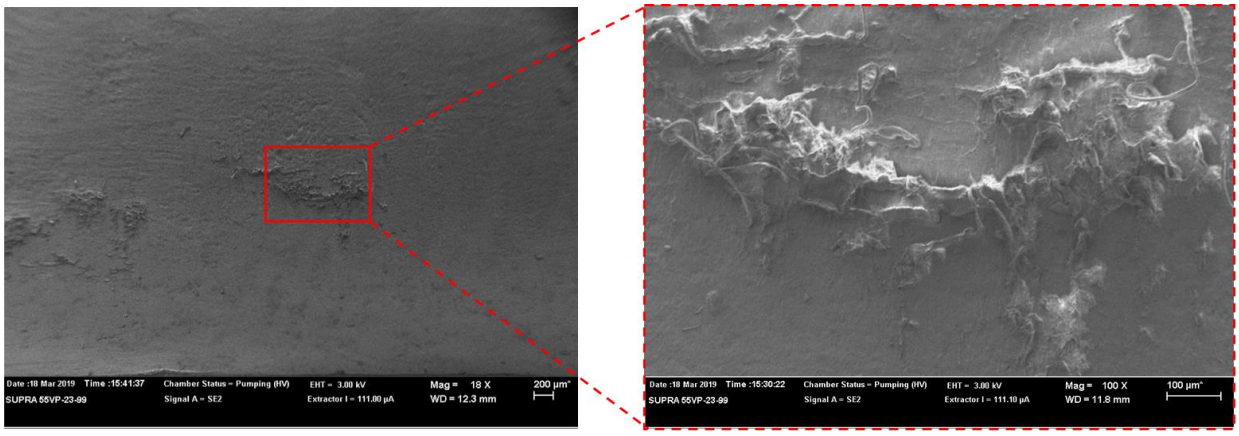

(a) (b)

Figure 28. (a) Nylon 66 injection mould gear (x 18). (b) Gear surface wear debris of Nylon 66 injection mould gear (×100)

relatively low surface roughness with no material peeled off from tooth surface (42), (58).

Moreover, as shown in figure 28, there is evidence of the onset of melting on the gear tooth surface, with the gear tooth shown relatively smoother compare with 3D printed gear. Several studies have mentioned that during FDM process, changes in temperature of the layer-by-layer polymer FDM process causes dramatically different cohesion strength of the layers and, the strength of the part. Greater differences in temperature during printing will weaken the bonding between each layers hence, this is one of the reasons causing different wear behaviour of 3D printed gear (60).

Polymer sintering effects affecting bond formation between layers, as shown in figure 29 [(60), (61)]. Parameter y represents the ratio of half the width of sintered bond, and d relates to filament radius. Hence y/d represents the bond formation of filaments and temperature difference in each layer could significantly affect the sintering process during FDM process.

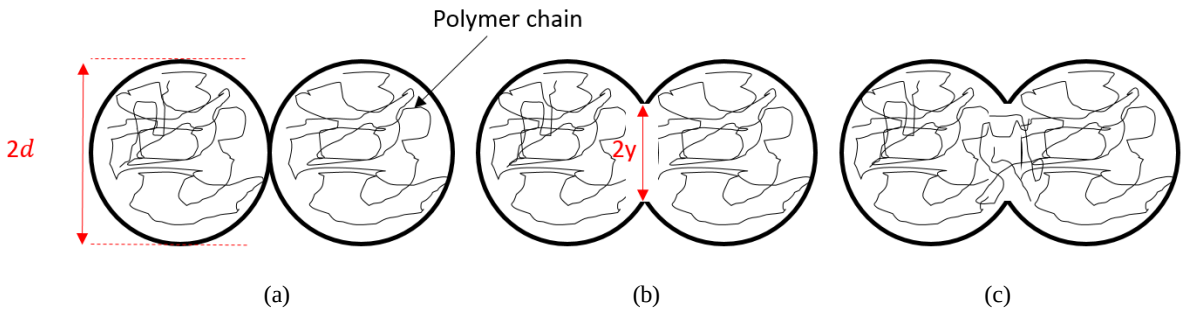

Figure 29. Process of polymer sintering between layers. (a) Represent filament instantaneously after deposition (b) Represent the neck growth, and (c) Represent sintering effect due to the movement of polymer chains.

This view of inter-layer bonding in 3D printed part (as shown in figure 29) could go some way to explain the difference formation in wear surface between Nylon 618 and Nylon 645, because nylon 618 has better polymer sintering behaviour compared with nylon 645 when printed using the manufacturers recommended parameters.

4.5 Differential Scanning Calorimetry (DSC) analysis.

In order to understand the thermal behaviour of the materials being used for 3D printing and assess if the thermal behaviour of 3D printed filament changed after printing, DSC was performed. DSC tests were carried out at three different stages, the first test was carried out before printing, the second test carried out after the nylon filaments were 3D printed and the third test carried out after the nylon gear step load test. It was found that the crystallinity of the filament before printing was slightly lower compared with the material after printing and material from gear tooth surface after testing. For example, the crystallinity of the Nylon 618 filament before printing was 43% and after printing was measured at 48%. Nylon 645 exhibited similar behaviour. Materials from a gear tooth surface after testing showed a crystallinity of 47.4%. DSC test results of glass transition temperatures and melting temperature showed that they remained relatively stable across the different stages with high repeatability of heating and cooling after being printed. Due to relatively poor performance in wear tests, alloy 910 and Markforged Nylon were not included in the DSC test. Nylon 66 (as used in the literature study of injection moulded gears) was included in the tests as a comparison material.

Tests were performed with two cooling cycles and two heating cycles to analyse the repeatability of each heating and cooling cycle. The temperature range of the test was set at -150 °C to 320 °C, with a heating rate of 10.00 K/min. An initial test was carried out with a maximum temperature of 420°C, however the materials decomposed after first heating cycle, and hence the heating temperature was limited to 320°C. As figure 30 shows the DSC tests of the different materials. Crystallinity was calculated using fitted equation with standard method based on a constant standard ΔH=196 J/g (154).

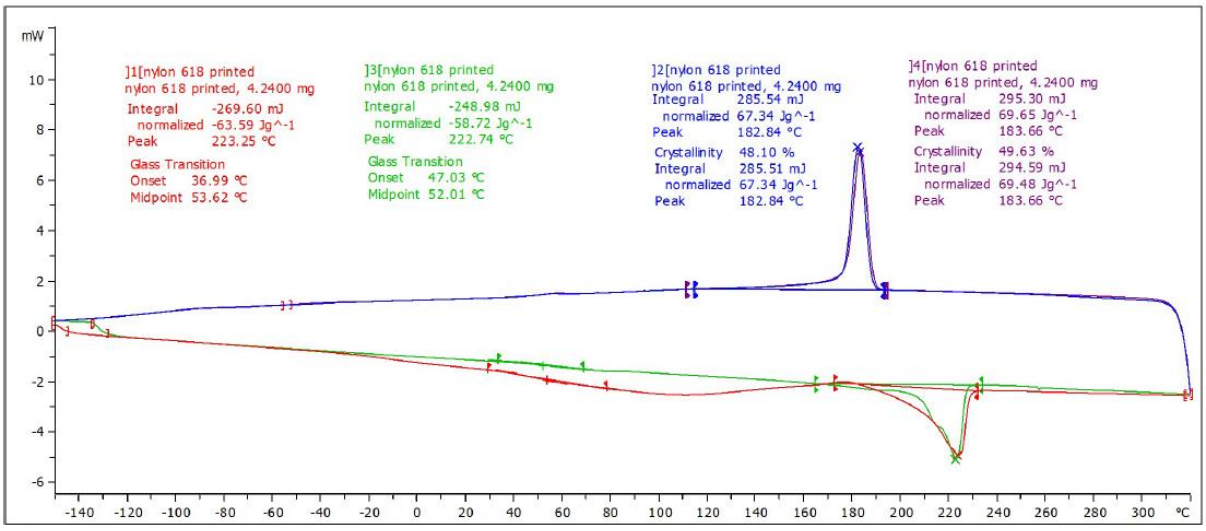

Figure 30. DSC test result of Nylon 618 filament after printed.

As figure 30 shown, the glass transition temperature of Nylon 66, Nylon 618, Onyx and Nylon 645, were measured as 54℃, 48℃, 47℃ and 43.5℃ respectively. The glass transition temperature of Nylon 618 was the same as the manufacturer's quoted value of 48℃. However, the test result of Nylon 645 was around 16% different to the value provided by manufacturer. The measured melting temperatures were similar compared with the data provided.

However, pure Nylon 66 had a higher melting temperature than the manufacturer quoted value. The crystallinities of Nylon 66, Nylon 618, Onyx and Nylon 645 were 56.51%, 48%, 23.5%, and 31% respectively. Normalised energy consumption showed the energy consumed during the heating and cooling cycling.

Based on the result of DSC test, it is believed that in the dynamic contact scenario found in polymer gears, thermal behaviour of polymer affects the wear rate and hence the performance of the polymer gear. From the test rig result, Nylon 618 filament had higher wear resistance compared with injection moulded gears at low applied torque. This may due to the unique process of the

FDM, with the gear tooth extrusions following the path of the gear tooth (155). Moreover, the 3D printing process could provide a benefit to molecular alignment in crystalline polymers such as Nylon (156). Shear stress distributed during the printing process can potentially cause the polymer to be aligned in the plane of the printed layers (157). Intramolecular bonding in 3D printing process often occurs as covalent bonding, which is stronger than van der Waals forces. Hence the mechanical properties could increase with suitable intramolecular bonding, which could further help explain why 3D printed gears can perform better than injection moulded gears in certain operating scenarios (55).

Measured Material / Thermal spec	**Nylon 66**	**Nylon 618**	**Onyx**	**Nylon 645**
Glass transition temperature	54℃	48℃	47℃	43℃
Melting temperature	260℃	225℃	200℃	210℃
Crystallinity	56%	48%	23%	31%
Normalised energy consumption	84J/g	60J/g	34J/g	45J/g

Figure 31. DSC test results

4.6 Gear tooth surface temperature.

The thermal performance of the Nylon 618 gears and Onyx gears is shown in figure 32 (c) and 32 (d) respectively via different torque at a constant rotational speed of 1000 rpm. The initial reading from the camera is plotted in dotted light grey, and the dark solid line represents the 6th order polynomial trend line to simplify the temperature analysis. Thermal test was carried out by wear test which the torque applied to nylon618 with 5Nm, 7Nm, 10Nm and 12Nm. Torque applied for thermal test for Onyx with 5Nm, 7Nm and 10Nm.

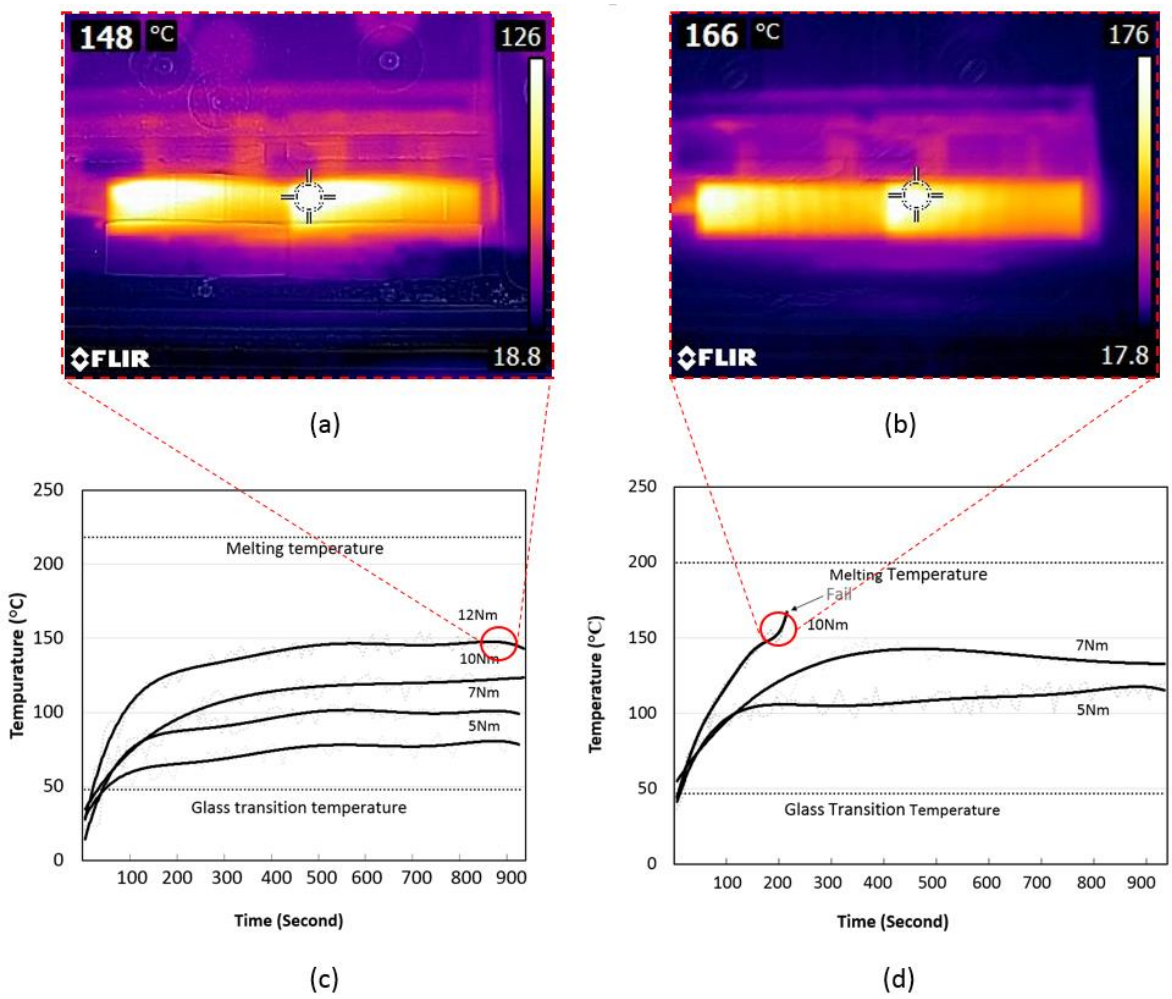

Figure 32. (a) Thermal image of Nylon 618 gear with 12Nm torque at 890 s. (b) Thermal image of Onyx gear with 10Nm torque at 200 s. (c) Thermal behaviour of Nylon 618 gears at 1000 rpm. (d) Thermal behaviour of Onyx gears at 1000 rpm

It was observed that for both materials, the surface temperature of the gears during operation was above the glass transition temperature. The analysis shows that there is a linear increase in temperature with increasing load in both materials. When the applied torque was 5 Nm, the surface temperature of the nylon 618 gears was steady around 80℃. There was a 20℃ increase in temperature when the torque was increased to 7 Nm, with a 35℃ increase in the surface temperature between 7 Nm and 10 Nm. Furthermore, there was around a 15℃ increase in temperature between 10 Nm and 12 Nm.

When 5 Nm torque was applied to Onyx 3D printed gears, the gear surface temperature stabilised around 110℃, increasing by 30℃ (to 140℃) when the torque was increased to 7 Nm from 110℃. However, when the applied torque was increased to 10 Nm, the gear failed after just over 180 seconds with a surface temperature of 170 ℃, 30 degrees below the melting temperature.

Comparing the thermal behaviour of Nylon 618 and Onyx, there was a 30℃ in difference (from 80℃ to 110℃) in surface temperature when both gears were subjected to the same torque of 5 Nm. There was around a 40℃ difference in surface temperature between Nylon 618 gears and Onyx gears at an applied torque of 7 Nm.

4.7. 3D printed gear failure mechanism.

Increasing the torque applied to 3D printed gears could lead to three main effects: an increase in contact stress, bending stress, and flash temperature of contact surface according to the equation (17) (18) below. (125):

$$\sigma = W^t K_0 K_v K_s \frac{1}{bm_t} \frac{K_H K_B}{Y_J} \dots\dots\dots\dots\dots\dots\dots\dots\dots\dots\dots\dots\dots\dots\dots\dots\dots (17)$$

σ_c : Gear contact stress.

W^t: Tangential transmitted load (N).

K_0 : Over load factor.

K_v : Dynamic factor.

K_s : Size factor.

b : Face width of the narrower member (mm).

K_h : Load-distribution factor.

K_B : Rim thickness factor.

Y_J : Geometry factor for bending strength.

m_t : Transverse metric module (mm)

Increasing the torque will lead to a greater value of W^t hence, bending stress acting on the gear tooth will accordingly increase. Gear tooth contact stress shown as equation below.

$$\sigma_c = C_p \sqrt{W^t K_0 K_v K_s \frac{K_h}{d_{w1} b} \frac{Z_r}{Z_1}} \dots\dots\dots\dots\dots\dots\dots\dots\dots\dots\dots\dots\dots\dots\dots\dots\dots (18)$$

Z_r : Elastic coefficient ($\sqrt{N/mm^2}$).

C_P : Surface condition factor.

d_{w1} : Pitch diameter of pinion. (mm).

Z_I : Geometry factor for pitting resistance.

It is extremely hard to measure the flash temperature of the gears, due to instantaneously contact of gear tooth, and flash temperature represent the highest temperature after gear tooth was sliding and contact, it is encloser when occurred. However, we could calculate the flash temperature via numerical calculations to predict flash temperature of the gears.

As shown in equation 19, increasing of the load applied to the gear will give rise to a raise in gear contact stress. Moreover, increasing the torque will cause a temperature accumulation in the gear body. An expression for the gear body temperature is shown as equation (19) below. (158)

$$\theta_b = \frac{3.927\mu T}{c\rho Zb(r_a^2 - r^2)} \dots\dots\dots\dots\dots\dots\dots\dots\dots\dots\dots\dots\dots\dots\dots\dots\dots\dots (19)$$

Where θ_b is the body temperature of gears, μ is the friction coefficient. T represents the transmitted torque, ρ is specific gravity, c refers to specific heat.r_a, r and b are outside radius, reference radius and tooth face width respectively. *Z* represents tooth number. From this equation it can be seen that torque and gear body temperature are positively correlated. The flash temperature can be expressed as in equation (20) below. (158)

$$\theta_f = 1.11\mu T \frac{(V_1^{0.5} - V_2^{0.5})}{b\sqrt{2k\rho ca}} \dots\dots\dots\dots\dots\dots\dots\dots\dots\dots\dots\dots\dots\dots\dots\dots\dots\dots (20)$$

θ_f is the flash temperature of the gear, a is half contact width, *V* represents sliding velocity of each gear, *T* represents the transmitted torque.

As figure 33 shows, there were three different types of failure that occurred in the wear tests of nylon 618 gears. When low torque was applied, the gears could sustain dramatically longer life

cycles compared with higher torque being applied. According to figure 33 (c), the gears failed due to material loss from the pitch line of the gear tooth when 10 Nm of torque was applied. Once wear from the gear tooth reached a certain depth, size factor K_s could dramatically increase lead bending stress in equation 18 excised the limitation of the gear tooth causing gear failure. When 12 Nm torque were applied, the life cycles were decreased from 1.5 million cycles to 0.78 million cycles with gear teeth failing due to root fracture (figure 33 b). With less life cycles, material loss was not the main cause for the gear tooth fail where in fact failure was due to lack of sintering effect between layers at the root of a gear tooth. Moreover, increasing load from 10 Nm to 12 Nm could rise the beading stress causing gear root fracture. With a higher toque of 15 Nm applied (figure 33 a), due to higher contact stress could lead to higher operational temperature (equation 19.20), teeth failed due to thermal bending.

For other types of nylon filaments, failure was mainly due to the lack of bonding between each layer of gear tooth, leading to dramatically higher rates of material loss from wear tests. Moreover, other nylon filaments are easier to heat up according to DSC tests, and hence operational temperature easily reached the melting temperature of the material. Those combined effects caused the rest of the nylon filaments to exhibit a much-reduced lifetime compared with Nylon 618 gears.

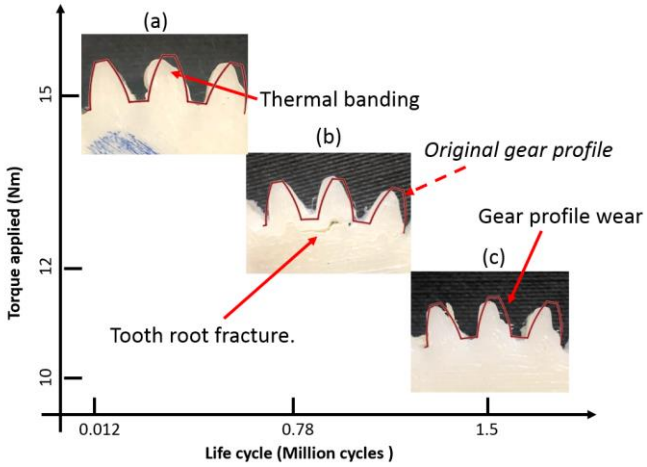

Figure 33. Failure mechanism of nylon 618 during wear test.

Chapter 5. Machine learning process applied for dynamic performance optimisation and prediction of 3D printed polymer spur gear.

5.1 ANN model fitting with original test data.

Figure 34 shown the performance of each model fitting with original 50 test data in section 3.3. Simulation was carried out with different ANN methods. In figure 34, Original test data was represented by red line, simulated data represented by black dote which provided by 3 different ANN models. It is clear shown that the converges of simulated data was improved with more complex model. Figure 34 (a) shows the linear fitting between ANN model and test data give pearson product-moment correlation coefficient of 0.85326 and R- square is 0.728 which shown high correlation related to the original test data (159),(160). However, performance optimisation could be achieved with more complexed simulation model. Hence, GA based ANN figure 34 (b) has been applied to the model which give closer agreement between the measured and predicted values of gear fatigue time. R2 increasing from 0.728 to 0.8 with GA applied, moreover, Pearson's r increased by nearly 5%. This could be an explanation to the fact that the proposed ANN-based predictive model accuracy in this case was increasing with GA optimization technique. Furthermore, initial target was to achieve the R-square greater than 0.9, hence, even the GA based ANN could provide a relatively satisfactory result. However, optimisations and prediction accuracy could be further increase by applied leave one cross validation. Figure 34(c) shown the model applied with both GA and using leave-one cross validation, Pearson's r and R2 shown dramatically increased from 0.83 to 0.97 and 0.728 to 0.956 respectively. Hence model with leave one cros validation applied will be the final model to carry on further analysis.

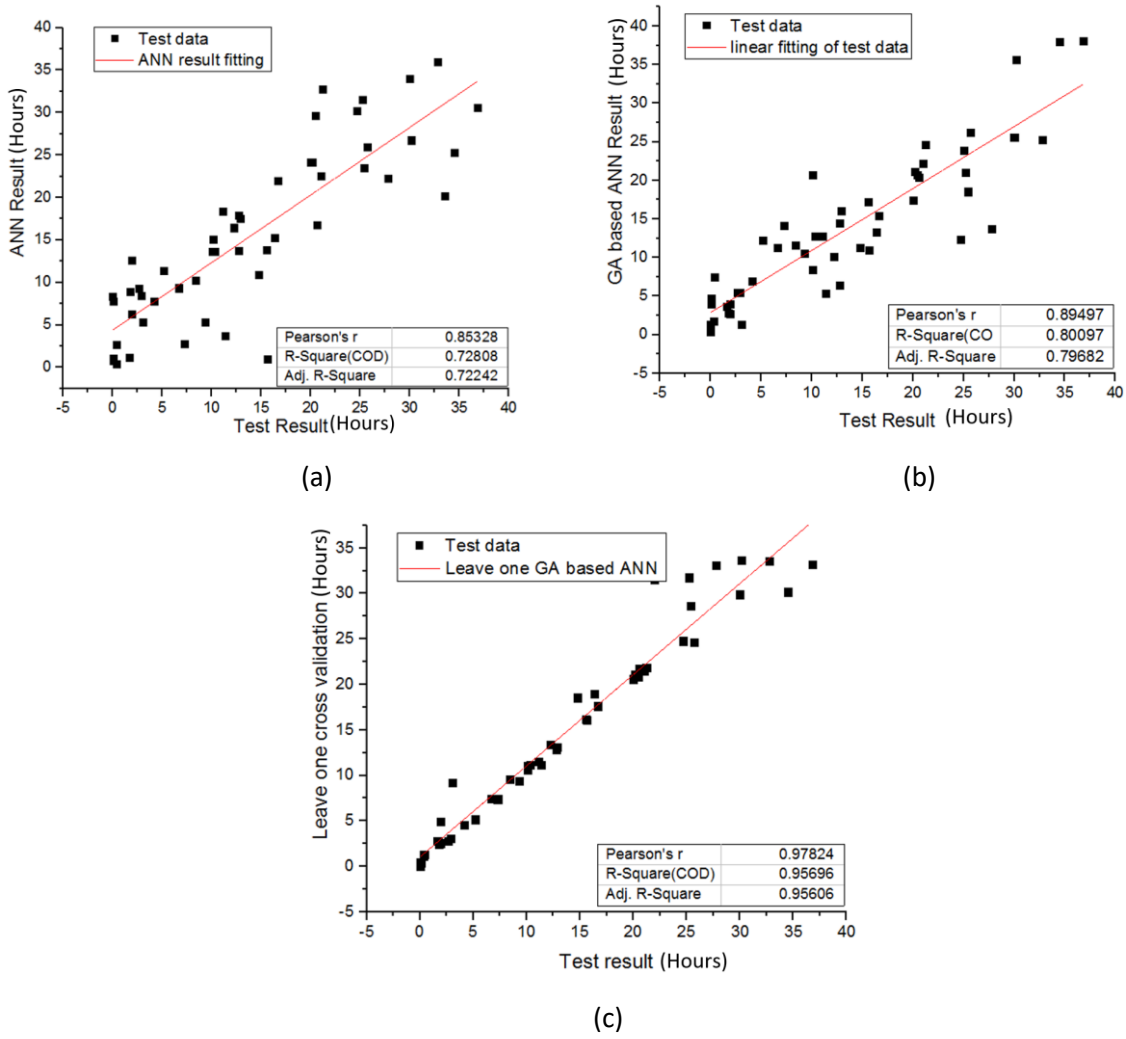

Figure 34. Performance result fitted with test data.

5.2 Genetic algorithm optimisation

Result of optimisations process performed by GA to optimise the ration between ω and δ shown as figure 35, hence, to contribute on the accuracy of the ANN performance. According to figure 36, solid plot represents the average error corresponded to the real test data, in the GA optimisation process, there are 200 iteration was selected due to decrease of the computational time and converge with optimised solution. Each iteration has 50 population involved, plot on solid line represent the average error corresponding to the test data and dotted line represent the best fitness

corresponded to test data performed by wear test rig. It is shown that average error was decreased from around 23% to 10%, moreover, best fitness was improved from 10% to less than 5% respectively. Hence, it can be proved that by applied GA could increase the efficiency and accuracy of the ANN regression model. The error of fitness was shown the difference between simulated data and real data, figure 35 shown a trend of error was decreased.

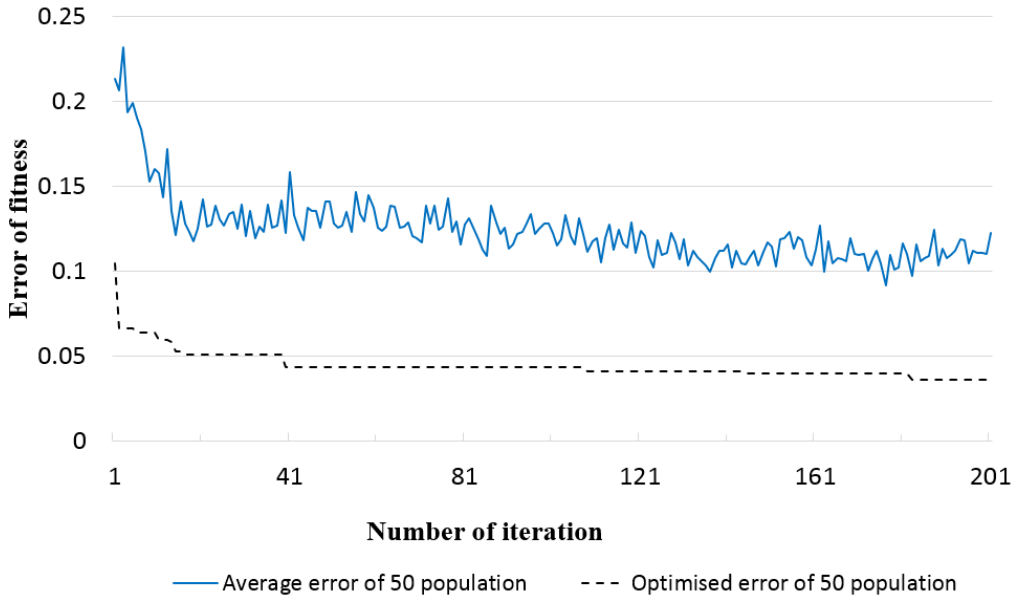

Figure 35. Optimisation process of GA on weight ratio of ANN

5.3. Sensitive analysis by Garson's algorithm.

The model reveals (figure 36) that printing temperature contributes to the performance of a printed gear by around 22% in terms of weighting. Printing speed has around a 23% influence in the performance. Bed temperature contributes a 8.6% influence to the final result, showing a reduced

importance compared with the rest parameters. Finally, by using Garson's algorithm it is possible to identify the most influential parameter regarding gear performance is infill percentage. Conceptually this result makes sense as it is possible that by increasing infill percentage, the rigidity of gear under loads is increased.

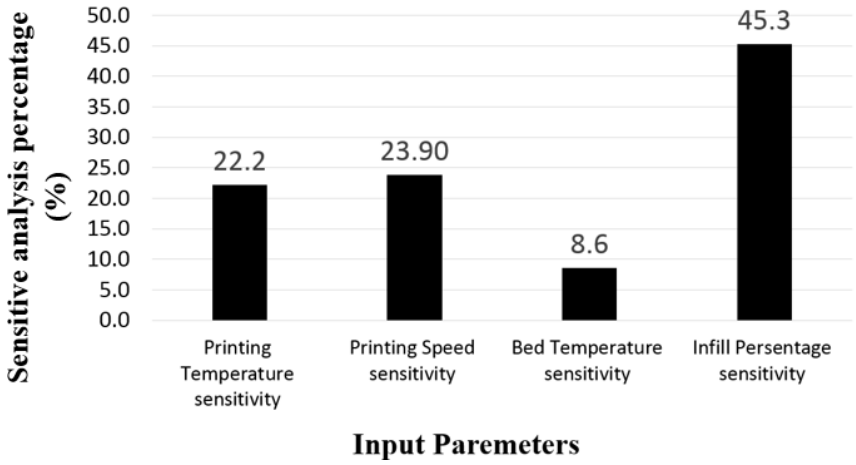

Figure 36. Sensitivity response contributes to result.

5.4. Optimisation setting analysis

In order to explore the power of the model in predicting optimal gear performance and outputting the 3D printer parameters required, a simulation was carried out. Figure 37 shows the simulation of 14256 combinations of different parameters. In this simulation, printing temperature is increased from 230°C to 275°C by 5°C （9 data）. Hence, there are 9 data points created for printing temperature instead of 50. Print speed was increased from 20mm/s to 75mm/s every 5 mm/s （10 data）. hence, there are 12 data points generated. Bed temperature is increased from 30°C to 70°C with 5°C each time, with 9 data points required for the analysis. Infill percentage was increased from 20% to 80%, with 12 data points. As mentioned earlier, there are more than 5

million combinations that could be used in generating test input data, however, errors in the 3D printing process and errors in the test rig could counter the tolerance of the setting, hence, a gap between parameters by factor of 5 could provide relatively accurate results. Simulation was carried out by leave one cross validation applied GA based ANN model. Simulation number 5732 showed 52.07 hours of potential gear performance with 3D printer settings of a printing temperature of 250°C, printing speed of 70mm/s, bed temperature of 25 °C and infill percentage of 80 %. Shown in Figure 37 below. According to figure 37, figure shown a periodic structure, it is meanly due to the repeat parameter for each simulation. Simulation with higher infill percentage, provide a longer operational time.

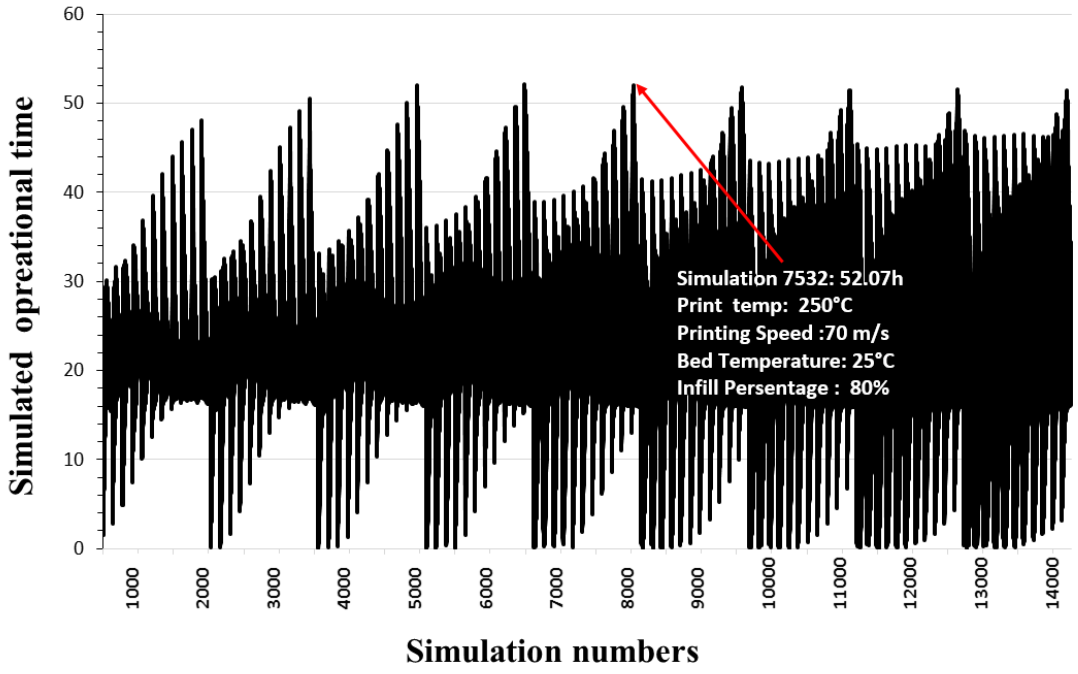

Figure 37. Sensitivity response contributes to result.

5.5 Simulation result validation test.

Validation of this model result was performed by producing a 3D printed gear using the same settings suggested by the ANN optimisation. 5 pair of gears were printed and tested on the wear test rig, with the results shown in figure 38 below. The results showed that the 5 tests yielded an average performance 51.46 hours, close to the ANN simulation value of 52.07 hours, hence optimisation simulation could be considered as a valid simulation.

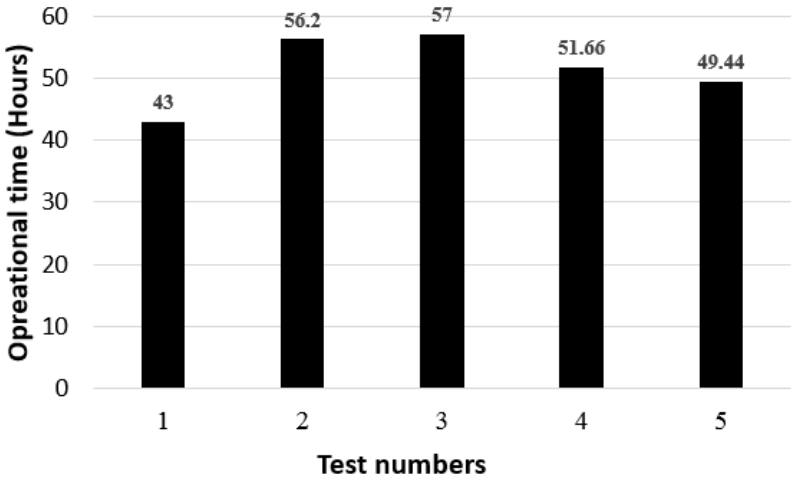

Figure 38. 5 test using optimisation setting for 3D printed gears.

5.6 Influence of different 3D printer settings on gears dynamic performance.

In previous chapter, a set of experimental data has been designed by sobol sequence, providing relatively higher tolerance and covering a much larger range of input data with minimal test data being required. Four 3D printing parameters was selected via specific requirement of polymer gears which require rigidity and light weight. A prediction model of 3D printed gears has been carried out with three models including an ANN model, a GA based ANN model and a leave one

cross validation applied GA based ANN model. Moreover, sensitive analysis for printing temperature, printing speed, bed temperature and infill percentage were 22.2%, 23.9%, 8.6% and 45.3% respectively. The results show that all models provide a relatively accurate prediction result and provide satisfactory fitting to the test data. A leave one cross validation applied model provides the strongest correlation with test results, with Pearson's r equal to 0.97 and R2 equal to 0.956 respectively. Moreover, by simulating an experiment, the printing parameters have been optimised to increase the performance of the 3D printed polymer gears. The results suggest an optimised setting of the 3D printer of printing temperature equal to 250°C, a printing speed of 70mm/s, a bed temperature of 25 °C and infill percentage of 80 %. The operational time of the resultant 3D printed polymer gear was increased more than 3 times compares with one produced using the default print settings. Sensitivity analysis performed by Garson's algorithm indicated that infill percentage has most influence on the performance of a 3D printed gear and bed temperature has the least influence on the test result.

5.7 Influence of each 3D printer parameter to gear performance.

ANN regression methods were performed within a black box. It is hard to see how each neuron interact with other neutrals. Hence, to investigate how each parameter could affect the performance of the 3D printed nylon gear was carried out in the following section. Moreover, sensitive analysis for each parameter has been carried out in the previous section, to further investigate how each parameter would affect the performance of the gear was carried in the following section.

50 data point were generated based on artificial neural network model. Figure below describes the correlation between bed temperature and operational time. Bed temperature varied from 20℃ to 70℃. In terms of investigating the response for each parameter, only one parameter will vary in

each simulation. Hence, when investigating bed temperature response, infill percentage was kept at 45%, printing temperature at 245℃, and printing speed was held at 45mm/s.

Due to the variation in bed temperature, gear performance time varied from 9.5 hours to 14 hours. Gear operational time was around 9.5 hours and when bed temperature around 20℃. Operational temperature started to increase until reach 50℃ the gear operational time was 14 hours. with further increasing the bed temperature, the gear operational time was decreased.

The fitted curve could be described as a Sine function with R-Square of 0.99972, which is highly correlated to the plot. Hence with ANN simulation this equation could describe the model with bed temperature and gear performance time, showing in figure 39.

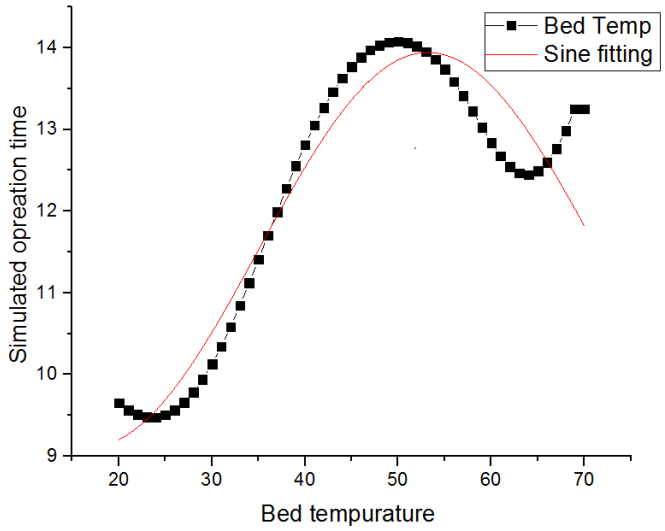

Model	Sine
Equation	y=y0+A*sin(pi*(x-xc)/w)
Plot	Bed temperature
y0	11.52731 ± 0.2197
Xc	34.99826 ± 1.43696
W	36.4007 ± 2.85844
A	2.41381 ± 0.1811
R-Square	0.99972

Figure 39. Numerical fitting via change of bed temperature.

As figure 40 showed, there were 50 test was simulated based on an ANN model to investigate the relationship between infill percentage and gear performance time. During infill percentage test, infill persentage was increased from 20% to 70% while bed tempurature remained at 45℃, printing temperature was set as 245℃, and printing speed at 45 mm/s respectively. Gear performance time was increasing from 5 hours to 30 hours. There was a dramatic increase in gear operational time after 50% of infill percentage, when infill percentage increased to 65%, gear performance time remained similar.

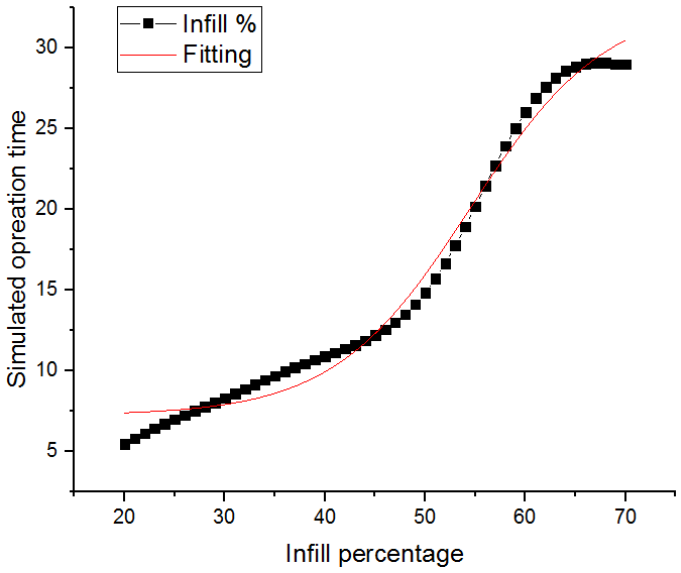

Model	Boltzmann
Equation	Time = A2 + (A1-A2)/(1 + exp((x-x0)/dx))
x	Infill percentage.
A1	7.22821 ± 0.31975
A2	32.7766 ± 1.0516
x0	54.44405 ± 0.69017
dx	6.7595 ± 0.54995
R-Square	0.98815

Figure 40 Numerical fitting via change of infill percentage.

To describe the response of infill percentage with a numerical equation, a Boltzmann equation was introduced with R-Square of 0.98815, which shows a high correlation of response.

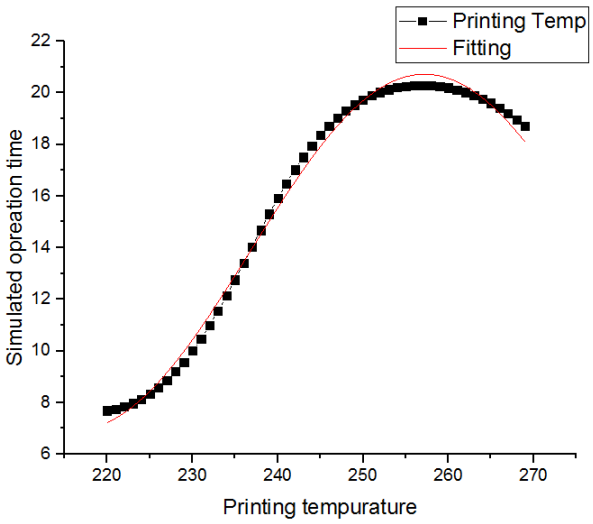

Model	Sine
Equation	y=y0+A*sin(pi*(x-xc)/w)
Plot	B
y0	13.82837 ± 0.16404
xc	-173.08288 ± 10.39637
w	40.9804 ± 1.00264
A	6.88894 ± 0.13573
R-Square(COD)	0.99509

Figure 41 Numerical fitting via change of printing temperature.

Figure 41 shown the response of the printing temperature, with the test of printing response. The temperature was increased from 220℃ to 270℃, bed temperature fixed at 45℃, infill percentage stay at 45% and printing temperature set as 245℃. Gear performance time varied between 6 hours and 24 hours, and the gear performance time peak appeared when printing temperature reached 255℃, and decreased after wards. There was a sharp increase after 230℃ sine equation was describing the response of the printing temperature with R-square of 0.99509. Hence, the numerical model could well fit well with response of the printing temperature.

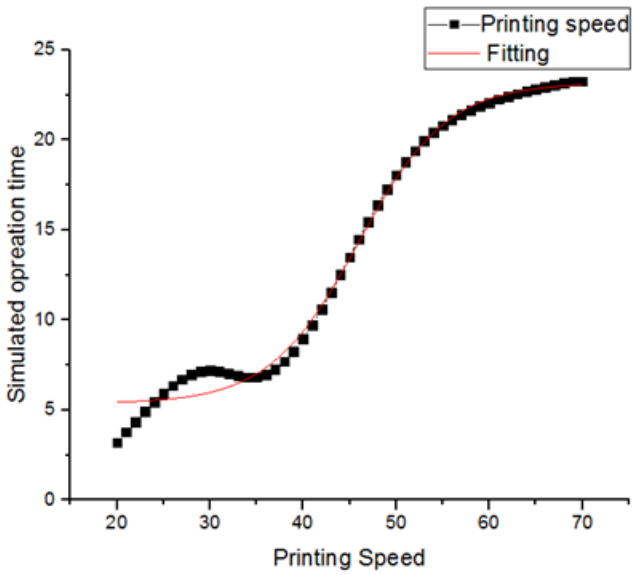

Model	Boltzmann
Equation	Time= A2 + (A1-A2)/(1 + exp((x-x0)/dx))
x	Printing Speed
A1	5.35548 ± 0.21755
A2	23.18063 ± 0.23782
x0	45.917 ± 0.28938
dx	4.78645 ± 0.27505
R-Square	0.99242

Figure 42. Numerical fitting via change of printing speed.

The response of printing speed shows a positive correlation with the gear performance time. Printing speed was increased from 20mm/s to 70mm/s, however, when printing reached 30mm/s gear operational time experienced a slight decrease. After 35mm/s gear operational time was sharply increased until speed reached 55mm/s. Gear performance time increased from 2.5 hours to 22.5 hours. A Boltzmann equation could describe the response of the printing speed. Shown in Figure. 42.

To discuss the response of the bed temperature, according to previous work, bed temperature was 8.6% in the sensitivity analysis, moreover, variation in bed temperature could change the operational time of gear by only 4.5 hours. This means, changing the bed temperature, could only have a limited effect on the result. This may due to the bed temperature only affecting the first few layers when printing. The thicker the printing object the less the bed temperature will contribute to the result. Unlike bed temperature, infill percentage has 45.3% of influence on the gear performance time in sensitivity analysis. Moreover, changing only the infill percentage could lead

to gear performance varying by around 25 hours. This is mainly due to the rigidity of the gear body. Increasing the infill percentage would be beneficial to the gear rigidity, hence, gears would occur less deformation during meshing and running. Therefore, gear teeth could operate in a desired position (117).

Printing speed and printing temperature could affect the bonding force between different layers, while, printing temperature and printing speed have similar sensitivity responses, of 22.2% and 23.9% respectively. By change printing temperature and printing speed separately, gear performance will be affected by 13.5 hours and 20 hours. A change in printing temperature could mainly affect the overall bonding force between each layer. Lowering the printing speed could increase the temperature difference of each layer, higher difference in temperature could cause higher thermal stress between each layer, hence, causing uneven stress across the gear tooth. Hence, a higher printing speed could provide better mechanical performance. However, in this case 70mm/s would be the appropriate speed due to no further increase in gear performance time after 70mm/s.

Chapter 6. Material properties analysis of 3D printed gears.

There were five different tests was carried out, including SAXS, WAXS, FTIR, and XRD test. Moreover, five tests were performed on three different 3D printing materials, including Nylon 68, Nylon 645 and Co Nylon. The aim of this chapter is to investigate the reasons that causing Nylon 66 based 3D printing filaments perform differently.

6.1 Analysis of different Nylon materials influence on failure mechanism.

The characteristic SAXS curves obtained from Nylon samples are adequately described by the equation proposed by Beaucage (161) which assumes the existence of a number of related structural levels by means of a unified equation offering a wide range of experimentally observed *q* values . The intensity would then obey the equation:

$$\boldsymbol{I(q) = Gexp(-q^2 \frac{R_G^2}{3}) + B(\frac{\{er\int(qR_g\sqrt{6})\}^3}{q})^p} \quad (21)$$

, where the first term accounts for the Guinier region (values of $q \leq 2\pi/R_g$), with two adjustable parameters: *G* (Guinier pre-factor) and R_g (radius of gyration). The second term describes the power law scattering behavior (for $q > 2\pi/R_g$), and the fitting of the experimental curve determines the pre-factor *B*, as well as the value of $\boldsymbol{p}$ (power-law exponent). A value of $\boldsymbol{p}$=4 for the high $\boldsymbol{q}$ limit in the case of sharp interfaces is predicted by Porod's law. Values of *P* larger than 4 are related with diffuse interfaces. If $4 > \boldsymbol{p} > 3$ the exponential law is characteristic of a fractally rough surface. The fractal dimension ds is calculated from the slope of the log–log intensity plots using the equation $d_s = 6 - \boldsymbol{p}$(162). The values obtained for d_s are between 2 and 3 and this parameter is associated with the topology of the surface. For d_s approaching 2, a well relevant smooth surface is assumed and ford$_s$ tending to 3 the surface will be more tightly crumpled(163).

In Fig. 43, the SXAS result consisted of intensity (Y-axis) and scattering vector (X-axis), and converted into volume distribution function (Y-axis) and volume distribution of radius (X-axis) under assumptions to be satisfied in reality, through a Titchmarsh transform according to:

$$\boldsymbol{D_v(R) \propto R \int_0^{\infty} [K - h^3 I(q)][2J_0(qR) + (qR - 3qR)J_1(qR)]dq} \qquad (22)$$

, where *D,(R)* is the volume distribution function of assumed spherical scattering heterogeneities whose radius is *R*, *K* = lim, ~ *q3Z(q)* and *J,* and *J1* are first-kind Bessel functions of order zero and one, respectively. Moreover, other representative parameters are available by directly analysing the experimental intensity curves(164). In Fig. 44, from the converted SAXS data, the mean radius of Nylon 618, Nylon 645 and Co Nylon can be determined as 24.2, 21.2 and 15.0 Å, which signify the decreasing tendency of lamellar spacing, domain size and corresponding periodicity from Nylon 618 to Co Nylon. The Full Width at Half Maximum (FWHM) are 7.4 (Nylon 618), 7.0 (Nylon 645) and 10.242 Å (Co Nylon), respectively. This suggests Nylon 645 has narrower distribution of its mean spacing, while Co Nylon was the widest one, based on the coherence

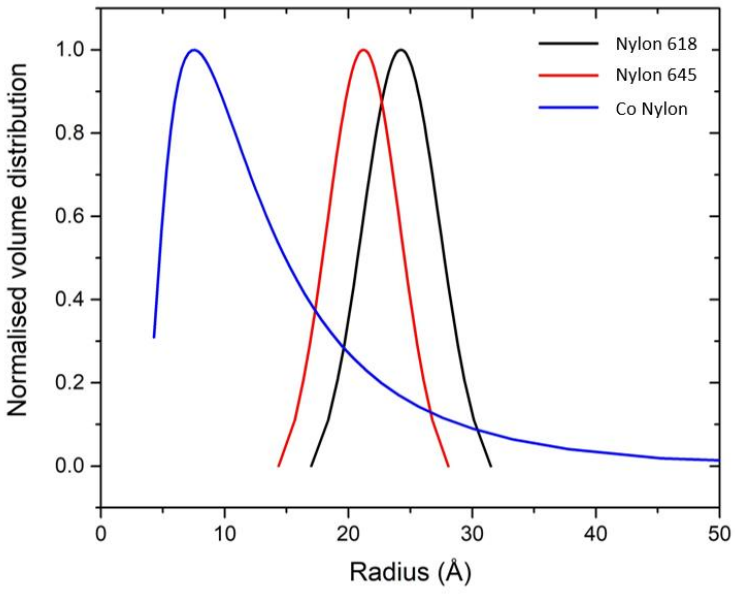

Figure 43. SXAS result of Nylon 618, Nylon 645 and Co nylon

length l_{coh} estimated by Sherrer equation(165). The shorter periodicity (smaller domain size) and more narrow distribution around the mean spacing will induce lower stress level, lower damage tolerance and lower fatigue resistance(165), which is identified in mechanical property test.

The WAXS result is shown in Fig.44, in which both Nylon 645 and Co Nylon just have one peak at $2\theta = \sim 21.0^{\circ}$ with the reflection of (100) and relevant d spacing of 0.416 nm in γ phase. However, the WAXS spectrum of Nylon 618 has three peaks located at ~20.0° ~21.0° and ~22.8°, respectively, among which the peak at ~ 21.0° is of (100) and 0.416 nm in γ phase as well, whereas the peaks at ~20.0° and ~22.8° are of (200) reflection, 0.445 nm d spacing and (002)/(220) reflection, 0371 nm d spacing, belonging to α-phase (166). The WAXS spectrum of Nylon 618 can be interpreted as a blend of α and γ phases. The fraction of the individual phase can be estimated by the ratio of the intensity of corresponding sharp peak in the software Highscore. Thence, the amount of γ phase can be estimated as 38.7% in the crystal phase of Nylon 618. Likewise, the crystalline index (CI) defined as the ratio of the total intensity of crystalline reflections to the total observed intensity (crystalline + amorphous) normalized to the maximum crystalline index observed for each individual sample(146), is equal to the crystallinity and can be estimated by HighScore. Thus, the crystallinity derived from WAXS are 49.3%, 35.6% and 24.1% for Nylon 618, Nylon 645 and Co

Nylon, respectively, which is consistent with the trend of lamellar spacing, amorphous domain size and periodicity illuminated by SAXS.

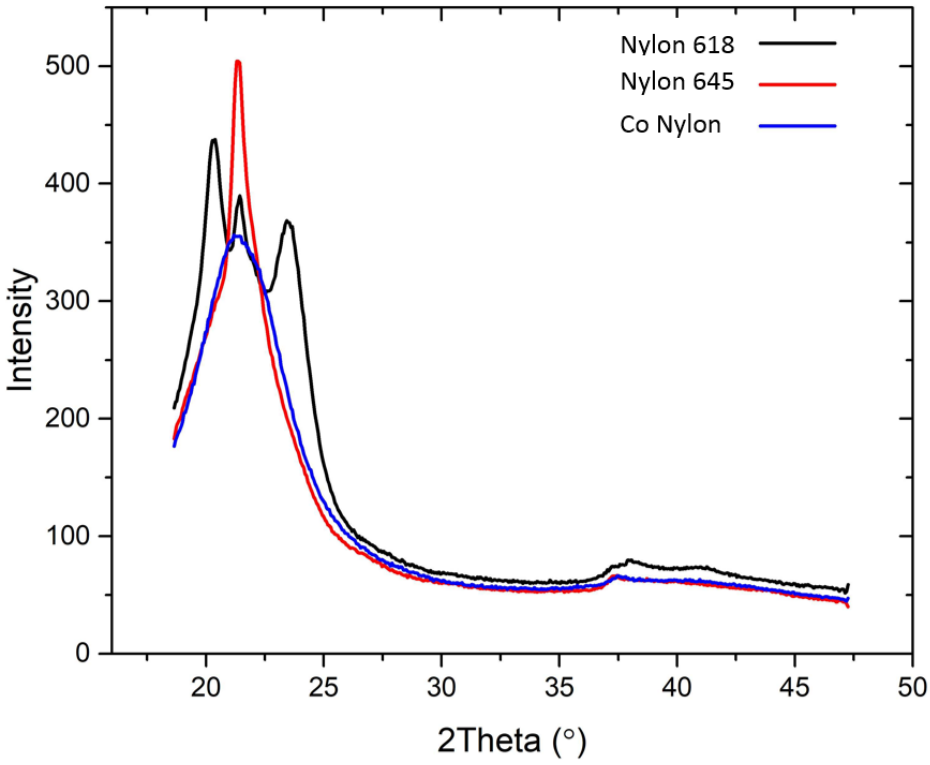

Figure 44. WXAS result of Nylon 618, Nylon 645 and Co nylon

6.2 Differential Scanning Calorimetry (DSC) Analysis result.

In order to understand the thermal behaviour of the materials being used for 3D printing and to assess whether the thermal behaviour of 3D printed filament changed after printing, differential scanning calorimetry (DSC) was performed. DSC tests were carried out at two different stages, the first was carried out before printing, the second carried out after the nylon filaments were 3D printed and the third carried out after the nylon gear step load test. It was found that the crystallinity of the filament before printing was slightly lower compared with the material after printing and material from gear tooth surface after testing, which was attributed to the annealing-like process

during 3D printing For example, the crystallinity of the Nylon 618 filament before printing was 43% (Figure 45) and after printing was measured at 48% (the heat of fusion data on equilibrium ΔH_f^O=196 J/g). Nylon 645 exhibited similar crystalline behaviour, the crystallinity of which changed from 27.9% to 28.3% before and after printing Materials from the gear tooth surface showed a crystallinity of 47.4% (figure 45). DSC test results of glass transition temperatures (T_g) and melting temperature (T_m) remained relatively stable across the different stages, which at 64.88℃ in the first cycle and 57.94℃ in the second cycle for T_g and 227.8℃ in the first cycle and 223.4℃ in the second cycle for T_m of Nylon 618. Likewise, Nylon 645 also can keep both the T_g (44.99℃ for first cycle and 44.89℃ for second cycle) and T_m (199.5℃ for first cycle and 200.8℃ for second cycle) stable before and after printing. Normally, a higher amorphous (but crystallisable) to high crystallization will lead to a more intense peak of crystallization temperature (T_{ch}), whereas a highly crystalline material might not exhibit(167). Herein, the peaks of T_{ch} of Nylon 645 in all cycles are more intense than those of Nylon 618, which shows the lower crystallinity of Nylon 645 than Nylon 618. The results showed that both materials had relatively stable thermal behaviour and high repeatability of heating and cooling after being printed. Due to relatively poor performance in wear tests, alloy 910 and Markforged Nylon were not included in the DSC test. Nylon 66 (as used in the literature study of injection moulded gears) was included in the tests as a comparison material. Shown in Figure 45 below.

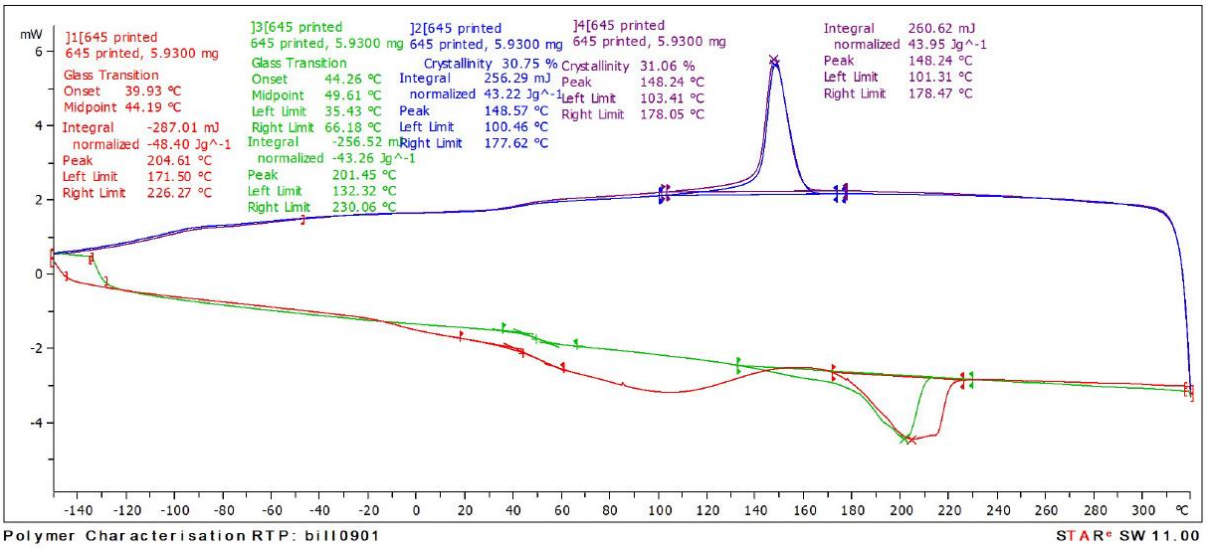

Figure 45. DSC test result for Nylon 645.

For polymer materials, composition and molecular structure can greatly affect crystallinity, and size of the crystallinity domain and therefore also the mechanical properties. For example, it was found that in semi-crystalline, branched poly(ethylene)-like materials yielded by polymerization of 1-octene, with different aluminium alkyls combined with various polymer microstructure, strongly affected the structure, thermal and mechanical polymer properties(125). In this research, to determine the difference of Nylon 618, Nylon 645 and Co Nylon regarding molecular structure, FTIR analysis was used with the result shown in Figure 46, while on the purpose of comparison, Nylon 66 was also investigated by FTIR. In Figure 46, the region from 3100 to 3500 cm^{-1} is sensitive to hydrogen bonding and is assigned to the hydrogen bonded NH stretch (amide A), thus the peaks at ~3250 cm^{-1} of all Nylon sample present N-H stretching while the peaks without that range at ~3020, ~2950, ~2840 cm^{-1} stand for CH stretches (C-H asymmetric stretching, CH_2 asymmetric stretching and CH_2 symmetric stretching)(168). The obvious peaks at ~1630 and ~1510 cm^{-1} are assigned to Amide I and Amide II band, respectively(168). The transmittance of

peaks concerning N-H stretching arising out of amorphous fraction, decrease from Nylon 66, Co-Nylon, Nylon 645 to Nylon 618 can predict the trend of their crystallinity. Meanwhile, the peaks set in the range from 900 to 400 cm^{-1} for N-H wagging, CH_2 rocking, C-C deformation and O=C-N bending can forecast the fraction of γ phase in the corresponding crystalline phase(166). For Nylon 66, at that range, only the intense peak of N-H wagging can be detected, which reveals the majority of α phase in that sample. Moreover, XRF was used to characterize the difference of these Nylon samples on composition. The main ingredient in these three samples is Nylon 66, and the elements in the additives to Nylon 66 are basically similar. The evident difference is the percent of Cl, Ca and Fe, which may be another factor inducing the difference on crystallinity of Nylon samples and will be studied further in the future.

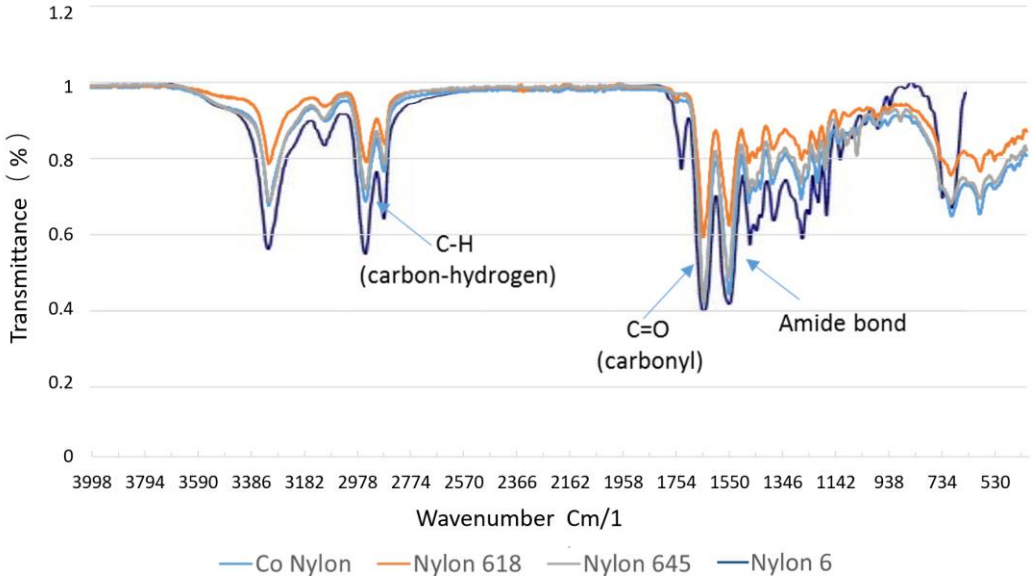

Figure 46. FTIR test result for Nylon 618, Nylon 645, and Co Nylon compare with Nylon 6.

Chapter. 7. Computational simulation of polymer spur gear.

7.1 Establishing 3D spur gear static simulation

In the previous chapters, the investigation of nylon gears has been well established, and stronger material such us PEEK could be investigated via similar method. However, due to the high cost of PEEK material, it is worthwhile to carry out a numerical simulation to have a basic understanding of PEEK gears before establishing experiments. 3D gear simulation has been built and accomplished, based on previous 2D gear simulation by MSc students at the University of Warwick. Considering the calculation cost, the rest of the gear body is replaced by coupling

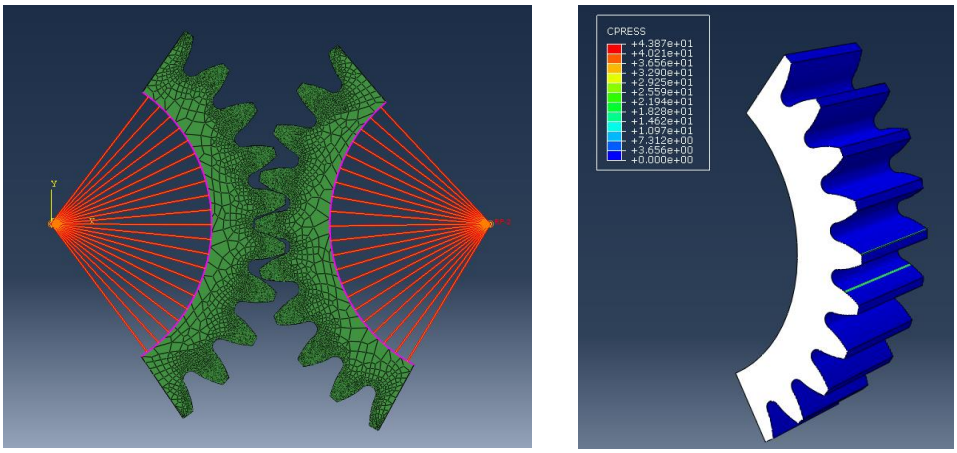

(a) (b)

Figure 47. (a) Coupling method in Abaqus and mesh generation, (b) 2D spur gear static contact simulation

methods, which assumes as rigid body, showing in figure. 47(a). 4Nm torque is applied on the gear based on PEEK material. The result shows the contact stress acting on the gear was around 43.87 MPa shown in figure 47 (b). It is impossible to see the contact stress while the two gears are in a meshing position, hence only one gear is displayed. Geometry is created based on Spur Gear 2M-30T with 15mm face width.

To validate this simulation, an AGMA contact equation was used (169):

$$\sigma = C_P\sqrt{W_t K_0 K_V K_S \frac{K_M C_F}{D_P F I}} \quad (22)$$

$E = young's\ modulus = 4000GPa$

$v = poisson's\ ratio = 0.38$

Where, C_P is the elastic coefficient, and C_P= $\sqrt{\frac{1}{\pi\left(\frac{1-v_1^2}{E_1}-\frac{1-v_2^2}{E_2}\right)}}$=27.27

W_t , Transmitted load=400Nmm

D_P, Pitch diametral of pinion=30mm

K_0, Overload factor=1

K_V, Dynamic factor=1

K_S, Size factor=1

K_M, Load-distribution factor=1.508

C_F, surface condition factor =1

F, Face width=15mm

I, Geometry factor=0.08

Therefore, σ can be calculated as follows.

$$\sigma = C_P\sqrt{W_t K_0 K_V K_S \frac{K_M C_F}{D_P F I}} = 27.27\sqrt{1.058 \times \frac{1}{30mm \times 15mm \times 0.08} \times \frac{400Nmm}{60mm}} = 45.57MPa \quad (23)$$

the difference between simulation result and calculation result was 3.8%. Still, according to Abdelrhman et al. (170), in his simulation, the static gear was against a tooth shaped rigid element. When compared with Hertz equation and AGMA equation, the errors are 12.71% and 1.66% respectively. Hence, the accuracy was similar. However, in the simulation produced by Abdelrhman et al. the Hertz effect was not fully represented due to the different mechanical properties between the rigid body and gear body, while the full cycle of the gear tooth contact was not accomplished.

7.2 Contact behaviour via geometry modification

By considering reducing the weight of the gears, it is resendable to find the part of gear carried less stress, which can be reduced. To further reduce the weight and cost of material while maintaining similar rigidity, shape optimisation methods were used. According to the figure 48,

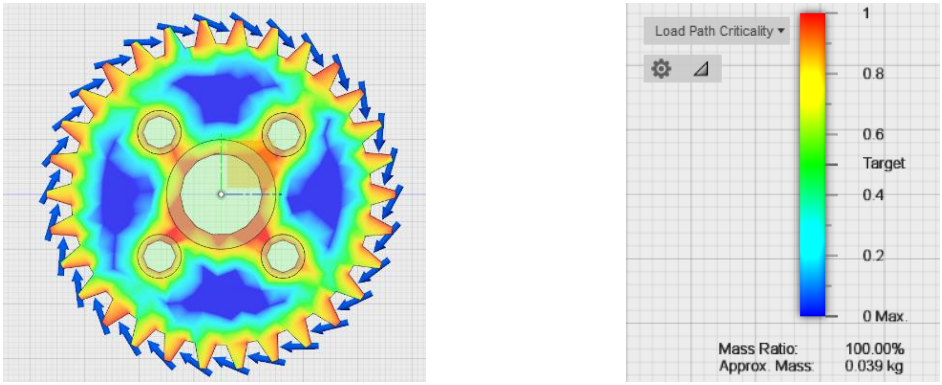

(a) (b)

Figure 48. (a) Load distribution within the polymer gear (b)load path criticality

PEEK was used in this shape optimisation. In terms of simulation gear loading criteria, the key hole was restricted in any direction. 4N load was distributed evenly on each gear tooth in order to represent the gear loading. According to the result, the blue part showed in figure 48（a）carried

less load, and the red shows the part carried more load. Hence, according to the figure 48(b) about 13% of material can be removed by further design.

7.3 Geometry modification by change in rim thickness.

Removing the material of gear rim could further reduce the weight and cost per gear. According to G.D.Bible (171) bending stresses in thin rims spur gear tooth fillets and root areas differ from the stresses in solid gears due to rim deformations. Rim thickness is a significant design parameter for these gears. A reduction in material while maintaining the mechanical performance which need several simulations. The simulation was based on the influence of increase or re duction in rim thickness in terms of stress changing on gear tooth. Shown in Figure 49 below.

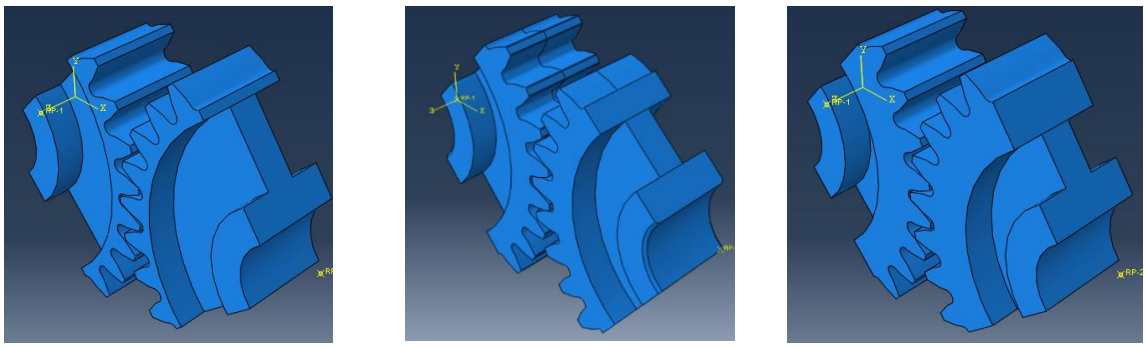

(a) (b) (c)

Figure 49. (a) Rim thickness 1.5m. (b) Rim thickness 4.5mm. (c) Rim thickness 6.5mm.

There are 6 iterations of the rim thickness: 1.5mm, 2.5mm, 3.5mm, 4.5mm, 5.5mm, and 6.5mm, as the figures 50 below show. This simulation was based on polycarbonate. As the result, the stress acts in accordance to different rim thickness.According to the result of the simulation, the increase of the rim thickness can raise the stress of the gear tooth. However, after rim thickness was extended than 5.5mm, the stress remains similar.

The result shows that the differences of the stress was determined by rim thickness. In addition, the simulation result indicates that a decrease in the rim thickness can increase the gear tooth rigidity. However, while rim thickness was greater than 5.5mm, the stress remains at 55.5Mpa.

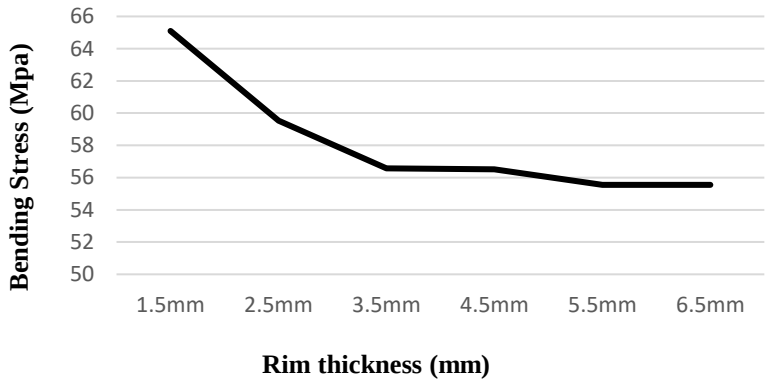

Figure 50. Simulation result in maximum stress against rim thickness.

Moreover, when rim thickness is more than 3.5 mm, it will provide similar rigidity of the gear tooth compare with 5.5 mm thickness. To reduce volume of the gear can also reduce the computational cost in simulation due to less elements being analysed if the meshing size and other simulation parameters remain the same.

7.4 Contact behaviours change regarding to different meshing position

Misalignment usually happened when gear was loaded causing bending force acting on gear shaft, hence, a misalignment occurred on gears. Four different types of misalignment have been simulated: pitch misalignment, radial misalignment, yaw misalignment and axial misalignment. In the FEM simulation, there are several degrees or distances regarding different misalignment. Furthermore, to understand the behaviour of polymer material compared with steel gear in terms of misalignment, four types of misalignment were simulated both in polycarbonate (as example to

demonstrate the behaviour of polymer gear)and steel. Due to the stiffness of the material, the steel gear misalignment simulation used 20Nm and PC gear simulation used 4Nm torque.

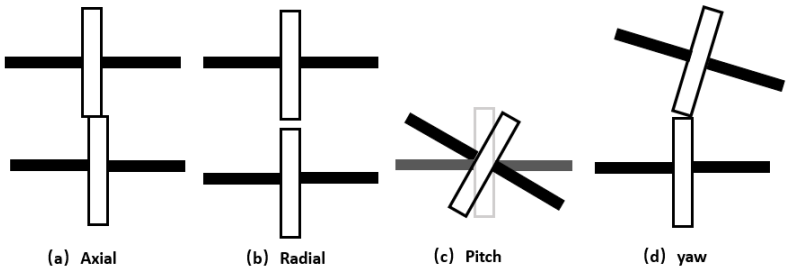

Figure 51. Four types of misalignment of spur gear pair.

7.4.1 Axial misalignment

In the Axial misalignment simulation, there are two gears were rotated along with z-axis at different distances: 0.5mm, 1mm, 1.5mm, and 2mm. Axial misalignment will remain the line contact with two gears. Figure. 52 shows the steel gear and polymer gear contact stress changes

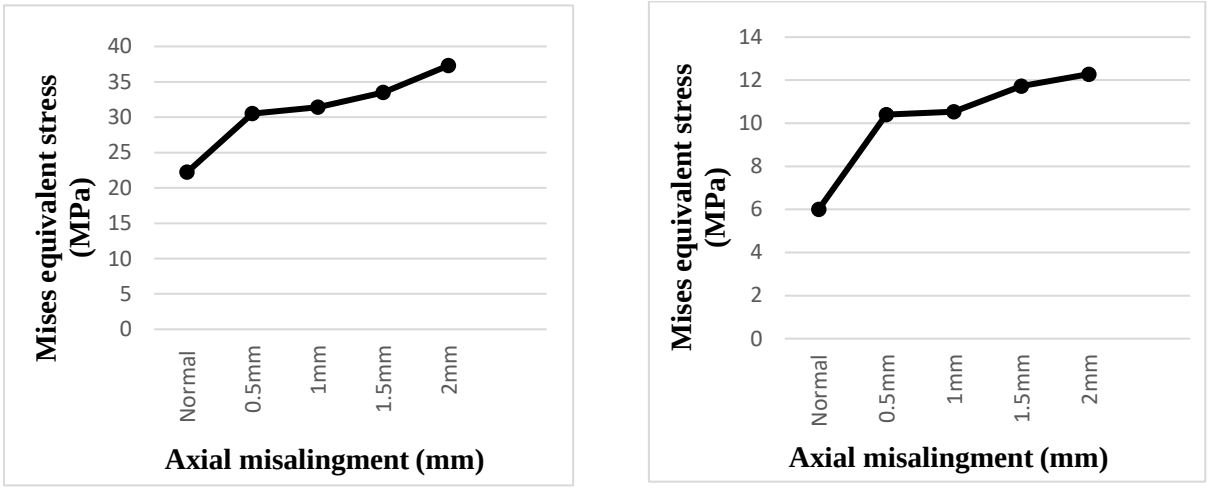

Figure 52. (a) Steel gear axial misalignment simulation with 20N load. (b) PC gear axial misalignment simulation with 4Nm torque.

under different rates of misalignment.

7.4.2 Radial misalignment

The ideal distance between gears centre is 60mm. Therefore, there was four central distances of the adjustments: 60.2mm, 60.4mm, 60.6mm, and 59.8 mm.

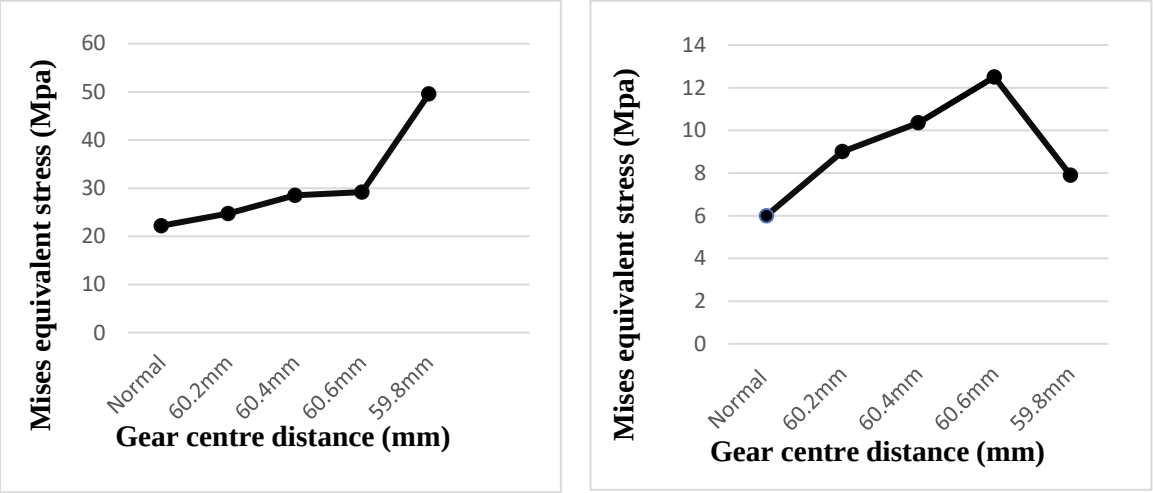

(a) (b)

Figure 53. (a) Steel gear axial misalignment simulation with 20Nm torque. (b) PC gear Radial misalignment simulation with 4Nm torque.

7.4.3 Yaw misalignment

Yaw misalignment is an angular misalignment. In these types of misalignment, line contact switch to point contact after the deformation of gear tooth, the point contact becomes the surface contact again. In the yaw misalignment, gear shaft occurs an angle along z-axis that starts from 0.5 degree to 2 degree and increased 0.25 degree in each iteration for PC gear. For steel the gear yaw simulation misalignment sets from 0.5 to 1 degree.

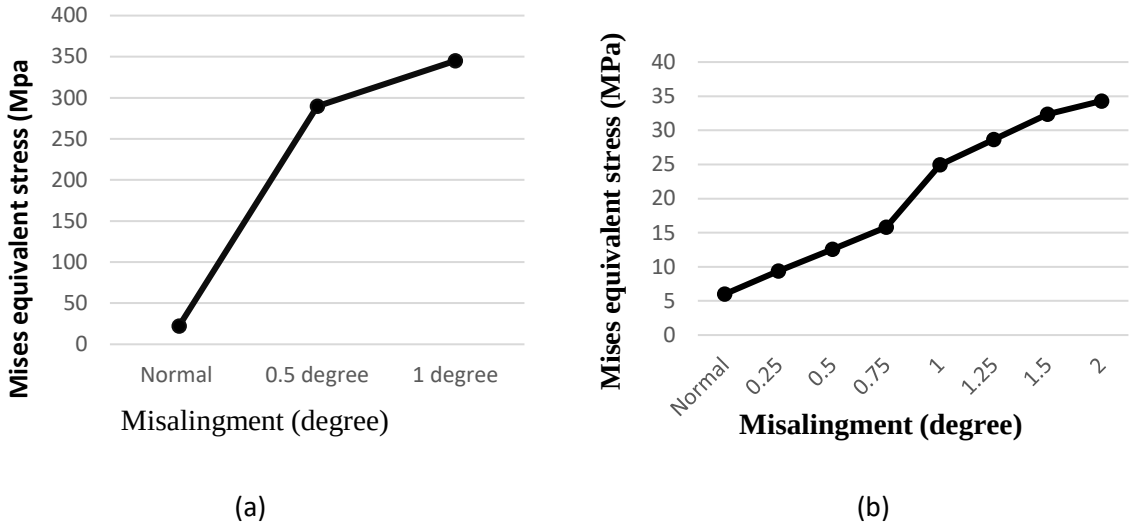

Figure 54. (a) Steel gear yaw misalignment simulation with 20Nm torque. (b) PC gear yaw misalignment simulation with 4N load.

7.4.4 Pitch misalignment

Pitch misalignment simulation performed in steel gear starts from 0.25 degree and ends up with 0.5 degree, and PC gear misalignment was from 0.25 degree to 1.25 degree with 0.25-degree increments.

According to the simulation Figure 55, pitch misalignment provides the essential influence to the gear meshing. Even small degree of rotation can dramatically change the position and shapes of the contact area and push towards the edge of the tooth flank. This simulation claims a similar result as Jones et al. (34).

Radial misalignment can change the involute contact and, therefore, increase the friction, and may increase the noise when operating. Considering the axial misalignment can reduce the contact area of the gear tooth and produce the moment between two gears, with the small amount of radial misalignment, the effects of the moment can be ignored. Yaw misalignment can be caused by the

bending of the gear shaft due to the load applied to the gear. To reducing yaw misalignment, it is plausible to apply an external shaft rotation. In addition, misalignment can appear in more than one form. For example, when applying the yaw misalignment, an introduction of a small amount of radial misalignment is always necessary in order to avoid overlay, shown in figure 55.

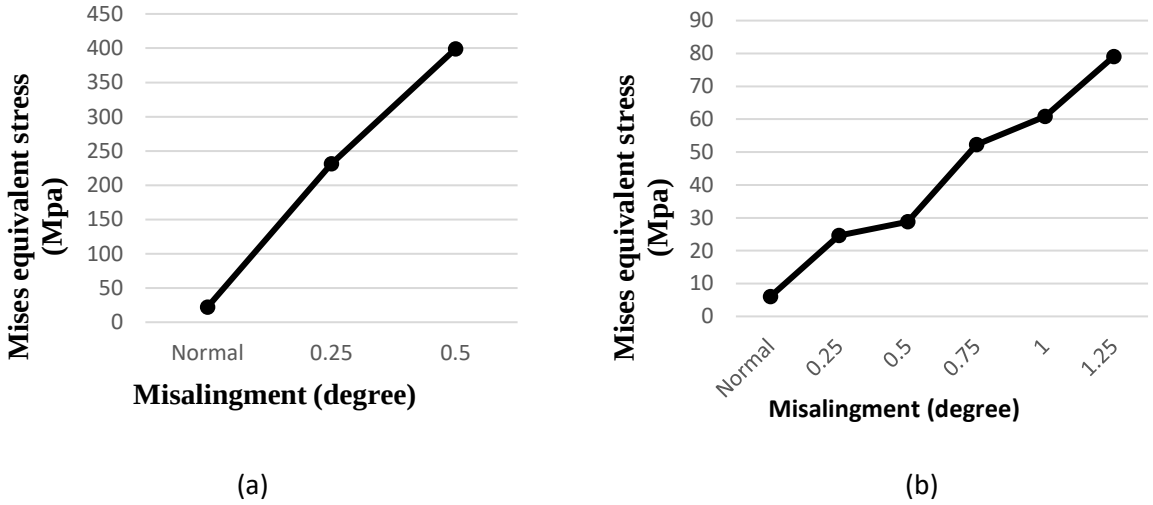

(a) (b)

Figure 55 (a) Steel gear pitch misalignment simulation with 20N load. (b) PC gear pitch misalignment simulation with 4N

7.5 Fibre reinforcement composite static simulation

To investigate the concept of fibre reinforcement to polymer gear, a rectangular cantilever was used to simplify the structure of gear tooth. The fibre reinforce simulation was based on cantilever beam bending by changing the orientation of the fibre filler within the matrices by three different positions: 30 degrees (Figure 56 (b)), 45 degrees (figure 56 (a)) and 60 degrees ((figure 57(b)).

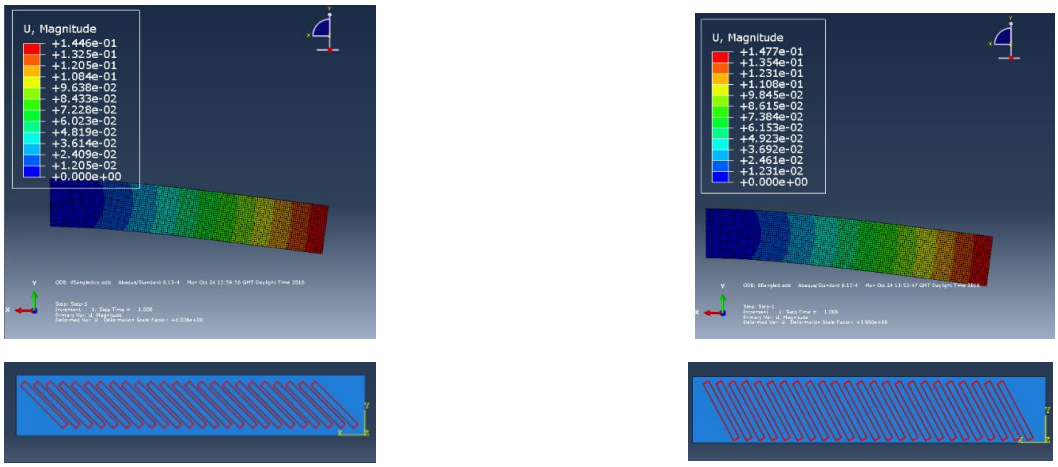

Figure 57. Reinforcement 45 degree fibre in PEEK with deflection of 0.145mm (a) Reinforcement 60 degree fibre in PEEK with deflection of 0.148mm (b)

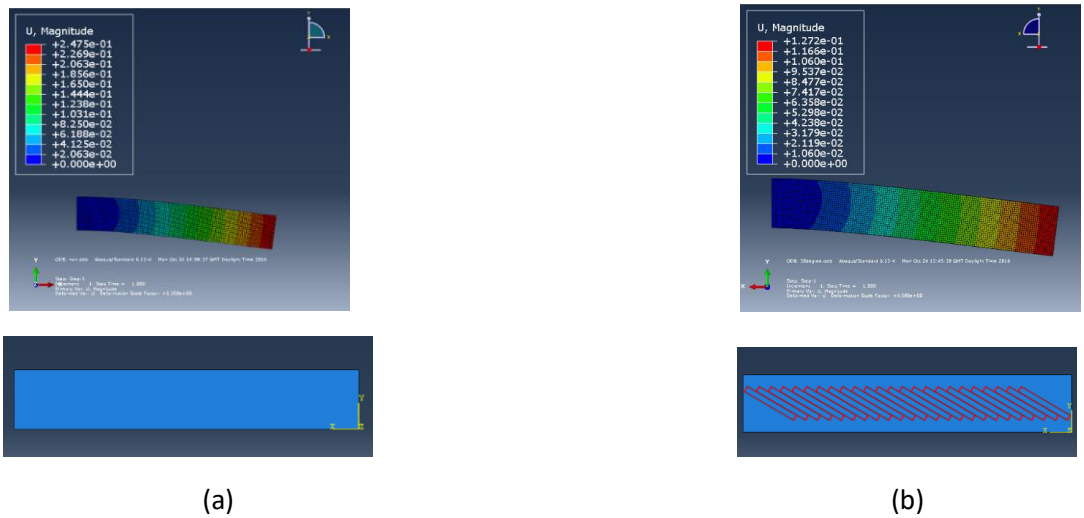

Figure 56.(a) Raw PEEK cantilever beam with deflection of 0.2475mm. (b) Reinforcement 30-degree fibre filler in PEEK with deflection of 0.127mm.

The size of the PEEK matrices is 5.8mm ×1mm×1mm, and that of the carbon fibre filler is 0.1mm diameter with 1mm length. The cantilever beam was fixed on one side and load of 0.5 N was aplied on the other side while the number of fibre fillers remained the same in each simulation.

According to the previous figure, less angle of fibre could reduce the deflection of cantilever beam. However, further simulation with horizontal and vertical fibre orientation was carried out. Simulation compared different combinations of carbon fibre in the cantilever at 0 degree and 90 degrees Figure 58 (a) (b).

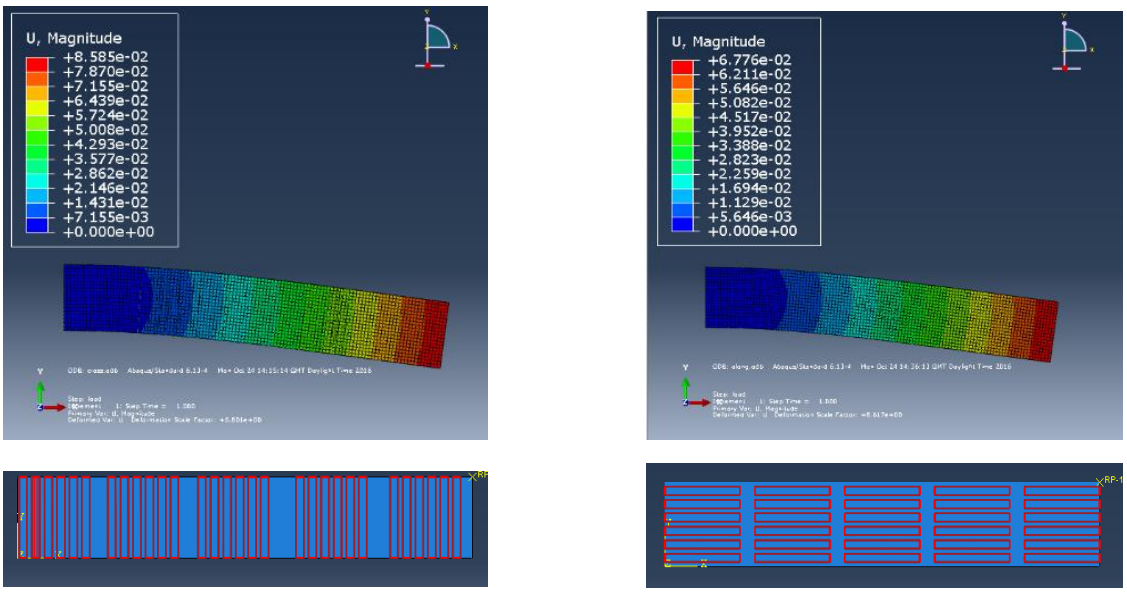

(a) (b)

Figure 58. (a) Reinforcement 90 degree fibre in PEEK with deflection of 0.085mm. (b) Reinforcement 90 degree fibre in PEEK with deflection of 0.067mm.

From the cantilever beam fibre filler reinforcement simulation, it is possible to assume that the alignment of carbon fibre perpendicular to the gear contact surface could provide a better result in terms of reinforcement performance. Therefore, the static loading simulation of carbon fibre reinforcement PEEK gear was carried out as the figure 59 below shows. There is 15Nm torque applied to the gear.

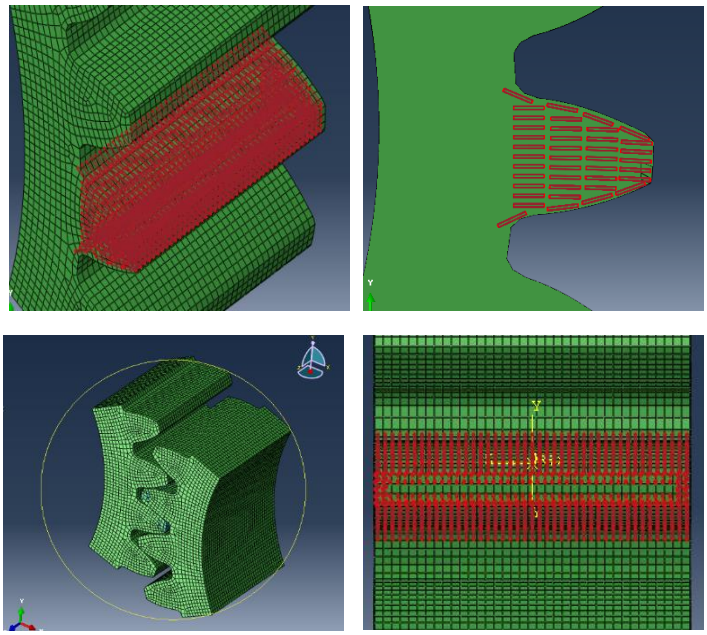

Figure 59. Carbon Fibre reinforcement of PEEK spur gear fibre orientation and gears contact position.

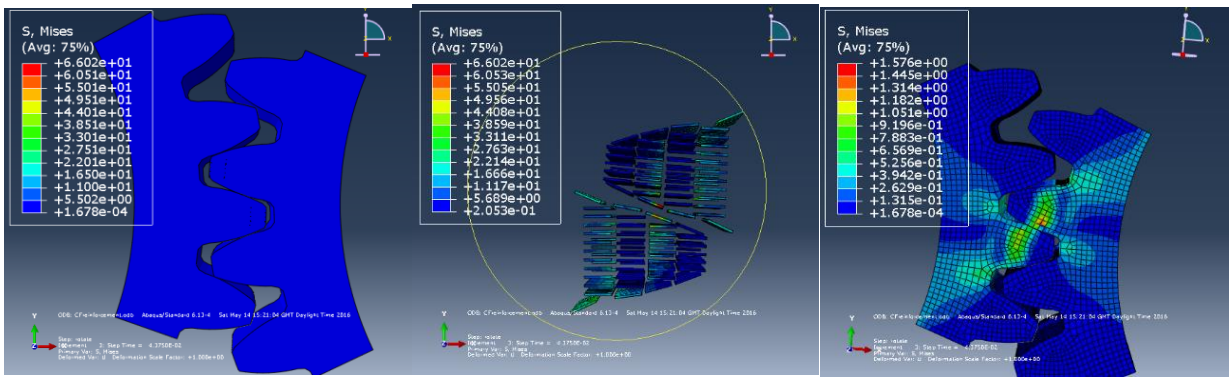

(a) (b) (c)

Figure 60. (a) Stress distribution on PEEK matrices and fibre filler. (b). Stress distribution on fibre filler. (C). Stress distribution on PEEK matrices

As shown in figure 59, the stress acting on the reinforcement gear was 66.02 MPa. By analysis the contact stress acting on peek and fibre separately could reflected the contribution of fibre in terms of reinforced. understand and the stress action on the PEEK matrices was below 5 MPa. Hence, as the figure 59 shown that most of the stress was applied to carbon fibre filler, hence the PEEK matrices was only carried 1.57MPa.

By analysis the simulation of cantilever beam simulation, the carbon fibre reinforcement improved the mechanical properties to reduce the deflection dramatically. According to Gupta It has been also claimed that low volume fraction of CNT results in a large increase in elastic modulus. Tibor et al (25) modelled the tribological performance of composite polymer with steel counterpart and analyed by real world experiment and FEM simulation. A steel sphere was slid across the carbon fibre reinforcement polymer, in three different orientation, moreover, best performance provided with the fibre orientation parallel to the sphere, which is similar to the cantilever beam simulation. In the cantilever beam simulation, the fibre filler orientation parallel to the cantilever beam could provide better performance (26).

When considering the carbon fibre reinforcement gear simulation, stress acting on the PEEK matrices was decreased by 40 times. However, this simulation was only aimed at understanding the distribution of stress acting on the filler, hence, the proportion of the carbon fibre was not considered.

7.6. Polymer spur gear thermal dynamic simulation

Dynamic and thermal effects simulation were successfully carried out by Abaqus Explicit. Simulation was carried out a pair of PEEK 450 spur gears was meshed with 1500 rpm with 4 Nm torque in 2 seconds. Due to complexity of the simulation, This 2 seconds simulation were take to month to complete. The initial material and ambient temperature were 20 degrees. Moreover, in this simulation, the thermal properties were considered, including conductivity, expansion, and specific heat. Due to the rotation of two me

shing gears, all gear tooth modelled, and the rest of the gear body using the coupling method to transform into the rigid body. The contact stress of the gear was shown in figure 61 below.

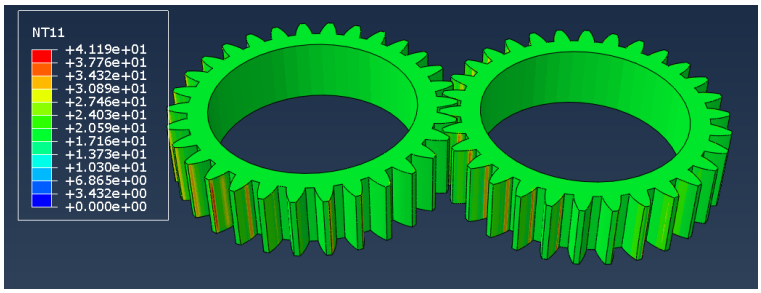

Figure 61. Flash temperature simulation. Master Gear (left) and Slave Gear (right) unit: °C

Figure 62 shows, the result of the dynamic simulation contact stress is 46.07 MPa, and the peak contact stress obtained at the edge between top land and addendum tooth face. Compare to the AGMA calculation result, the difference was only 0.9%. However, due to the dynamic affect, the contact stress was not constant. Still, due to the separation during the high-speed operation at some point, the gear was not in contact at all. Moreover, the stress was increasing at beginning of the rotation due to inertia.

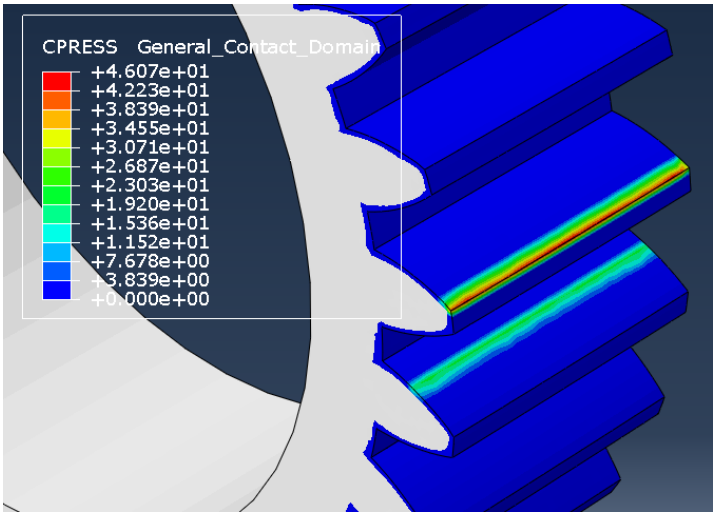

Figure 62.Contact temperature of dynamic simulation. unit: °C

According to the figure 62, the flash temperature after 2 seconds was 46 °C. The higher flash temperature on master gear was obtained at the edge between the top land and addendum tooth face, and heat generated on the slave gear was located at the pitch line of the gear tooth.

In terms of rotational speed of the gear, 1500 rpm and 50 revolutions were performed. Hence, it is acceptable that the flash temperature increased 20 Celsius in 2 second while this simulation was not yet validated by theoretical calculations and bulk temperature was not considered. However, by thermal camera test in section 4.6, in the first two second this simulation was followed in similar behaviour.

Chapter 8. Conclusions

In this report, different analyses of spur gear were carried out based on the Abaqus simulation and validated by hand calculation. The 3D simulation has been established which could provide satisfactory accuracy. Moreover, by using Fusion360, possible shape optimisation was provided, and by considering the shape optimization, the mechanical behaviour change via changes in the thickness of the gear rim was analysed. A misalignment simulation was carried out in this report. However, misalignment is usually caused by gear shaft bending, hence, by adding gear shaft connected with gear could make those simulations more realistic. Misalignment in the real world it could be multiple types of misalignment, and often comes with more than one misalignment situation, and hence it is useful to simulate the different combination of the misalignment.

Simulation of fibre reinforcement cantilever beam could provide a basic idea of how the filler could improve the mechanical performance, moreover, a reasonable orientation of the fibre filler could provide better mechanical results. By simulation of carbon fibre reinforcement PEEK, the way that carbon filler contributes to the mechanical performance was understood. However, carbon fibre normally comes in a much smaller scale compared to the simulation in the previous section, hence, this sub structure may not be accurate enough. Hence, in this simulation it is more important to focus on effect of the position of the carbon fibre within the PEEK gear, and the rigidity contribution to the gear tooth. Moreover, simulating gear meshing dynamically was overly complex, and considering only with thermal affect simulation was not enough to predict the performance of the gear, as wear and fatigue also need analysing.

Moreover the additive manufacturing process could be a key process to solve the fibre filler orientation problem in the fibre reinforcement polymer gear, as in the earlier stage of the additive

manufacture of polymer gear, there are still some improvements to be considered, for example, there was still small amount of peeling (bottom shrinkage) when printing the Nylon gear.

There were five different 3D printed materials tested: including Nylon 618, Nylon 645, alloy 910, Onyx and Markforged nylon. Comparisons between literature values for injection moulded nylon 66 gears and the five 3D printed gear types have been carried out. Nylon 618 provided better results when low to medium torque was applied compared with injection moulded gears. Different wear behaviour and wear patterns on the gear tooth were recorded by SEM. Interestingly, wear only occurred on the pitch line of 3D printed gear and for the Nylon 618 printed gears, parts of the gear tooth surface were melted but no materials were peeled off from the tooth, while the other four printed materials exhibited peeling of material from the gear tooth. In DSC tests, Nylon 66 and Nylon 618 showed relatively better thermal behaviour in terms of higher glass transition temperatures, higher melting temperatures and higher crystallinity when compared to the other materials tested. It is thus hypothesized that the superior Nylon 618 friction and wear performance (when compared to the other printed materials) is mainly dependent on the thermal behaviour and the level of sintering effect between each layer.

A set of experimental data was designed by sobol sequence, providing relatively higher tolerance and covering a much larger range of input data with minimal test data being required. Four 3D printing parameters were selected via specific requirement of polymer gears which require rigidity and light weight. A prediction model of 3D printed gears was carried out using with three models including an ANN model, a GA based ANN model and a leave one cross validation applied GA based ANN model. The results show that all models provide a relatively accurate prediction result and provide satisfactory fitting to the test data. A leave one cross validation applied model provides the strongest correlation with test results, with Pearson's r equal to 0.97 and R2 equal to

0.956 respectively. Moreover, by simulating an experiment, the printing parameters have been optimised to increase the performance of the 3D printed polymer gears. The results suggest an optimised setting of the 3D printer of printing temperature equal to 250°C, a printing speed of 70mm/s, a bed temperature of 25 °C and infill percentage of 80 %. The operational time of the resultant 3D printed polymer gear was increased more than 3 times compares with one produced using the default print settings. Sensitivity analysis performed by Garson's algorithm indicated that infill percentage has most influence on the performance of a 3D printed gear and bed temperature has the least influence on the test result.

Based on previous works, the parameters including printing speed, printing temperature, bed temperature and infill percentage have been separately investigated, and the result of the different parameters were correlated to the sensitive analysis which is shown by restricting three parameters and varying the infill percentage, which could increased optimised result by 25 hours compare with unoptimized result . Bed temperature could affect gear operational time by 4.5 hours, printing temperature could change result by 13.5. Meanwhile, printing speed could potentially change gear performance time by 20 hours. Moreover, the response of operational time to printing infill percentage can be modelled by a Boltzmann equation. Furthermore, bed temperature and printing temperature shown a sine response, and a peak appeared in certain temperature range. This discovery could be beneficial to the additive manufacturing process in terms of defining priorities printing task while retain reasonable quality. Infill percentage was the critical parameter to define gear body rigidity, hence a higher infill percentage could decrease the gear defamation and hence maintain the gear performance.

There are five different methods were used here to analyse the nylon materials: DSC, SAXS, WAXS, FTIR and XRF. Even though the manufacture of each printing filament could not provide

detail properties of each Nylon materials sufficiently, the detailed material characterization can be realized through above tests. A DSC test was carried out to analyse the crystallinity and phase transition temperature, while a WAXS test was also performed to illustrate the crystallinity which is similar to the DSC test. The domain size of the crystallinity for three different nylon filaments has been studied by SAXS, among which Nylon 618 has the largest domain size and so the optimum mechanical performance can be predicted. FTIR is employed to characterize the molecular structure of each material, which can affect the microstructure of Nylon materials. XRF points out the main ingredient of each materials is nylon, whereas, for each material there were minor difference in Cl, Ca and Fe elements.

There are five targets suggested which including Simulating polymer composite gear contact dynamically; Find suitable way to combine the dynamic simulation to predict gear performance, Simulate fibre reinforcement gear dynamically. Carry out testing of 3D printed gear via pre-examinations (Shrinkage, Porosity, and Crystallinity) and Improve gear performance by control the parameter of 3D printing process. In this section seven, different analyses of spur gears were carried out based on the Abaqus simulation and validated by hand calculation. 3D simulation was established which could provide higher accuracy. Moreover, possible shape optimisation was provided using Fusion360 and by considering the shape optimization, the mechanical behavioural change via changes the thickness of the gear rim was analysed. Misalignment simulation was carried out in this report, however, to increase the accuracy of the simulation, the gear shaft will be considered which will be more realistic, and misalignment in the real world will never be a single type of misalignment, and it often comes with more than one misalignment situation, and hence it is practical to simulate the different combination of misalignment.

The simulation of the fibre reinforcement cantilever beam could provide a basic idea of how the filler could improve the mechanical performance, moreover, a reasonable orientation of the fibre filler could provide better mechanical results. In the simulation of carbon fibre reinforcement PEEK, the way that carbon filler contributes to the mechanical performance was understood. However, carbon fibre normally comes in a much smaller scale compared to the simulation in the previous section, hence, this sub structure may not be accurate enough. Hence, in this simulation it is more important to focus on effect of the position of the carbon fibre within the PEEK gear, and also the rigidity contribution to the tear tooth. Moreover, simulating the gear meshing dynamically was overly complex, considering only with thermos affect simulation was not enough to predict the performance of the gear, the wear and fatigue simulation also need to be analysed.

Moreover, additive manufacturing processes could be key to solve the fibre filler orientation problem in fibre reinforcement polymer gear, as in the earlier stage of the additive manufacture of polymer gear, there is still some improvement to be considered, for example, there was still a small amount of appealing (bottom shrinkage) when printing the nylon gear.

8. 1 Limitations and future scope

The main limitation of this study is the lack of conventional materials information provided by the filament manufacturers. Both 3D printing filament manufacturers claim that the materials are based on Nylon 66 or a Nylon mixture, however no other compositional information is provided. It is noted that this area of 3D printed gears is certainly an area requiring future study. Firstly, further material analysis of available printing materials is required to give a better understanding of the key factors that influence the wear behaviour. Secondly, an investigation into optimisation methods for 3D printing parameters to enhance the performance of 3D printed gears is required.

Thirdly, a much wider analysis and comparison of the characteristics of polymer gears manufactured by different manufacturing processes including injection moulding, machine cutting and 3D printing is required.

Due to the unique characteristic of the ANN process, true correlation between each parameters was not fully studied. Moreover, more data points added to the model could increase accuracy of the simulation. There are several possible directions based on this research. Firstly, to carry out the study of the polymer molecular structure to explain the influence of different parameter settings. Secondly, investigating several other 3D printed materials in order to understand the correlation between different materials and create model to predict the performance of gears produced using different material and elicit the required print parameters.

References

1. Terry W. Additive manufacturing and 3D printing state of the industry. Annual Worldwide Progress Report Wohlers Associations. 2012.
2. Yousef S, Khattab A, Zaki M, Osman T. Wear characterization of carbon nanotubes reinforced polymer gears. IEEE Transactions on Nanotechnology. 2013;12(4):616-20.
3. BIEDERBICK K, Franck A. Kunststoff-Kompendium. Vogel Buchverlag, Würzburg; 1988.
4. Darlix B, Monasse B, Montmitonnet P. Hardness measurement as a means of determining simultaneously the elastic modulus and yield stress of polymers as a function of temperature. Polymer Testing. 1986;6(2):107-20.
5. Häger A, Davies M. Short-fibre reinforced, high-temperature resistant polymers for a wide field of tribological applications. Composite Materials Series. 8: Elsevier; 1993. p. 107-57.
6. Friedrich K, Zhang Z, Schlarb AK. Effects of various fillers on the sliding wear of polymer composites. Composites science and technology. 2005;65(15-16):2329-43.
7. Briscoe B. The tribology of composite materials: a preface. Composite Materials Series. 8: Elsevier; 1993. p. 3-15.
8. Voort JV, Bahadur S. The growth and bonding of transfer film and the role of CuS and PTFE in the tribological behavior of PEEK. Wear. 1995;181:212-21.
9. Xue Q-J, Wang Q-H. Wear mechanisms of polyetheretherketone composites filled with various kinds of SiC. Wear. 1997;213(1-2):54-8.
10. Davim JP, Cardoso R. Effect of the reinforcement (carbon or glass fibres) on friction and wear behaviour of the PEEK against steel surface at long dry sliding. Wear. 2009;266(7-8):795-9.
11. Mishra S, Mohanty A, Drzal L, Misra M, Parija S, Nayak S, et al. Studies on mechanical performance of biofibre/glass reinforced polyester hybrid composites. Composites Science and Technology. 2003;63(10):1377-85.
12. Xing X, Li R. Wear behavior of epoxy matrix composites filled with uniform sized sub-micron spherical silica particles. Wear. 2004;256(1-2):21-6.
13. Mao K, Li W, Hooke C, Walton D. Friction and wear behaviour of acetal and nylon gears. Wear. 2009;267(1-4):639-45.
14. Mao K, Li W, Hooke C, Walton D. Polymer gear surface thermal wear and its performance prediction. Tribology International. 2010;43(1-2):433-9.
15. Kurokawa M, Uchiyama Y, Nagai S. Performance of plastic gear made of carbon fiber reinforced poly-ether-ether-ketone. Tribology International. 1999;32(9):491-7.
16. Kurokawa M, Uchiyama Y, Nagai S. Performance of plastic gear made of carbon fiber reinforced poly-ether-ether-ketone: Part 2. Tribology International. 2000;33(10):715-21.
17. Senthilvelan S, Gnanamoorthy R. Influence of reinforcement on composite gear metrology. Mechanism and machine theory. 2008;43(9):1198-209.
18. Reddy J. An introduction to the finite element method: McGraw-Hill New York, USA; 2004.
19. Hrennikoff A. Solution of problems of elasticity by the framework method. J appl Mech. 1941.
20. Courant R. Variational methods for the solution of problems of equilibrium and vibrations: Verlag nicht ermittelbar; 1943.
21. Asker HK. THREE DIMENSIONAL DYNAMIC STRESS ANALYSES FOR A GEAR TEETH USING FINITE ELEMENT METHOD. 2006.
22. Karaveer V, Mogrekar A, Joseph TPR. Modeling and finite element analysis of spur gear. International Journal of Current Engineering and Technology. 2013;3(5):2104-7.
23. AL-Qrimli HF, Abdelrhman AM, Hadi HM, Mohammed RK, Sultan HS. Times three dimensional spur gear static contact investigations using finite element method. Modern Applied Science. 2016;10(5):145-50.

24. Xin W KWN, Ying P, Jong B,, Jee H, Anthony G. Finite Element Simulation of Thermography Non-destructive Testing for Gear Inspection NDT Conference2010.

25. Goda T, Váradi K, Friedrich K, Giertzsch H. Finite element analysis of a polymer composite subjected to a sliding steel asperity part I normal fibre orientation. Journal of materials science. 2002;37(8):1575-83.
26. Friedrich K, Varadi K, Goda T, Giertzsch H. Finite element analysis of a polymer composite subjected to a sliding steel asperity Part II: Parallel and anti-parallel fibre orientations. Journal of Materials Science. 2002;37(16):3497-507.
27. Chawla KK. Composite materials: science and engineering: Springer Science & Business Media; 2012.
28. Langlois P, Al B, Harris O. Hybrid Hertzian and FE-based helical gear-loaded tooth contact analysis and comparison with FE. Gear Technology. 2016;6:54-7.
29. Bravo A, Koffi D, Toubal L, Erchiqui F. Life and damage mode modeling applied to plastic gears. Engineering Failure Analysis. 2015;58:113-33.
30. Wong KV, Hernandez A. A review of additive manufacturing. ISRN Mechanical Engineering. 2012;2012.
31. Kruth J-P, Leu M-C, Nakagawa T. Progress in additive manufacturing and rapid prototyping. Cirp Annals. 1998;47(2):525-40.
32. Noorani R. Rapid prototyping: principles and applications. 2006.
33. Berman B. 3-D printing: The new industrial revolution. Business horizons. 2012;55(2):155-62.
34. Jones R, Mao K, Phang A, Allen B. Effects of linear and angular misalignment on a spur gear pair. Insight-Non-Destructive Testing and Condition Monitoring. 2011;53(8):420-5.
35. Mao K, Li W, Hooke C, Walton DJW. Friction and wear behaviour of acetal and nylon gears. 2009;267(1-4):639-45.
36. Wohlers T. Additive Manufacturing and 3D Printing State of the Industry; Wohlers Associates: Fort Collins, CO, USA, 2015. ISBN 978-0-9913332-1-9; 2013.
37. Wong KV, Hernandez AJIME. A review of additive manufacturing. 2012;2012.
38. Leigh SJ, Bradley RJ, Purssell CP, Billson DR, Hutchins DAJPo. A simple, low-cost conductive composite material for 3D printing of electronic sensors. 2012;7(11):e49365.
39. Christ JF, Aliheidari N, Ameli A, Pötschke PJM, Design. 3D printed highly elastic strain sensors of multiwalled carbon nanotube/thermoplastic polyurethane nanocomposites. 2017;131:394-401.
40. Blok LG, Longana ML, Yu H, Woods BKJAM. An investigation into 3D printing of fibre reinforced thermoplastic composites. 2018;22:176-86.
41. Kalin M, Kupec AJ. The dominant effect of temperature on the fatigue behaviour of polymer gears. Wear. 2017;376:1339-46.
42. Hu Z, Mao K. An investigation of misalignment effects on the performance of acetal gears. Tribology International. 2017;116:394-402.
43. Weng Z, Wang J, Senthil T, Wu LJM, Design. Mechanical and thermal properties of ABS/montmorillonite nanocomposites for fused deposition modeling 3D printing. 2016;102:276-83.
44. Torrado AR, Shemelya CM, English JD, Lin Y, Wicker RB, Roberson DAJAM. Characterizing the effect of additives to ABS on the mechanical property anisotropy of specimens fabricated by material extrusion 3D printing. 2015;6:16-29.
45. Gupta A, Harsha SJPMS. Analysis of mechanical properties of carbon nanotube reinforced polymer composites using continuum mechanics approach. 2014;6:18-25.
46. Singh S, Ramakrishna S, Singh RJJoMP. Material issues in additive manufacturing: A review. 2017;25:185-200.

47. Dickson AN, Ross K-A, Dowling DPJCS. Additive manufacturing of woven carbon fibre polymer composites. 2018;206:637-43.
48. Singh PK, Singh AKJMTP. An investigation on the effects of the various techniques over the performance and durability of polymer gears. 2017;4(2):1606-14.
49. Tavčar J, Grkman G, Duhovnik JJJoAMD, Systems,, Manufacturing. Accelerated lifetime testing of reinforced polymer gears. 2018;12(1):JAMDSM0006-JAMDSM.
50. dos Santos WN, De Sousa J, Gregorio Jr RJPT. Thermal conductivity behaviour of polymers around glass transition and crystalline melting temperatures. 2013;32(5):987-94.
51. Carraher CE, Seymour RB. SeymourCarraher's polymer chemistry: an introduction: Dekker; 1996.
52. Zhang Y, Purssell C, Mao K, Leigh S. A physical investigation of wear and thermal characteristics of 3D printed nylon spur gears. Tribology International. 2020;141:105953.
53. Hooke C, Mao K, Walton D, Breeds A, Kukureka SJJot. Measurement and prediction of the surface temperature in polymer gears and its relationship to gear wear. 1993;115(1):119-24.
54. Gauvin RJGT, The J. of the Gear Manufacturing. Maximum Surface'Temperature0'£'the'Thermoplastic Gear in a Non-Lubricated Plastic/Steel Gear'Pair'. 1984:20-7.
55. Mao K. A numerical method for polymer composite gear flash temperature prediction. 2007;262(11-12):1321-9.
56. Chacón J, Caminero MA, García-Plaza E, Núñez PJJM, Design. Additive manufacturing of PLA structures using fused deposition modelling: Effect of process parameters on mechanical properties and their optimal selection. 2017;124:143-57.
57. Gomez-Gras G, Jerez-Mesa R, Travieso-Rodriguez JA, Lluma-Fuentes JJM, Design. Fatigue performance of fused filament fabrication PLA specimens. 2018;140:278-85.
58. Kuznetsov VE, Solonin AN, Tavitov AG, Urzhumtcev OD, Vakulik AH. Increasing Strength of FFF 3D Printed Parts by Influencing on Temperature-Related Parameters of the Process. 2019.
59. Prajapati H, Ravoori D, Woods RL, Jain AJAM. Measurement of anisotropic thermal conductivity and inter-layer thermal contact resistance in polymer fused deposition modeling (FDM). 2018;21:84-90.
60. Bellehumeur C, Li L, Sun Q, Gu PJJoMP. Modeling of bond formation between polymer filaments in the fused deposition modeling process. 2004;6(2):170-8.
61. Sun Q, Rizvi G, Bellehumeur C, Gu PJRPJ. Effect of processing conditions on the bonding quality of FDM polymer filaments. 2008;14(2):72-80.
62. Wang M, Zhu Z, Dong Y, Zhou L. Study of mixed-mode I/II fractures using single cleavage semicircle compression specimens under impacting loads. Engineering Fracture Mechanics. 2017;177:33-44.
63. Deng L, Feng B, Zhang YJCI. An optimization method for multi-objective and multi-factor designing of a ceramic slurry: Combining orthogonal experimental design with artificial neural networks. 2018;44(13):15918-23.
64. Koeppe A, Padilla CAH, Voshage M, Schleifenbaum JH, Markert BJML. Efficient numerical modeling of 3D-printed lattice-cell structures using neural networks. 2018;15:147-50.
65. Delli U, Chang SJPM. Automated process monitoring in 3D printing using supervised machine learning. 2018;26:865-70.
66. Li W, Lin W, Yu JJN. Predicting contact characteristics for helical gear using support vector machine. 2016;174:1156-61.
67. Sun S, Wang S, Wang Y, Lim TC, Yang YJM, Theory M. Prediction and optimization of hobbing gear geometric deviations. 2018;120:288-301.
68. Samanta BJMs, processing s. Gear fault detection using artificial neural networks and support vector machines with genetic algorithms. 2004;18(3):625-44.
69. Hadavandi E, Shahrabi J, Hayashi YJSC. SPMoE: a novel subspace-projected mixture of experts model for multi-target regression problems. 2016;20(5):2047-65.

70. Melki G, Cano A, Kecman V, Ventura SJIS. Multi-target support vector regression via correlation regressor chains. 2017;415:53-69.
71. Michalski RS, Carbonell JG, Learning TMM. An Artificial Intelligence Approach. Understanding the Nature of Learning. 1983;2:3-26.
72. Turing AM. Computing machinery and intelligence. Mind. 1950;59(236):433-60.
73. Rosenblatt F. The perceptron: A probabilistic model for information storage and organization in the brain. Psychological review. 1958;65(6):386.
74. Cover T, Hart P. Nearest neighbor pattern classification. IEEE transactions on information theory. 1967;13(1):21-7.
75. Winston PH. Learning structural descriptions from examples. 1970.
76. Wang S-C. Artificial neural network. Interdisciplinary computing in java programming: Springer; 2003. p. 81-100.
77. Rumelhart DE, Hinton GE, Williams RJ. Learning representations by back-propagating errors. Cognitive modeling. 1988;5(3):1.
78. Quinlan JR. Induction of decision trees. Machine learning. 1986;1(1):81-106.
79. Breiman L, Friedman J, Stone CJ, Olshen RA. Classification and regression trees: CRC press; 1984.
80. Vapnik V. Pattern recognition using generalized portrait method. Automation and remote control. 1963;24:774-80.
81. Vapnik VN, Chervonenkis AJ. Theory of pattern recognition. 1974.
82. Cortes C, Vapnik V. Support-vector networks. Machine learning. 1995;20(3):273-97.
83. Boser BE, Guyon IM, Vapnik VN, editors. A training algorithm for optimal margin classifiers. Proceedings of the fifth annual workshop on Computational learning theory; 1992: ACM.
84. Noble WS. What is a support vector machine? Nature biotechnology. 2006;24(12):1565-7.
85. LeCun Y, Bengio Y, Hinton G. Deep learning. Nature. 2015;521(7553):436-44.
86. Hinton GE, Osindero S, Teh Y-W. A fast learning algorithm for deep belief nets. Neural computation. 2006;18(7):1527-54.
87. Joachims T. Text categorization with support vector machines: Learning with many relevant features. Machine learning: ECML-98. 1998:137-42.
88. Scholkopf B, Smola AJ. Learning with kernels: support vector machines, regularization, optimization, and beyond: MIT press; 2001.
89. Cristianini N, Shawe-Taylor J. An introduction to support vector machines and other kernel-based learning methods: Cambridge university press; 2000.
90. Schölkopf B, Burges C, Vapnik V. Incorporating invariances in support vector learning machines. Artificial Neural Networks—ICANN 96. 1996:47-52.
91. Chaplot S, Patnaik L, Jagannathan N. Classification of magnetic resonance brain images using wavelets as input to support vector machine and neural network. Biomedical Signal Processing and Control. 2006;1(1):86-92.
92. Smola AJ, Schölkopf B. A tutorial on support vector regression. Statistics and computing. 2004;14(3):199-222.
93. Hsu C-W, Lin C-J. A comparison of methods for multiclass support vector machines. IEEE transactions on Neural Networks. 2002;13(2):415-25.
94. Hong DH, Hwang C. Support vector fuzzy regression machines. Fuzzy sets and systems. 2003;138(2):271-81.
95. Wu C-H, Ho J-M, Lee D-T. Travel-time prediction with support vector regression. IEEE transactions on intelligent transportation systems. 2004;5(4):276-81.
96. Park J, Kim Y, Eom I, Lee K. Economic load dispatch for piecewise quadratic cost function using Hopfield neural network. IEEE Transactions on Power Systems. 1993;8(3):1030-8.

97. Paik JK, Katsaggelos AK. Image restoration using a modified Hopfield network. IEEE Transactions on image processing. 1992;1(1):49-63.
98. Zhu Y, Yan Z. Computerized tumor boundary detection using a Hopfield neural network. IEEE transactions on medical imaging. 1997;16(1):55-67.
99. Ferentinou M, Hasiotis T, Sakellariou M. Application of computational intelligence tools for the analysis of marine geotechnical properties in the head of Zakynthos canyon, Greece. Computers & geosciences. 2012;40:166-74.
100. Rizzo R, Allegra M, Fulantelli G, editors. Hypertext-like structures through a SOM network. Proceedings of the tenth ACM Conference on Hypertext and hypermedia: returning to our diverse roots: returning to our diverse roots; 1999: ACM.
101. Kohavi R, editor Scaling Up the Accuracy of Naive-Bayes Classifiers: A Decision-Tree Hybrid. KDD; 1996.
102. Freund Y, Mason L, editors. The alternating decision tree learning algorithm. icml; 1999.
103. Magerman DM, editor Statistical decision-tree models for parsing. Proceedings of the 33rd annual meeting on Association for Computational Linguistics; 1995: Association for Computational Linguistics.
104. Abonyi J, Roubos JA, Szeifert F. Data-driven generation of compact, accurate, and linguistically sound fuzzy classifiers based on a decision-tree initialization. International journal of approximate reasoning. 2003;32(1):1-21.
105. Umanol M, Okamoto H, Hatono I, Tamura H, Kawachi F, Umedzu S, et al., editors. Fuzzy decision trees by fuzzy ID3 algorithm and its application to diagnosis systems. Fuzzy Systems, 1994 IEEE World Congress on Computational Intelligence, Proceedings of the Third IEEE Conference on; 1994: IEEE.
106. Miller CJ, Nichol RC, Reichart D, Wechsler RH, Evrard AE, Annis J, et al. The C4 clustering algorithm: clusters of galaxies in the sloan digital sky survey. The Astronomical Journal. 2005;130(3):968.
107. Denison DG, Mallick BK, Smith AF. A bayesian CART algorithm. Biometrika. 1998;85(2):363-77.
108. Pisanti O, Cirillo A, Esposito S, Iocco F, Mangano G, Miele G, et al. PArthENoPE: Public algorithm evaluating the nucleosynthesis of primordial elements. Computer Physics Communications. 2008;178(12):956-71.
109. Azadeh A, Saberi M, Moghaddam RT, Javanmardi L. An integrated data envelopment analysis–artificial neural network–rough set algorithm for assessment of personnel efficiency. Expert Systems with Applications. 2011;38(3):1364-73.
110. Fonarow GC, Adams KF, Abraham WT, Yancy CW, Boscardin WJ, Committee ASA. Risk stratification for in-hospital mortality in acutely decompensated heart failure: classification and regression tree analysis. Jama. 2005;293(5):572-80.
111. Hess KR, Abbruzzese MC, Lenzi R, Raber MN, Abbruzzese JL. Classification and regression tree analysis of 1000 consecutive patients with unknown primary carcinoma. Clinical Cancer Research. 1999;5(11):3403-10.
112. Munprom R, Limtasiri S. Optimization of stereolithographic 3D printing parameters using Taguchi method for improvement in mechanical properties. Materials Today: Proceedings. 2019;17:1768-73.
113. Sanatgar RH, Campagne C, Nierstrasz V. Investigation of the adhesion properties of direct 3D printing of polymers and nanocomposites on textiles: Effect of FDM printing process parameters. Applied Surface Science. 2017;403:551-63.
114. Tay YWD, Li MY, Tan MJ. Effect of printing parameters in 3D concrete printing: printing region and support structures. Journal of Materials Processing Technology. 2019;271:261-70.
115. Chacón J, Caminero MA, García-Plaza E, Núnez PJ. Additive manufacturing of PLA structures using fused deposition modelling: Effect of process parameters on mechanical properties and their optimal selection. Materials & Design. 2017;124:143-57.

116. Covolan VL, Volpe PL, Plivelic TS, Torriani IL. Polystyrene latex by dispersion polymerization: real time SAXS measurements. Colloids and Surfaces A: Physicochemical and Engineering Aspects. 2002;204(1-3):211-25.
117. Kuznetsov VE, Solonin AN, Tavitov AG, Urzhumtsev OD, Vakulik AH. Increasing of strength of FDM (FFF) 3d printed parts by influencing on temperature-related parameters of the process. Rapid Prototyp J Epub ahead of print. 2018;9.
118. Prajapati H, Ravoori D, Woods RL, Jain A. Measurement of anisotropic thermal conductivity and inter-layer thermal contact resistance in polymer fused deposition modeling (FDM). Additive Manufacturing. 2018;21:84-90.
119. Bellehumeur C, Li L, Sun Q, Gu P. Modeling of bond formation between polymer filaments in the fused deposition modeling process. Journal of manufacturing processes. 2004;6(2):170-8.
120. Sun Q, Rizvi G, Bellehumeur C, Gu P. Effect of processing conditions on the bonding quality of FDM polymer filaments. Rapid Prototyping Journal. 2008.
121. Kennedy M, Peacock A, Failla M, Lucas J, Mandelkern L. Tensile properties of crystalline polymers: random copolymers of ethylene. Macromolecules. 1995;28(5):1407-21.
122. Ricci G, Leone G, Boccia AC, Pierro I, Zanchin G, Mauri M, et al. Perfectly alternating ethylene/2-butene copolymers by hydrogenation of highly stereoregular 1, 4-Poly (1, 3-diene) s: Synthesis and characterization. Macromolecules. 2017;50(3):754-61.
123. Duraccio D, Mauriello A, Cimmino S, Silvestre C, Auriemma F, De Rosa C, et al. Structure–property relationships in polyethylene based films obtained by blow molding as model system of industrial relevance. European Polymer Journal. 2015;62:97-107.
124. Pierro I, Leone G, Zanchin G, Canetti M, Ricci G, Bertini F. Polyolefin thermoplastic elastomers from 1-octene copolymerization with 1-decene and cyclopentene. European Polymer Journal. 2017;93:200-11.
125. Leone G, Mauri M, Pierro I, Ricci G, Canetti M, Bertini F. Polyolefin thermoplastic elastomers from 1-octene chain-walking polymerization. Polymer. 2016;100:37-44.
126. Reddy JN. An introduction to the finite element method. New York. 1993.
127. Singh PK, Singh AKJTI. An investigation on the thermal and wear behavior of polymer based spur gears. 2018;118:264-72.
128. Sobol' IyMJZVnMiMF. On the distribution of points in a cube and the approximate evaluation of integrals. 1967;7(4):784-802.
129. Kshirsagar A P RMN. Article: Artificial Neural Network. IJCA Proceedings on National Conference on Recent Trends in Computing 2 2012:12-6.
130. Quinlan JR. C4. 5: programs for machine learning: Elsevier; 2014.
131. Mohamad ET, Armaghani DJ, Momeni E, Yazdavar A, Ebrahimi M. Rock strength estimation: a PSO-based BP approach. Neural Computing and Applications. 2018;30(5):1635-46.
132. Dormishi A, Ataei M, Khaloo Kakaie R, Mikaeil R, Shaffiee Haghshenas S. Performance evaluation of gang saw using hybrid ANFIS-DE and hybrid ANFIS-PSO algorithms. Journal of Mining and Environment. 2019;10(2):543-57.
133. Babanouri N, Nasab SK, Sarafrazi S. A hybrid particle swarm optimization and multi-layer perceptron algorithm for bivariate fractal analysis of rock fractures roughness. International Journal of Rock Mechanics and Mining Sciences. 2013;60:66-74.
134. Holland JH. Adaptation in natural and artificial systems: an introductory analysis with applications to biology, control, and artificial intelligence: MIT press; 1992.
135. Chipperfield AJ, Fleming P, Pohlheim H. Genetic Algorithm Toolbox: For Use with MATLAB; User's Guide (version 1.2): University of Sheffield, Department of Automatic Control and Systems Engineering; 1994.

136. Simpson AR, Dandy GC, Murphy LJJJowrp, management. Genetic algorithms compared to other techniques for pipe optimization. 1994;120(4):423-43.
137. Jadav K, Panchal MP. Optimizing weights of artificial neural networks using genetic algorithms. Int J Adv Res Comput Sci Electron Eng. 2012;1(10):47-51.
138. Vose MD. The simple genetic algorithm: foundations and theory: MIT press; 1999.
139. Houck CR, Joines J, Kay MG. A genetic algorithm for function optimization: a Matlab implementation. Ncsu-ie tr. 1995;95(09):1-10.
140. Wong T-T. Performance evaluation of classification algorithms by k-fold and leave-one-out cross validation. Pattern Recognition. 2015;48(9):2839-46.
141. Garson GD. Interpreting neural-network connection weights. AI expert. 1991;6(4):46-51.
142. Momeni E, Nazir R, Armaghani DJ, Maizir HJM. Prediction of pile bearing capacity using a hybrid genetic algorithm-based ANN. 2014;57:122-31.
143. Goh AT. Back-propagation neural networks for modeling complex systems. Artificial Intelligence in Engineering. 1995;9(3):143-51.
144. Garson GDAe. Interpreting neural-network connection weights. 1991;6(4):46-51.
145. Goh AT. Back-propagation neural networks for modeling complex systems. Artificial Intelligence in Engineering. 1995;9(3):143-51.
146. Lincoln DM, Vaia RA, Krishnamoorti R. Isothermal Crystallization of Nylon-6/Montmorillonite Nanocomposites. Macromolecules. 2004;37(12):4554-61.
147. Ultimaker. Nylon618 features http://taulman3d.com/618-features.html http://taulman3d.com/618-features.html. Accessed on: 15th Apr 2017
148. Ultimaker. Nylon645 features http://taulman3d.com/nylon-645-spec.html http://taulman3d.com/nylon-645-spec.html Accessed on: 15th Apr 2017
149. Ultimaker. Alloy910 features http://taulman3d.com/alloy-910-spec.html http://taulman3d.com/alloy-910-spec.html Accessed on: 15th Apr 2017
150. https://markforged.com/landing/material-data-sheet/ M. Data sheet https://markforged.com/landing/material-data-sheet/ Accessed on: 20th Dec 2017
151. Friedrich K. Friction and wear of polymer composites: Elsevier; 2012.
152. Lancaster JJT. Estimation of the limiting PV relationships for thermoplastic bearing materials. 1971;4(2):82-6.
153. A Breeds SK, K Mao, CJ Hooke, D WaltonA Breeds, S Kukureka, K Mao, CJ Hooke, D Walton. Wear behaviour of acetal gear pairs. Wear. 1993;166(1):85-91.
154. Lee SS, Phillips PJJEPJ. Melt crystallized polyamide 6.6 and its copolymers, Part I. Melting point–Lamellar thickness relations in the homopolymer. 2007;43(5):1933-51.
155. Sezer HK, Eren OJJoMP. FDM 3D printing of MWCNT re-inforced ABS nano-composite parts with enhanced mechanical and electrical properties. 2019;37:339-47.
156. Bonnet MJVTV. Plastics in engineering applications: properties, processing and practical use of polymeric materials. 2008.
157. Blaeser A, Duarte Campos DF, Puster U, Richtering W, Stevens MM, Fischer HJAhm. Controlling shear stress in 3D bioprinting is a key factor to balance printing resolution and stem cell integrity. 2016;5(3):326-33.
158. Mao K. A numerical method for polymer composite gear flash temperature prediction. Wear. 2007;262(11-12):1321-9.
159. Lee Rodgers J, Nicewander WAJTAS. Thirteen ways to look at the correlation coefficient. 1988;42(1):59-66.
160. Stigler SM. Francis Galton's account of the invention of correlation. Statistical Science. 1989:73-9.

161. Covolan VL, Volpe PLO, Plivelic TS, Torriani IL. Polystyrene latex by dispersion polymerization: real time SAXS measurements. Colloids and Surfaces A: Physicochemical and Engineering Aspects. 2002;204(1):211-25.
162. Bale HD, Schmidt PW. Small-Angle X-Ray-Scattering Investigation of Submicroscopic Porosity with Fractal Properties. Physical Review Letters. 1984;53(6):596-9.
163. Chiarello R, Panella V, Krim J, Thompson C. X-ray reflectivity and adsorption isotherm study of fractal scaling in vapor-deposited films. Physical Review Letters. 1991;67(24):3408-11.
164. Cocco G, Enzo S, Galvagno S, Poltarzewski Z, Pietropaolo R. X-ray scattering structural investigation of Pt and Pt–Sn catalysts supported on nylon. Journal of the Chemical Society, Faraday Transactions 1: Physical Chemistry in Condensed Phases. 1985;81(2):321-33.
165. Prevorsek DC, Chin HB. Intrinsic Differences between Nylon 6 and Nylon 66 Industrial Fibers: Micromechanical and Molecular Analysis. International Journal of Polymeric Materials and Polymeric Biomaterials. 1994;25(3-4):161-84.
166. Nair SS, Ramesh C. Studies on the Crystallization Behavior of Nylon-6 in the Presence of Layered Silicates Using Variable Temperature WAXS and FTIR. Macromolecules. 2005;38(2):454-62.
167. Khanna YP, Kuhn WP. Measurement of crystalline index in nylons by DSC: Complexities and recommendations. Journal of Polymer Science Part B: Polymer Physics. 1997;35(14):2219-31.
168. Charles J, Ramkumaar GR, Azhagiri S, Gunasekaran S. FTIR and Thermal Studies on Nylon-66 and 30% Glass Fibre Reinforced Nylon-66 %J E-Journal of Chemistry. E-Journal of Chemistry. 2009;6(1):23-33.
169. Shigley JE. Shigley's mechanical engineering design: Tata McGraw-Hill Education; 2011.
170. Abdelrhman AM, AL-Qrimli HF, Hadi HM, Mohammed RK, Sultan HS. Times Three Dimensional Spur Gear Static Contact Investigations Using Finite Element Method. Modern Applied Science. 2016;10(5):145.
171. Bibel G, Reddy S, Savage M, Handschuh R. Effects of rim thickness on spur gear bending stress. Journal of Mechanical Design. 1994;116(4):1157-62.

Appendices: key MATLAB codes developed in this work.

A1. Sobol sequence generate.

```
clear all
close all
clc

X=i4_sobol_generate(4,70,0);
Temperature=230+X(1,:)*45;
Speed=25+X(2,:)*50;
BedT=30+X(3,:)*40;
Infill=20+X(4,:)*60;
Input(:,1)=Temperature';
Input(:,2)=Speed';
Input(:,3)=BedT';
Input(:,4)=Infill';
save('Input.dat', '-ascii', 'Input')
```

A2. Artificial neural network model.

```
% code to establish machine learning model
clear all
close all
clc

% Input data

input=xlsread('test rig input.xlsx');
%test1=xlsread('test1.xlsx');
output=xlsread('test rig output.xlsx');

%Divide training set and test set
k=rand(1,50);
[ m, n]=sort(k);
input_train= input(:,n( 1:45));
output_train = output(:,n(1: 45));
input_test= input(:,n(46:50));
output_test=output(:,n(46:50));


%without Divide training set and test set
%input_train= input(1:18);
%output_train = output(1: 18);
%input_test= input(19:21);
%output_test=output(19:21);
```

```
%Normalised%%
[intrain, ps_input] = mapminmax(input_train,0,1);
intest= mapminmax('apply',input_test,ps_input);

[outtrain, ps_output] = mapminmax(output_train,0,1);

% build net %%%%%
hiddenSizes =7; % default 10
trainFcn = 'trainlm'; % default trainlm(LM) trainbfg(newton)
net=feedforwardnet(hiddenSizes,trainFcn);
% net.trainParam.lr=0.1;
% net.performFcn = 'mae';
% net.trainparam.epochs=6000; %max epochs
% net.trainparam.goal=0.00001; %target perfromance error


[net,tr]=train(net,intrain,outtrain);
test_out=sim(net,intest);

%%Simulation
test_out1=sim(net,test1);


data_real=input(1,length(input)-2:end);



%Renormalised%%
T_sim = mapminmax('reverse',test_out,ps_output);




%The evaluation of preformance
% 1.error
error = abs(T_sim - output_test)./output_test;

%
% 2. R^2
R2 = (5 * sum(T_sim .* output_test) - sum(T_sim) * sum(output_test))^2
/ ((5 * sum((T_sim).^2) - (sum(T_sim))^2) * (5 * sum((output_test).^2)
- (sum(output_test))^2));


%
% 3. Comparsion
result=[output_test' T_sim' error'];

%extract necwork weight
answ=net.iw;
ansb=net.b;
```

```
% Figure
figure
plot(1:5,output_test,'b:*',1:5,T_sim,'r-o')
legend('Real value','Predicted value')
xlabel('Sample')
ylabel('S/N Ratio')
string = {'Comparsion';['R^2=' num2str(R2)]};
title(string)
```

A3. Artificial neural network with genetic algorithm.

```
%%%% code to establish machine learning model
clear all
close all
clc

%%%% Input data

input=xlsread('test rig input.xlsx');
output=xlsread('test rig output.xlsx');


k=rand(1,50);
[ m, n]=sort(k);
input_train= input(:,n( 1:45));
output_train = output(:,n(1: 45));
input_test= input(:,n(46:50));
output_test=output(:,n(46:50));
%%Normalised%%


%%Normalised%%
[intrain, ps_input] = mapminmax(input_train,0,1);
intest= mapminmax('apply',input_test,ps_input);

[outtrain, ps_output] = mapminmax(output_train,0,1);

%%Selecting the optimal hidensize%%
for i=1:20


hiddenSizes =i;
trainFcn = 'trainlm';
net=feedforwardnet(hiddenSizes,trainFcn);


[net,tr]=train(net,intrain,outtrain);
test_out=sim(net,intest);
```

```
%%Renormalised%%
T_sim = mapminmax('reverse',test_out,ps_output);



error = abs(T_sim - output_test)./output_test;
%error = abs(T_sim - output_test);
%error1=error
%error=error(1)+error(2)+error(3);
a1(i)=error;
a(i)=1/error;
S(i,:)=T_sim;

end

num=size(a,2);
max_grad=0;
index=1;
for i=1:size(a,2)
    max_grad=a(i);
    for j=1:size(a,2)
        if j~=i
            if a(j)>=max_grad
                max_grad=a(j);
                index=j;

            end

        end

    end

end

fprintf('The optimal hiddensize is %-5f',index);

error=a1(index);
%error=error/3;

T_sim = S(index,:)



%%Structure of network
inputnum=4;
hiddennum=index;
outputnum=1;

%%Genetic algorithm

hiddenSizes =index;
trainFcn = 'trainlm';
```

```
net=feedforwardnet(hiddenSizes,trainFcn);

%%Iteration number
maxgen=100;
%%Population size
sizepop=5;
%%Cross probability
pcross=[0.4];
%%Mutation probability
pmutation=[0.2];

%%Toatal joint number
numsum=inputnum*hiddennum+hiddennum+hiddennum*outputnum+outputnum;

lenchrom=ones(1,numsum);
bound=[-3*ones(numsum,1) 3*ones(numsum,1)];

%%Structure of population
individuals=struct('fitness',zeros(1,sizepop),'chrom',[]);
avgfitness=[];
bestfitness=[];
bestchrom=[];

%%Calculation of individual fitness
for i=1:sizepop

    individuals.chrom(i,:)=Code(lenchrom,bound);

    x=individuals.chrom(i,:);

individuals.fitness(i)=fun(x,inputnum,hiddennum,outputnum,net,intrain,
outtrain);
end
FitRecord=[];

[bestfitness bestindex]=min(individuals.fitness);
bestchrom=individuals.chrom(bestindex,:);
avgfitness=sum(individuals.fitness)/sizepop; %


trace01=[avgfitness bestfitness];


for i=1:maxgen

    %%Selection
    individuals=select(individuals,sizepop);

    %%Cross

individuals.chrom=Cross(pcross,lenchrom,individuals.chrom,sizepop,boun
d);
```

```
    %%Mutation

individuals.chrom=Mutation(pmutation,lenchrom,individuals.chrom,sizepo
p,i,maxgen,bound);

    %%Calculating fitness
    for j=1:sizepop
        x=individuals.chrom(j,:);

individuals.fitness(j)=fun(x,inputnum,hiddennum,outputnum,net,intrain,
outtrain);
    end
        %%Finding optimal individual
        [newbestfitness,newbestindex]=min(individuals.fitness);
        [worestfitness,worestindex]=max(individuals.fitness);

        %%Updating optimal individual
        if bestfitness>newbestfitness
            bestfitness=newbestfitness;
            bestchrom=individuals.chrom(newbestindex,:);

        individuals.chrom(worestindex,:)=bestchrom;
        individuals.fitness(worestindex)=bestfitness;
        end
        %%Calculating fitness of optimal individual
        avgfitness=sum(individuals.fitness)/sizepop;
       trace01=[trace01;avgfitness bestfitness];
    FitRecord=[FitRecord;individuals.fitness];
    end


   %%Results analysis
 figure(1)
[r c]=size(trace01);
plot([1:r],trace01(:,2),'b--');
title(['Error Fitness ' 'Final iteration' num2str(maxgen)]);
xlabel('Iteration number');ylabel('Fitness');
legend('Average fitness','Optimal fitness');
disp('Fitness                  varibale');

    %%Assigning optimal individual to network
   x=bestchrom
   w1=x(1:inputnum*hiddennum);
   B1=x(inputnum*hiddennum+1:inputnum*hiddennum+hiddennum);

w2=x(inputnum*hiddennum+hiddennum+1:inputnum*hiddennum+hiddennum+hidde
nnum*outputnum);

B2=x(inputnum*hiddennum+hiddennum+hiddennum*outputnum+1:inputnum*hidde
nnum+hiddennum+hiddennum*outputnum+outputnum);
```

```
    net=configure(net,intrain,outtrain)

    net.iw{1,1}=reshape(w1,hiddennum,inputnum);
    net1w{2,1}=reshape(w2,outputnum,hiddennum);
    net.b{1}=reshape(B1,hiddennum,1);
    net.b{2}=B2;



%%Training network
%%Parameters of network
net.trainParam.epochs=100;
net.trainParam.lr=0.1;
net.trainParam.goal=0.00001;


%%Training network
[net,tr]=train(net,intrain,outtrain);
test_out=sim(net,intest);

%%Renormalised%%
T_sim = mapminmax('reverse',test_out,ps_output);

%%figure
%figure
%plot(1:4000,input_train,'bo');hold on;
%plot(1:2000,input_test','go');
%plot(1:4000,output_train,'k+');
%plot(1:2000,T_sim,'r*');

answ=net.iw;
ansb=net.b;

%%Simulation
%test_out1=sim(net,Orthogonal expeimental test.xlsx);
%data_simulation=input(1,length(input)-2:end);


%%The evaluation of preformance
%% 1.error
%error = abs(T_sim - output_test)./output_test;

%%
% 2. R^2
R2 = (5 * sum(T_sim .* output_test) - sum(T_sim) * sum(output_test))^2
/ ((5 * sum((T_sim).^2) - (sum(T_sim))^2) * (5 * sum((output_test).^2)
- (sum(output_test))^2));

%%
% 3. Comparsion
%result=[output_test' T_sim' error'];
%% Figure
```

```
figure
plot(1:5,output_test,'b:*',1:5,S(index,:),'r-o')
legend('Test value','Predicted value')
xlabel('Sample')
ylabel('Time(Hour)')
string = {'Comparsion';['error=' num2str(error)]};
title(string)



%%%%simulation
%%%%application%%%%%%%%%%%%%%%%%%%%%%%%%%%%%%%%%%%%%%%%%%%%%%%%%%%%%%%%%%%

simulation_test=xlsread('simulation 5 digites.xlsx');
%Normalised 2%%
%[simulation_test1, ps_input] = mapminmax(simulation_test,0,1);

%[outtrain, ps_output] = mapminmax(output_train,0,1);

%%Simulation
test_out1=sim(net,simulation_test);
%Renormalised%%
%simulation_result = mapminmax('reverse',test_out1,ps_output);
%result%%
abssimulation_result=abs(test_out1);
%simulation_test=xlsread('test1.xlsx');

%Normalised 2%%
%[simulation_test1, ps_input] = mapminmax(simulation_test,0,1);

%[outtrain, ps_output] = mapminmax(output_train,0,1);

%%Simulation

%test_out1=sim(net,simulation_test1);

%Renormalised%%

simulation_result = mapminmax('reverse',test_out1,ps_output);
```

A4. Artificial neural network with genetic algorithm and leave one cross validation.

```
%%%% code to establish machine learning model
```

```
clear all
close all
clc

%%%% Input data

input=xlsread('test rig input.xlsx');
output=xlsread('test rig output.xlsx');


k=rand(1,50);
[ m, n]=sort(k);
input_train= input(:,n( 1:49));
output_train = output(:,n(1: 49));
input_test= input(:,n(50:50));
output_test=output(:,n(50:50));
%%Normalised%%


%%Normalised%%
[intrain, ps_input] = mapminmax(input_train,0,1);
intest= mapminmax('apply',input_test,ps_input);

[outtrain, ps_output] = mapminmax(output_train,0,1);

%%Selecting the optimal hidensize%%
for i=1:20


hiddenSizes =i;
trainFcn = 'trainlm';
net=feedforwardnet(hiddenSizes,trainFcn);


[net,tr]=train(net,intrain,outtrain);
test_out=sim(net,intest);

%%Renormalised%%
T_sim = mapminmax('reverse',test_out,ps_output);



error = abs(T_sim - output_test)./output_test;
%error = abs(T_sim - output_test);
%error1=error
%error=error(1)+error(2)+error(3);
a1(i)=error;
a(i)=1/error;
S(i,:)=T_sim;

end
```

```
num=size(a,2);
max_grad=0;
index=1;
for i=1:size(a,2)
    max_grad=a(i);
    for j=1:size(a,2)
        if j~=i
            if a(j)>=max_grad
                max_grad=a(j);
                index=j;

            end

        end

    end

end

fprintf('The optimal hiddensize is %-5f',index);

error=a1(index);
%error=error/3;

T_sim = S(index,:)



%%Structure of network
inputnum=4;
hiddennum=index;
outputnum=1;

%%Genetic algorithm

hiddenSizes =index;
trainFcn = 'trainlm';
net=feedforwardnet(hiddenSizes,trainFcn);

%%Iteration number
maxgen=100;
%%Population size
sizepop=5;
%%Cross probability
pcross=[0.4];
%%Mutation probability
pmutation=[0.2];

%%Toatal joint number
numsum=inputnum*hiddennum+hiddennum+hiddennum*outputnum+outputnum;

lenchrom=ones(1,numsum);
```

```
bound=[-3*ones(numsum,1) 3*ones(numsum,1)];

%%Structure of population
individuals=struct('fitness',zeros(1,sizepop),'chrom',[]);
avgfitness=[];
bestfitness=[];
bestchrom=[];

%%Calculation of individual fitness
for i=1:sizepop

    individuals.chrom(i,:)=Code(lenchrom,bound);

    x=individuals.chrom(i,:);

individuals.fitness(i)=fun(x,inputnum,hiddennum,outputnum,net,intrain,
outtrain);
end
FitRecord=[];

[bestfitness bestindex]=min(individuals.fitness);
bestchrom=individuals.chrom(bestindex,:);
avgfitness=sum(individuals.fitness)/sizepop; %


trace01=[avgfitness bestfitness];


for i=1:maxgen

    %%Selection
    individuals=select(individuals,sizepop);

    %%Cross

individuals.chrom=Cross(pcross,lenchrom,individuals.chrom,sizepop,boun
d);

    %%Mutation

individuals.chrom=Mutation(pmutation,lenchrom,individuals.chrom,sizepo
p,i,maxgen,bound);

    %%Calculating fitness
    for j=1:sizepop
        x=individuals.chrom(j,:);

individuals.fitness(j)=fun(x,inputnum,hiddennum,outputnum,net,intrain,
outtrain);
    end
        %%Finding optimal individual
        [newbestfitness,newbestindex]=min(individuals.fitness);
```

```
        [worestfitness,worestindex]=max(individuals.fitness);

        %%Updating optimal individual
        if bestfitness>newbestfitness
            bestfitness=newbestfitness;
            bestchrom=individuals.chrom(newbestindex,:);

        individuals.chrom(worestindex,:)=bestchrom;
        individuals.fitness(worestindex)=bestfitness;
        end
        %%Calculating fitness of optimal individual
        avgfitness=sum(individuals.fitness)/sizepop;
       trace01=[trace01;avgfitness bestfitness];
    FitRecord=[FitRecord;individuals.fitness];
    end


   %%Results analysis
 figure(1)
[r c]=size(trace01);
plot([1:r],trace01(:,2),'b--');
title(['Error Fitness ' 'Final iteration' num2str(maxgen)]);
xlabel('Iteration number');ylabel('Fitness');
legend('Average fitness','Optimal fitness');
disp('Fitness                  varibale');

    %%Assigning optimal individual to network
   x=bestchrom
   w1=x(1:inputnum*hiddennum);
   B1=x(inputnum*hiddennum+1:inputnum*hiddennum+hiddennum);

w2=x(inputnum*hiddennum+hiddennum+1:inputnum*hiddennum+hiddennum+hidde
nnum*outputnum);

B2=x(inputnum*hiddennum+hiddennum+hiddennum*outputnum+1:inputnum*hidde
nnum+hiddennum+hiddennum*outputnum+outputnum);

   net=configure(net,intrain,outtrain)

   net.iw{1,1}=reshape(w1,hiddennum,inputnum);
   net1w{2,1}=reshape(w2,outputnum,hiddennum);
   net.b{1}=reshape(B1,hiddennum,1);
   net.b{2}=B2;



%%Training network
%%Parameters of network
net.trainParam.epochs=100;
net.trainParam.lr=0.1;
net.trainParam.goal=0.00001;
```

```
%%Training network
[net,tr]=train(net,intrain,outtrain);
test_out=sim(net,intest);

%%Renormalised%%
T_sim = mapminmax('reverse',test_out,ps_output);

%%figure
%figure
%plot(1:4000,input_train,'bo');hold on;
%plot(1:2000,input_test','go');
%plot(1:4000,output_train,'k+');
%plot(1:2000,T_sim,'r*');

answ=net.iw;
ansb=net.b;

%%Simulation
%test_out1=sim(net,Orthogonal expeimental test.xlsx);
%data_simulation=input(1,length(input)-2:end);


%%The evaluation of preformance
%% 1.error
%error = abs(T_sim - output_test)./output_test;

%%
% 2. R^2
R2 = (1 * sum(T_sim .* output_test) - sum(T_sim) * sum(output_test))^2
/ ((1 * sum((T_sim).^2) - (sum(T_sim))^2) * (1 * sum((output_test).^2)
- (sum(output_test))^2));

%%
% 3. Comparsion
%result=[output_test' T_sim' error'];
%% Figure
figure
plot(1:1,output_test,'b:*',1:1,S(index,:),'r-o')
legend('Test value','Predicted value')
xlabel('Sample')
ylabel('Time(Hour)')
string = {'Comparsion';['error=' num2str(error)]};
title(string)



%%%%simulation
%%%%application%%%%%%%%%%%%%%%%%%%%%%%%%%%%%%%%%%%%%%%%%%%%%%%%%%%%%%%

simulation_test=xlsread('simulation 5 digites.xlsx');
%Normalised 2%%
```

```
%[simulation_test1, ps_input] = mapminmax(simulation_test,0,1);

%[outtrain, ps_output] = mapminmax(output_train,0,1);

%%Simulation
test_out1=sim(net,simulation_test);
%Renormalised%%
%simulation_result = mapminmax('reverse',test_out1,ps_output);
%result%%
abssimulation_result=abs(test_out1);
%simulation_test=xlsread('test1.xlsx');

%Normalised 2%%
%[simulation_test1, ps_input] = mapminmax(simulation_test,0,1);

%[outtrain, ps_output] = mapminmax(output_train,0,1);

%%Simulation

%test_out1=sim(net,simulation_test1);

%Renormalised%%

simulation_result = mapminmax('reverse',test_out1,ps_output);
```